AFRL-AFOSR-JP-TR-2018-0040

Rarefied plasma aerodynamics for LEO objects in the ionosphere

Laurie Brown
University of New South Wales-NEW NCAGE Code

04/30/2018
Final Report

DISTRIBUTION A: Distribution approved for public release.

Air Force Research Laboratory
AF Office Of Scientific Research (AFOSR)/ IOA
Arlington, Virginia 22203
Air Force Materiel Command

FORM SF 298

REPORT DOCUMENTATION PAGE

Form Approved
OMB No. 0704-0188

1. REPORT DATE *(DD-MM-YYYY)*
14-05-2018

2. REPORT TYPE
Final

3. DATES COVERED *(From - To)*
28 Sep 2016 to 27 Jan 2018

4. TITLE AND SUBTITLE
Rarefied plasma aerodynamics for LEO objects in the ionosphere

5a. CONTRACT NUMBER

5b. GRANT NUMBER
FA2386-16-1-4134

5c. PROGRAM ELEMENT NUMBER
61102F

6. AUTHOR(S)
Laurie Brown

5d. PROJECT NUMBER

5e. TASK NUMBER

5f. WORK UNIT NUMBER

7. PERFORMING ORGANIZATION NAME(S) AND ADDRESS(ES)
University of New South Wales-NEW NCAGE Code
HIGH STREET
KENSINGTON, NSW, 2052 AU

8. PERFORMING ORGANIZATION REPORT NUMBER

9. SPONSORING/MONITORING AGENCY NAME(S) AND ADDRESS(ES)
AOARD
UNIT 45002
APO AP 96338-5002

10. SPONSOR/MONITOR'S ACRONYM(S)
AFRL/AFOSR IOA

11. SPONSOR/MONITOR'S REPORT NUMBER(S)
AFRL-AFOSR-JP-TR-2018-0040

12. DISTRIBUTION/AVAILABILITY STATEMENT
A DISTRIBUTION UNLIMITED: PB Public Release

13. SUPPLEMENTARY NOTES

14. ABSTRACT
A Particle-in-Cell/Direct Simulation Monte Carlo (PIC/DSMC) solver was developed to investigate the conditions under which the interaction between a resident space object with the tenuous plasma in the ionosphere could produce sufficient force to perturb its orbit. A dimensional analysis of the unmagnetised Vlasov-Maxwell system of equations derived a set of 6 dimensionless parameters that describe the interaction of a body of arbitrary size and surface charge interacting with a plasma under the assumption of a mesothermal condition. The ion energy ratio () and general shielding ratio () were identified as the parameters that have the greatest influence on the ionospheric drag. The effect of charged drag on the orbit of a CubeSat sized object was investigated through developing a response surface model in and for a cylindrical body of varying radius and surface charge. The response surface was applied to 2 years worth of high fidelity atmosphere data from the Global Ionosphere/Thermospere Model (GITM), covering a year of high solar activity (2002) and low solar activity (2007). The results found that ionospheric aerodynamics could contribute between 5%-35% of the total aerodynamic force experienced by a CubeSat sized body at -3V above 469km in 2002 and above 400km in 2007 using the supplied GITM atmospheric dataset. The report concludes that previously neglected ionospheric aerodynamic could be a significant factor driving uncertainty in the accelerations experienced by satellites in the Low Earth Orbit Environment.

15. SUBJECT TERMS
rarefied plasma, aerodynamics, LEO, low earth orbit, ionosphere

16. SECURITY CLASSIFICATION OF:			17. LIMITATION OF ABSTRACT	18. NUMBER OF PAGES	19a. NAME OF RESPONSIBLE PERSON
a. REPORT	b. ABSTRACT	c. THIS PAGE			WINDER, SHEENA
Unclassified	Unclassified	Unclassified	SAR	90	19b. TELEPHONE NUMBER *(Include area code)* +81-42-511-2008

space
UNSW CANBERRA

Rarefied Plasma Aerodynamics for LEO Objects in the Ionosphere

Air Force Office of Scientific Research FA2386-16-1-4134: Final Report

Dr. Christopher Capon, Dr. Melrose Brown,

Lewis Freeland, Brenton Smith, Dr. Philippe Lorrain, Prof. Russell Boyce

Executive Summary

Rapid and accurate prediction of Resident Space Objects (RSO) orbital elements is a capability vital for the sustainable development of the near-Earth environment as it becomes increasingly congested and contested. An understanding of all the forces influencing the dynamics of RSOs is fundamental to this capability. The influence of the charged aerodynamic interaction of RSOs with the ionosphere (i.e. ionospheric aerodynamics) on their motion is currently not considered in Precise orbit Prediction and Determination (PoPD) applications despite neutral aerodynamics being the largest non-conservative force on LEO objects with the largest associated uncertainties. This report details the development of framework for quantifying the influence of ionospheric aerodynamics on the motion of RSOs and provides preliminary evidence that ionospheric aerodynamics may appreciably contribute to the uncertainties in aerodynamics models.

To determine the significance of ionospheric aerodynamics in LEO, the hybrid Particle-in-Cell (PIC)/Direct Simulation Monte Carlo (DSMC) code, pdFOAM, was developed and validated in collaboration with the University of Strathclyde in the OpenFOAM framework. A dimensional analysis of the unmagnetised Vlasov-Maxwell system of equations that describe a K-species plasmas resulted in the identification of $2+4K$ non-dimensional scaling parameter. A comprehensive investigation of the influence of these scaling parameters on underlying physical phenomena highlighted the importance of the ion energy ratio α and general shielding ratio χ to charged drag forces. These scaling parameters were combined in conjunction with a control surface analysis, where charged aerodynamics forces were separated into direct forces resulting from gas-surface interactions and indirect forces resulting from the scattering of non-colliding ions (and captured here through the deformations caused in the plasma sheath structure and transmitted through the Maxwell stress tensor), to provide new insights into the role of plasma-body interaction phenomena on the charged drag.

Drawing upon these insights, a response surface based on observed physical trends and fitted to simulation outputs in a parameter space defined by α and χ was constructed to allow the rapid prediction of the charged drag coefficient $C_{D,C}$ based on atmospheric model outputs. This response surface was applied to 2 years' worth of high fidelity atmospheric data generated by the Global Ionosphere/Thermosphere Model (GITM) from the University of Michigan, covering a period of high and low solar activity. The results reveal that charged ionospheric drag can account for between 5% - 35% additional force for a CubeSat sized body with a fixed body potential of -3V relative to the surrounding plasma for altitudes typical of many Low Earth Orbit missions. A greater ratio of charged to neutral work done per orbit was found in the lower solar activity period of 2007 than 2002, suggesting that ionospheric aerodynamics can have an appreciable contribution to the total aerodynamic force vector relative to the neutral drag component throughout the 11-year solar cycle.

UNIVERSITY OF NEW SOUTH WALES CANBERRA, ACT

This research was undertaken with the assistance of resources from the National Computational Infrastructure, which is supported by the Australian Government.This work was supported by the Air Force Office of Scientific Research under award number FA2386-16-1-4134. Elements of this work have been published in [1], [2],[3], [4].

April 30, 2018

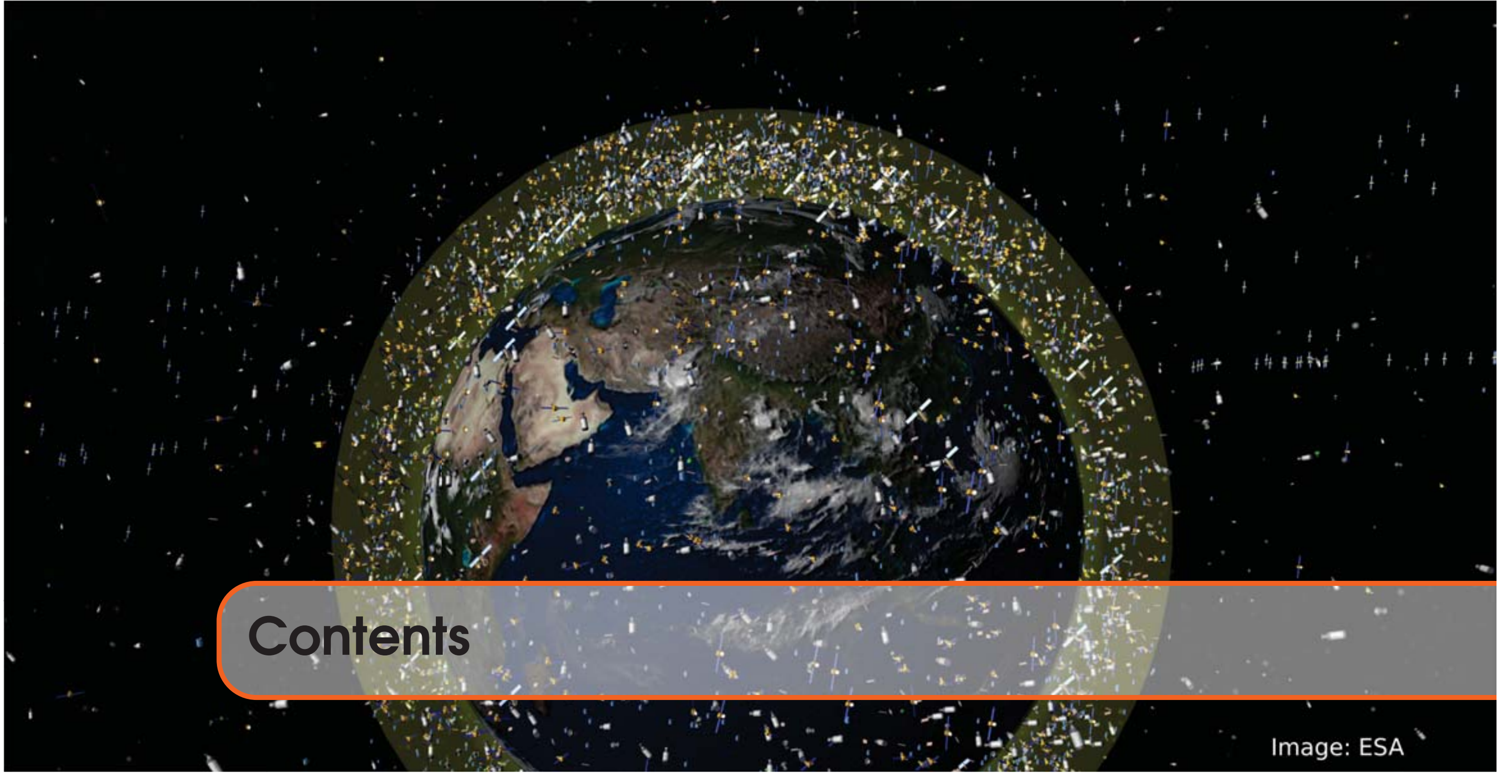

Contents

1. Introduction

Addressing current risks and future opportunities associated with the utilisation of space-based technologies requires advances in our ability to understand, and accurately and rapidly predict how Resident Space Objects (RSO) interact with their local space environment - both operational satellites and space debris. In the report *"Continuing Kepler's Quest"*, the US National Research Council recommended that US Air Force Space Command tackle a series of current and pending problems that face the international community in relation to space debris and collision avoidance [5]. As the largest non-conservative force on Low Earth Orbit (LEO) objects below 2000 km altitude, the aerodynamic interaction of RSOs with the near-Earth space environment represents an important facet of these problems. The importance of spacecraft aerodynamics has been demonstrated in a variety missions. For example, aerodynamic forces at altitudes of several hundred km were sufficient to demonstrate the formation reversal of three CubeSats in the AeroCube-4 mission, while the in-track discrepancy between onboard GPS and standard orbit propagation algorithms was observed to grow by 10-20 km per day for that mission with a spanwise discrepancy of 1-3 km per day [6]. Thus the forces generated by the interaction of space objects and the rarefied atmosphere in which they fly are non-negligible, integrate to produce significant orbital perturbations. Unfortunately, aerodynamic forces on near-Earth RSO's also have the largest associated uncertainties.

Typical orbit predictions assume cannon-ball representations of space objects using a drag coefficient C_D of 2.2 and ignore spanwise forces. As demonstrated numerically [7] and examined with Direct Simulation Monte Carlo (DSMC) simulations in the Los Alamos National Laboratory IMPACT project [8], the drag coefficient of objects can in fact vary by up to 40% for a given shape over altitude ranges typical of LEO and depends significantly on factors such as solar maximum/minimum. Various models of the thermosphere and ionosphere are available to compute atmospheric parameters for orbit predictions, at varying levels of fidelity ranging from semi-empirical correlations through to physics-based three-dimensional computational fluid dynamics simulations that require significant computational effort. Modelling the space environment - a large, complex, time-varying structure sensitive to space weather perturbations - is difficult, however, early models based on sparse measurements and subsequently built up over time. As a consequence of the historical development of many atmospheric models, predictions of atmospheric neutral density may vary significantly from each other. This is emphasised in Figure 1.1, which compares the neutral density inferred from the CHAMP spacecraft [9]. Figure 1.1 demonstrates not only disagreements between atmospheric models, but apparent anomalous behaviour such as the 85% spike in inferred neutral density in the middle of the figure - see also [10, 11]. In a critical analysis of atmospheric models Vallado and Finkleman [12] concluded that there appeared to be a common unmodelled physical mechanism or systemic error in the MSIS-86 and Jacchia 71 neutral atmosphere models. One currently unmodelled physical mechanism that may account for this anomalous behaviour is the direct interaction of RSOs with the ionosphere i.e. *"ionospheric aerodynamics"*.

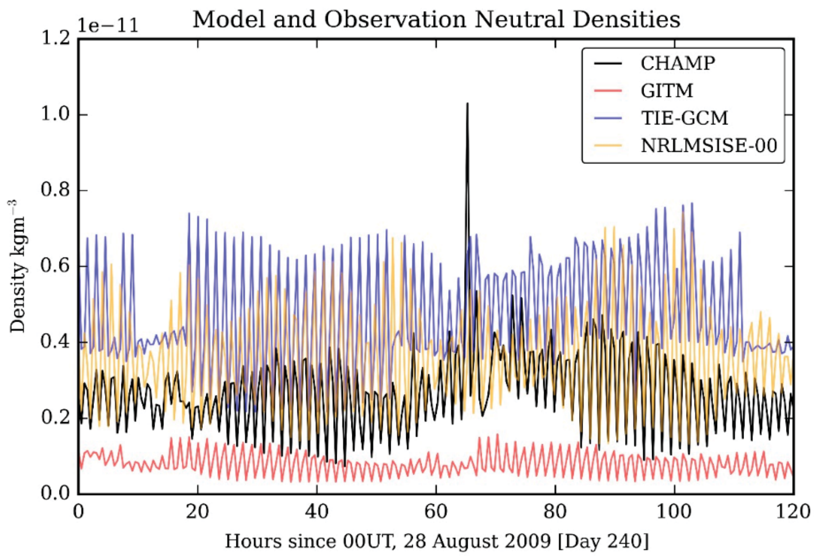

Figure 1.1: Predicted and inferred neutral density variations for CHAMP.

The aerodynamic interaction between RSOs and the ionosphere (charged environment) is fundamentally different from the aerodynamic interaction between the object and the thermosphere (neutral environment). Whenever an object is immersed in a plasma, it acquires a floating potential (ϕ_B) with respect to the freestream plasma based on the sum of currents into/out of the surface. In LEO, the electron thermal velocity is orders of magnitude larger than an object's orbital velocity, which is, in turn, larger than the surrounding ion thermal velocity. This velocity distribution (known as a *"mesothermal flow"*) results in a negative floating potential and sets up a region of charge discontinuity about the body where ions are accelerated toward the body and electrons are repelled such that the ion and electron currents are equal. This region of charged discontinuity is known as the *"plasma sheath"*.

The plasma sheath has two key effects: the first is to increase the effective collection area of the object beyond the wetted area of the body; the second is to deflect (scatter) ions into (or away from) the wake of the object. The increase in effective collection area allows direct charged aerodynamic forces resulting from gas-surface interactions to be enhanced compared to an equivalent rarefied gas dynamic interaction. The deflection of ions causes an indirect exchange of momentum between the object and ions also known as *"dynamic friction"* [13, 14]. Hence, while neutral aerodynamics in LEO is well described by rarefied gas mechanics [15] [1], ionospheric aerodynamics calculations must account for both the direct and indirect exchange of momentum between the object and the surrounding plasma through field effects.

In short, ionospheric aerodynamic mechanisms tend to increase aerodynamic forces beyond those in an equivalent neutral interaction. The reasons ionospheric aerodynamic forces are not currently modelled stems back to conclusions by Brundin [14] referenced in the seminal work by Cook [16]. These conclusions were based around the following key assumptions:

- That the surface potential of LEO objects is never more negative than -0.75 V with respect to a quasi-neutral freestream plasma ($\phi_\infty = 0$).
- That the maximum ion number density is approximately 10% of the neutral number density in LEO.
- That monotonic oxygen ions (O^+) are the dominant source of charged aerodynamic forces (monotonic hydrogen ions (H^+) were not considered).

Based on these assumptions, Brundin [14] concluded that neglecting ionospheric aerodynamic forces would cause a maximum possible over-prediction of neutral density by 20% when based on satellite accelerations. With advances in knowledge of the LEO space environment and the increasing complexity of LEO satellites and their orbits, the validity of each of these assumptions has become questionable. It is now recognised that LEO objects can naturally achieve floating potentials more negative than -100 V (albeit for short periods), while the use of high voltage power systems can cause large artificial surface potentials [17–22]. Advances in atmospheric models mean that regions where the ion number density approaches the neutral number density are well recognised.

For example, in a numerical analysis the charged drag force on a high voltage solar array ($O(-1kV)$) with an approximate altitude of 500 km, Kuriki and Kuninaka [23] predicted ion drag to range between $5-10$ times that of the local neutral drag when at 90 degrees angle of attack (maximum surface area) [2]. Similarly, a recent study by Andrés de la Fuente [24] offers *in-situ* evidence that charged aerodynamic forces can be significant. Andrés de la Fuente [24] applied the dusty plasma theory described outlined by Hutchinson [25–27] to predict the contribution of charged aerodynamics to the anomalous along-track accelerations experienced by the LAGEOS-I and LAGEOS-II satellites with nominal altitudes of 5900 km (Medium Earth Orbit). Andrés de la Fuente [24] concluded that the contribution of charged aerodynamics to along-track accelerations increases from -0.5 pms^{-2} when not in eclipse to -85 pms^{-2} and -70 pms^{-2} respectively in eclipse - the larger eclipse charged aerodynamic acceleration for the LAGEOS-I a reflection of its orbit which brought it over the auroral and polar zones where larger negative floating potentials occur. Compared to a neutral drag acceleration of -0.5 pms^{-2}, Andrés de la Fuente [24] demonstrated that charged aerodynamics can have a significant and complex effect on the dynamics of the LAGEOS spacecraft in MEO. It is, therefore, reasonable to revisit the question pursued by Brundin [14], can ionospheric aerodynamics have an appreciable effect on the motion of LEO objects?

Following world best practice for aerospace research, UNSW Canberra Space is developing an astrodynamics research program that closely couples physics-based supercomputer simulations of the interaction between spacecraft/debris and the near-Earth environment, benchmark-quality

[1] Uncertainties in neutral aerodynamics are primarily caused by the nature of the gas-surface interaction [7]

[2] Kuriki and Kuninaka [23] only accounted for the direct force from gas-surface interactions. As will be shown later, the indirect contribution of scattered ions plays an important role in the calculation of charged drag forces.

ground-based experiments (by means of employing high energy / low density particle sources to create a rarefied gas satellite "wind tunnel"), and orbital flight experiments to validate the ground-based science. This report represents *Phase A* of this program and outlines the development of a high-fidelity space simulation capability to understand the aerodynamics interaction of RSOs with the ionosphere to determine whether ionospheric aerodynamic forces can have an appreciable influence on the motion of LEO objects. The simulation capability and understanding of the fundamental physics involved in these interactions will then be used to guide and develop ground-based experiments and on-orbit experiments. In turn, this research program is intended to eventually contribute to the development of advanced orbit propagation and collision-avoidance algorithms for Australian input to space traffic and debris management. This activity would directly support the efforts of the University of Arizona led AFOSR/AFRL Astrodynamics CoE, specifically in the area of dynamical interaction and modelling of vehicles with the space environment, accounting for coupling between translational and rotational motion, and the full effect of the natural environment on RSOs.

The following sections provide relevant background material on the structure of the near-Earth environment and near-Earth plasma-body interactions. The final section outlines the objectives of this report.

1.1 Structure of the Near-Earth Environment

Compared to Geostationary Earth Orbit (GEO), the LEO space environment is a cold, dense, quasi-neutral, partially ionised plasma primarily composed of N_2, O_2, O, He and H and their ionised analogues. Description of the environment is often broken into the neutral domain, comprising the thermosphere (90 – 600 km) and exosphere (> 600 km)[3], and the charged domain, also known as the ionosphere. The structure of the thermosphere and ionosphere are significantly different. Figure 1.2 plots representative variations in neutral and ion composition with altitude during a representative international quiet solar year.

The temperature of the thermosphere asymptotes to a common exospheric temperature with increasing altitude. A consequence of this common temperature is the stratification of constituents by molecular mass, the driving force being gravity [31]. Extreme ultraviolet (EUV) solar radiation provides the primary direct day-side heat source, producing large thermal gradients with the night-side and causing upper atmospheric winds ranging from 1 km/s to 100 km/s [31, 32]. Solar EUV production exhibits an 11-year cycle that results in density variations of an order of magnitude, while dinural[4] variations are typically on the order of 10% [31]. EUV also is a primary ionisation mechanism maintaining the day-side ionisation of the charged environment [30].

While the thermosphere is gravity and temperature dependent, the Earth's magnetic field and self-induced local electromagnetic inhomogeneities govern the ionosphere. As a result, the ionosphere exhibits a greater latitudinal variation than the thermosphere [30]. Similarly, the distribution of ionospheric constituents with altitude is non-linear and coupled with global and local electromagnetic perturbations. The injection/precipitation of energetic plasma species into polar auroral regions during solar weather events, such as coronal mass ejections, along with increased EUV fluxes can significantly disturb the ionosphere [17, 21, 22, 30].

During these events, energy input can increase by an order of magnitude compared to local EUV

[3] Hereafter referred to as the thermosphere for convenience.

[4] 24 hour

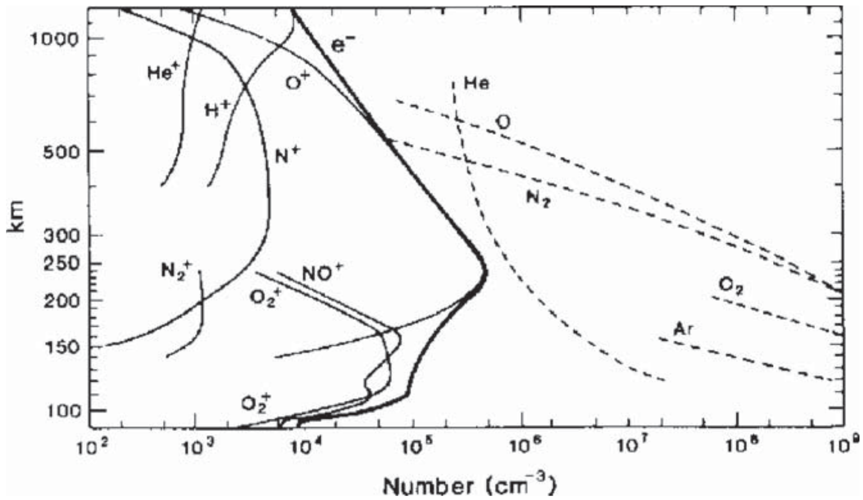

Figure 1.2: Representative daytime atmosphere structure during an international quiet solar year. Reproduced from [28].

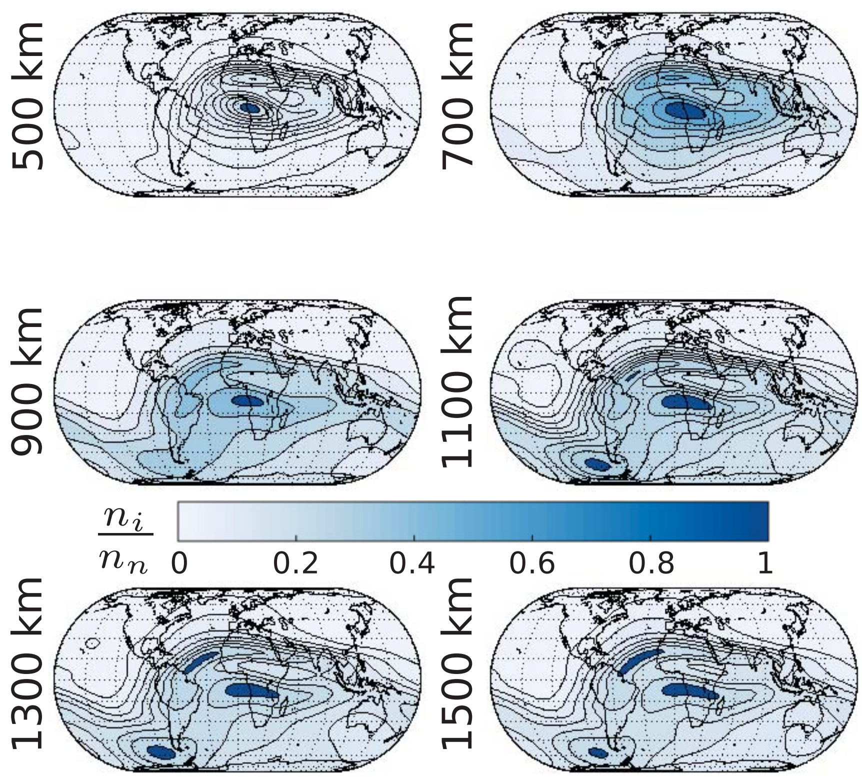

Figure 1.3: Comparison of total ion and neutral number densities in LEO based on the NRLMSISE-00 [29] and IRI-2012 [30] atmospheric models. Conditions are for 4/1/2007 UT 12:00:00 with solar indices $f_{10.7} = 87.7$, $f_{10.7a} = 83.35$ and using the daily magnetic index $a_p = [17.3750, 15.0, 20.0, 15.0, 27.0, 18.125, 21.75]$.

input, increasing ionisation, temperature, and other key parameters [17, 22]. The redistribution of this energy to the thermosphere occurs through transfer mechanisms, significantly disturbing global circulation patterns and generating phenomena such as travelling ionospheric disturbances and gravity waves [31]. It is perhaps not surprising then that the modelling of the LEO environment has been, and remains, difficult [31].

Two established atmospheric models are the Naval Research Laboratory Mass Spectrometer Incoherent Scatter Radar Extended (NRLMSISE-00) [29] and International Reference Ionosphere (IRI-2012) [30] atmospheric models. For a comprehensive review of atmospheric models see Emmert [31] and Vallado and Finkleman [12]. A principle argument for neglecting ionospheric aerodynamic forces in [14] was that ion number densities (n_i) are orders of magnitude less than neutral number densities (n_n). While true below $300-400$ km altitude (depending on space weather conditions), as altitude increases so does the proportional ionisation of the environment. This is demonstrated in Figure 1.3, which plots n_i/n_n slices through altitude based on NRLMSISE-00 and IRI-2012 atmospheric models. Conditions are for the 4^{th} of January 2007 UT 12:00:00 with solar indices $f_{10.7} = 87.7$, $f_{10.7a} = 83.35$ and using the daily magnetic index $a_p = [17.3750, 15.0, 20.0, 15.0, 27.0, 18.125, 21.75]$[5].

The IRI-2012 and NRLMSISE-00 atmospheric models, however, are largely empircal. As a consiquence, they have inherited drag baises from early datasets based on constant drag coefficients of 2.2. The Global Ionosphere-Thermosphere Model (GITM) is a physics based atmospheric model, which incorperates the coupling of the ionosphere and thermosphere in an attempt to bypass some of these historical biases while providing new insights into fundamental physics.

Unlike other models in this class, particularly the widely used NCAR-TIEGCM [33], GITM does not assume the upper atmosphere is in hydrostatic equilibrium. This has the effect of allowing GITM to better capture the full magnitude of vertical thermospheric winds, which are an important energy transfer mechanism. This approach also allows GITM to use altitude as the vertical axis variable, rather than the more traditional pressure, this in turn allows GITM to include gravitational acceleration as a function of altitude.

To investigate the influence of the aerodynamics forces from both the ionosphere and thermosphere on RSOs, this work will employ the coupled ionosphere/thermosphere model, GITM. This work will use data provided by the Los Alamos National Laboratory for simulations of 2002 and 2007 for the whole globe at 90-minute cadence and $72 \times 36 \times 50$ resolution.

[5]Relevant solar and magnetic data can be obtained from `ftp://ftp.ngdc.noaa.gov/STP/space-weather/solar-data/solar-features/solar-radio/noontime-flux/penticton/` and `ftp://ftp.ngdc.noaa.gov/STP/GEOMAGNETIC_DATA/INDICES/KP_AP/`

1.2 Near-Earth Plasma-Body Interactions

The physics of a conducting body immersed in a stationary, collisionless, quasi-neutral plasma is well established [26, 34–36]. The most probable ion ($v_{t,i}$) and electron ($v_{t,e}$) thermal velocity in three dimensions is given by Bird [37],

$$v_{t,i(e)} = \sqrt{\frac{2k_B T_{i(e)}}{m_{i(e)}}} \tag{1.1}$$

where k_B is the Boltzmann constant, subscripts i and e refer to ion and electron properties, and T and m are the ion and electron temperature and mass respectively.

From Eqn. 1.1 it is clear that, except for the conditions where $T_i \gg T_e$, the relative mass of ions and electrons results in $v_{t,i} \ll v_{t,e}$. Consequently, when an object is immersed in the plasma, the surface initially experiences a larger flux of electrons than ions and the body gains a macroscopic negative charge relative to the surrounding plasma. Plasmas tend to work to neutralise charge discontinuities, hence the body surface potential (ϕ_B) caused by the build-up of charge on the body's surface tends to accelerate and repel nearby ions and electrons. The body is said to have achieved a *"floating potential"* when the ion and electron currents (I) have achieved some dynamic equilibrium i.e. $I_i = I_e$. Ions are not accelerated from infinity however, instead there exists a region of charge discontinuity surrounding the body known as the *"plasma sheath"*, beyond which the plasma is electrically shielded from the influence of the body. While the structure of plasma sheaths in quiescent plasmas are well understood, when there exists relative motion between the plasma and body, such as in LEO, the sheath structure becomes significantly more complex [38, 39].

The structure of LEO plasma-body interactions has been studied extensively[6]. In general, these studies fall into one of two categories: studies that investigate the floating potential of LEO objects by calculating the self-consistent ion and electron surface currents [19, 35, 39–46]; and the study of wake phenomena from a charging context or physics perspective [38, 47–54]. Charging studies are intrinsically related to charged aerodynamics, the difference being the prediction of ion/electron surface fluxes (charging) compared to momentum exchange (charged aerodynamics). Charging studies are not interested momentum exchange, but instead the distribution of ion current collection and the equilibrium condition where ion current equals electron current ($I_i = I_e$). Similarly, studies focusing on the characterisation of plasma interaction phenomena, while providing important physical insights to plasma-body interaction phenomena, do not consider the influence of these phenomena to momentum exchange - the justification for the characterisation of phenomena generally related to charging. Nevertheless, it is instructive to review the general structure of LEO plasma-body interactions based on this literature.

Figure 1.4 illustrates the general anatomy of LEO plasma-body interactions, linking observed collective phenomena with representative ion trajectories [38, 39, 50, 54]. The LEO plasma interaction phenomena illustrated in Figure 1.4 arise primarily from the relative velocity between LEO objects and the ionosphere. The orbital velocity (v_B) of LEO objects is on the order of 7.5 km/s. As a result, LEO objects move hyperthermally ($v_B \gg v_{t,i}$) relative to the ion thermal velocity ($v_{t,O^+} \approx 1.25$ km/s) and subthermally ($v_B \ll v_{t,i}$) relative to the electron thermal velocity ($v_{t,e} \approx 246$ km/s). This bi-thermal velocity distribution is referred to as a *"mesothermal"* flow. As illustrated in Figure 1.4, characteristic features resulting from this velocity distribution are a compressed fore-body (or *"ram"*) sheath and an elongated *"wake"* sheath surrounded by a *"rarefaction wave"* [38].

[6] The study of floating potentials and surface potentials in LEO.

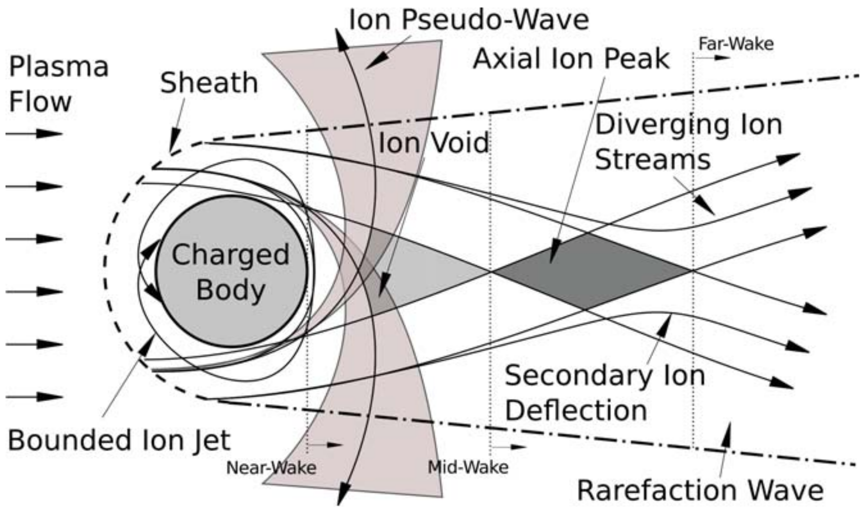

Figure 1.4: Illustration of relationship between collective phenomena observed in mesothermal plasma-body interactions and ion trajectories.

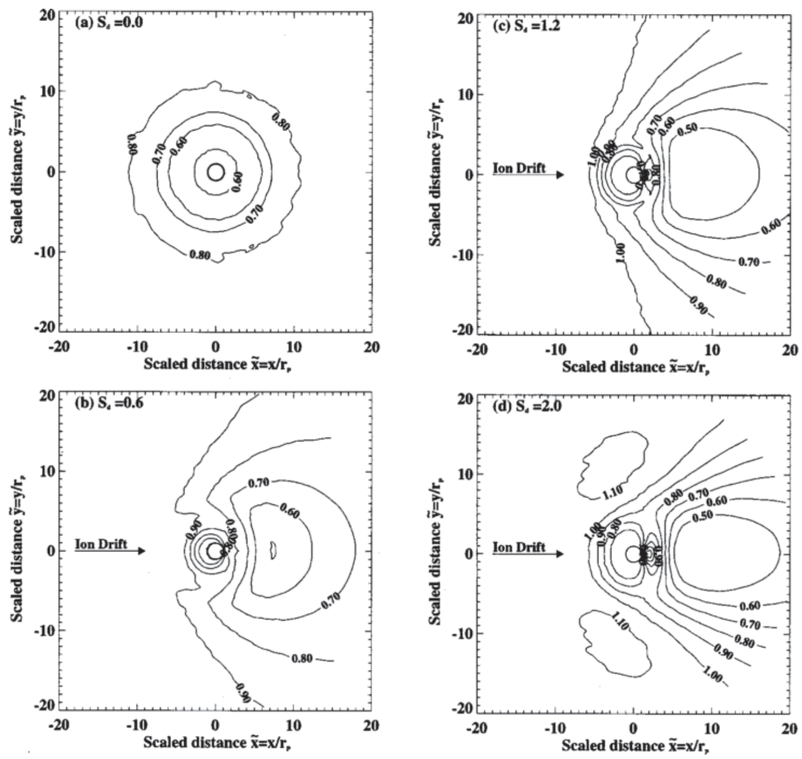

Figure 1.5: Contours of equal ion density $\hat{n}_i$ around a probe for various drift speed ratios S_d. Plasma parameters are $\Phi_B = -25$, $\lambda_{D,e}/r_B = 1$, $T_e/T_i = 1$. Reprinted from McMahon, Xu, and Laframboise [39] with the permission of AIP Publishing.

Two important additional features are shown in Figure 1.4, bounded ion jets and ion pseudo-waves.

The compression of the ram sheath and elongation of the wake sheath seen in Figure 1.4 is a product of the hyperthermal ion velocity where ions are unable to populate the near-wake region immediately behind the body. The electron mobility allows an initial population of the ion void region labelled in Figure 1.4 causing a localised negative disturbance trailing behind the body. The negative region then attracts ions into the wake region and deflects incoming electrons, re-populating the wake region significantly faster than equivalent neutral flow interactions where re-population is a function of gas temperature.

The re-population of the wake region by deflected ions causes an ion density gradient as ions move to fill the wake. This density gradient causes a collective response in the plasma in the form of a *"rarefaction wave"*, defined by the leading edge of the density gradient travelling perpendicularly outwards to the flow direction. As illustrated in Figure 1.4, in the frame of the body this rarefaction wave angle (θ_r) appears physically similar to a continuum Mach wave where its angle relative to the flow direction is defined by the ion acoustic Mach number (M_i)[7], e.g. [55]

$$\theta_r = \sin^{-1}\left[\frac{1}{M_i}\right], \qquad M_i = \frac{v_B}{\sqrt{k_B(T_e+\gamma_i T_i)/m_i}} \tag{1.2}$$

where the ion adiabatic index γ_i refers to the ability of real gases to store energy in higher energy rotational and vibrational states (degrees of freedom n),

$$\gamma_i = 1 + 2/n \tag{1.3}$$

In a collisionless plasma $n = 1$ and $\gamma_i = 3$ [55].

Within the wake, the confluence point of deflected ions may then create a positive space-charge region of sufficient intensity to cause the secondary deflection of incoming ions[8] [38]. Finally, depending on where they enter the sheath, ions within particular energy bands are deflected through the near wake on unbounded (hyperbolic orbit) or bounded (impact the body) trajectories. Together, these ions form bounded and unbounded ion jets, the latter appearing as the ion pseudo-waves illustrated in Figure 1.4.

McMahon, Xu, and Laframboise [39] investigated the effect of ion drift speed on plasma-body interaction phenomena, in particular the sheath and pre-sheath structure, to determine its effect on ion current collection i.e. a charging study. The method used by McMahon, Xu, and Laframboise [39] to simulate plasma-body interactions involved the tracing of particle trajectories through a computational domain to build-up a space-charge distribution. This space-charge distribution was then used to solve Poisson's equations for the electrostatic field $\phi(\mathbf{x})$, whereupon particle trajectories were traced through this potential field according to Newton's laws and the Lorentz force. This process was iteratively repeated until the average of the square of differences in normalised densities between two repetitions was smaller than a specified tolerance i.e. the solution had converged.. Figure 1.5 provides an illustrative example of the general plasma interaction phenomena described above [39]. Here contours are of normalised number density ($\hat{n}_= n_i(\mathbf{x})/n_\infty$) at various ion drift velocities normalised against thermal velocity ($S_d = v_B/\sqrt{2k_BT_i/m_i}$), where $\Phi = q_e\phi_B/k_BT_e = -25$ and $\lambda_{D,e}/r_B = 1$[9].

[7] The speed at which electrostatic information travels through a plasma.

[8] This primarily occurs in the wake of compact objects e.g. spheres, cubes.

[9] Here $\lambda_{D,e}$ is the electron Debye length and is generally used to describe the distance required to electrostatically shield an ion

The top left frame shows the stationary case, the plasma sheath causing a (near) uniform density gradient around the body i.e a symmetric plasma sheath. The bottom left frame shows the sub-thermal ($S_d < 1$) case, where ion drift velocity causes the formation of a rarefaction wave while the low kinetic energy of the freestream ions compared to the body results in bounded orbits that cause the apparent forebody density discontinuity. The top and bottom right panels show hyperthermal flows ($S_d > 1$), the peak in ion density in the immediate wake of the bodies caused by the confluence of deflected ions. Overdense regions outside the rarefaction wave in the bottom right panel are representative of unbounded ion jets, the super-position of unbounded ion jets and freestream ions causing an over-dense region.

It is also worth noting that the above phenomena assume unmagnetised plasma interactions. This is a common assumption whereby the gyration radius of ions[10] is orders of magnitude larger than object sizes in LEO (with the exception of the International Space Station) and therefore, in the frame of the body, the ions travel in straight lines. The unmagnetised assumption is also employed in this work.

1.3 Objectives of this Report

This work represent the first stage of development of the end-to-end space capability development roadmap at UNSW Canberra, where high fidelity numerical and experimental investigations couple together for the rapid design of innovative and meaningful in-orbit experiments. This work specifically works toward reducing uncertainties in orbit prediction by developing an understand of the fundamental physical phenomena that influence the motion of LEO objects.

To meet requirements of the AFOSR grant FA2386-16-1-4134, the objectives are this report are as follows:

- Outline the development and validation of the hybrid PIC-DSMC code, pdFOAM, and demonstrate its suitability as a space simulation tool.
- Determine the minimum set of parameters required to understand the fundamental interaction of a body immersed in a flowing plasma
- Develop a framework within which to quantify ionospheric aerodynamics forces.
- Apply this framework to determine whether ionospheric aerodynamic forces are appreciable compared to neutral aerodynamic forces and highlight regions of interest for future study.

Chapters of this report address each of these objectives respectively. Outputs from this report feed directly in AFOSR grant FA2386-17-1-4105, for development of an experimental capability to test conclusions of this report. Elements of this work have been published in [1–4], with several papers currently under review.

[10] The radius about which an ion gyrates when moving parallel to a magnetic field

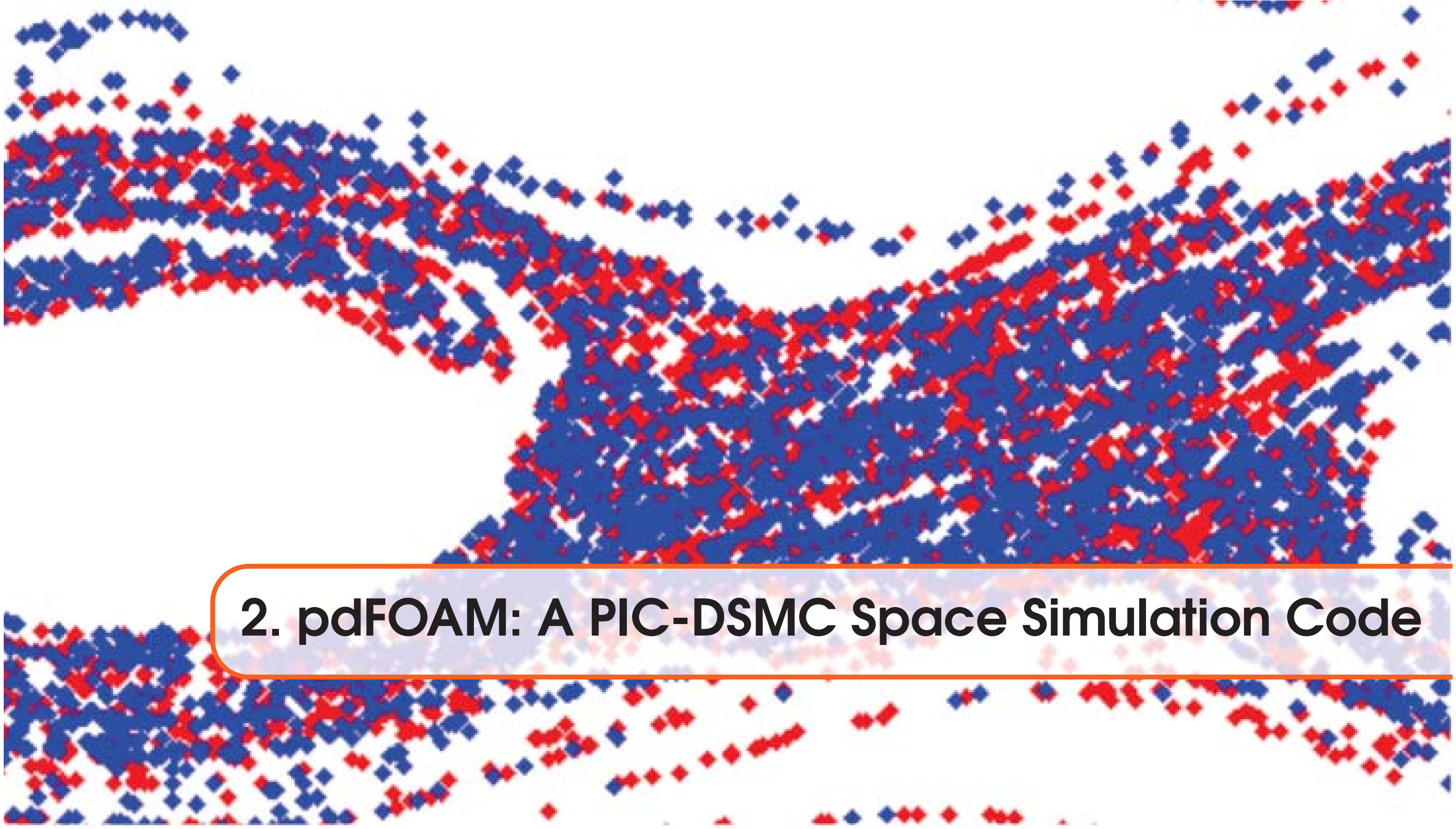

2. pdFOAM: A PIC-DSMC Space Simulation Code

The PIC-DSMC code, pdFOAM, has been developed here to investigate the interaction of RSOs with the space environment (including both charged and neutral environments) and is the principle research tool used throughout this work. pdFOAM has been developed in the open-source C++ CFD library, *OpenFOAM* [56], extending the DSMC code, *dsmcFOAM*[1], to include a PIC method.

This chapter details the implementation and validation of pdFOAM and is broken down as follows. Section 2.1 provides a brief introduction to kinetic theory and its relationship to the PIC and DSMC methods. Section 2.2 then describes the numerical realisation of the PIC method in pdFOAM. Section 2.3 presents two validation cases; the replication of results in Lofthouse [58] for the rarefied flow of Argon at Mach 10 over a cylinder, and the self-consistent charging of a flat plate and cylinder in a flowing plasma compared with the PIC code, PICLas [59]. The first case demonstrates the ability of pdFOAM to accurately predict surface force distributions, while the second case demonstrates the ability of pdFOAM to capture the self-consistent interaction of an object immersed in a flowing plasma. Together these cases demonstrate the suitability of pdFOAM to investigate charged aerodynamics.

2.1 Kinetic Theory and Super-Particle Methods

This section presents an overview of the relationship between kinetic theory and the PIC and DSMC methods. While this work is primarily focused on the collisionless plasma regions described by the PIC method, a discussion of the DSMC method is included for two reasons. The first is that the gas-surface interactions model used throughout this work was primarily developed within DSMC methods and all collisions are handled using the DSMC portion of pdFOAM. The second is that an avenue for future study is considering regimes or situations where particle-particle collisions are non-negligible e.g. below 300 km, out-gassing structures or objects employing mass based thrusters (either gas or ion).

[1] See Scanlon et al. [57] for a description of the implementation and validation of dsmcFOAM

2.1.1 The Vlasov-Maxwell Equations

The near-Earth space environment is a collection of positive ions, negative electrons, and neutral atoms and molecules. To describe this system, let us define the phase space distribution function f of particles of species k within the volume element $dx_1dx_2dx_3$ as $f_k(\mathbf{x}, \mathbf{c}_\alpha, t)$, where $\mathbf{c}_k$ and $\mathbf{x}$ are the particle velocity and position respectively at time t. Given a particular f_k, macroscopic mean properties arise from the moments of f_k e.g. number density (n_k) and velocity (v_k) [60],

$$n_k = \int f_k d\mathbf{c}, \;\; \mathbf{v}_k = \frac{1}{n_k}\int \mathbf{c}_k f_k d\mathbf{c} \tag{2.1}$$

At its most general, the evolution of f_k through t is described by the Boltzmann equation [61],

$$\frac{\partial f_k}{\partial t} + \mathbf{c}_k \cdot \nabla_x f_k + \frac{\mathbf{F}_k}{m_k} \cdot \nabla_c f_k = \left(\frac{\partial f_k}{\partial t}\right)_{coll} \tag{2.2}$$

From left to right, the terms on the LHS of Eqn. 2.2 describe: the rate of change of f_k with time; the diffusion of f_k; and the influence of external forces $\mathbf{F}_k$ acting on f_k. The RHS of Eqn. 2.2 describes the rate of change of f_α as a result of particle collisions.

In a plasma, Eqn. 2.2 describes the interaction of particles of mass m_k and charge q_k through their mutual electric ($\mathbf{E}$) and magnetic ($\mathbf{B}$) fields via the Lorentz force ($\mathbf{F_k}$) [61, 62],

$$\mathbf{F}_k = q_k\left(\mathbf{E}(\mathbf{x},t) + \mathbf{c}_k \times \mathbf{B}_k(\mathbf{x},t)\right) \tag{2.3}$$

In the context of LEO plasma-body interactions, the interaction may be considered electrostatic and unmagnetised [38, 44, 46, 63]. Under these assumptions, Maxwell's equations reduce to Poisson's equation for the electric potential ϕ,

$$\mathbf{E} = -\nabla\phi, \;\; \nabla^2\phi = -\frac{\rho_c}{\varepsilon_0} \tag{2.4}$$

where ε_0 is the permittivity of free space and ρ_c is the macroscopic space-charge density,

$$\rho_c = \sum_k q_k \int f_k d\mathbf{c}_k = \sum_k q_k n_k \tag{2.5}$$

Determining the general particle distribution of a system with multiple reacting species in the presence of external and self-consistent forces is the challenge posed by kinetic theory. Direct solutions of the Boltzmann equation are intractable for practical systems. PIC [64] and DSMC [65] methods avoid solving the Boltzmann equation directly by simulating the microscopic interactions of super-particles.

2.1.2 The Direct Simulation Monte Carlo Method

The DSMC method describes collision dominated systems ($\Lambda \ll 1$) i.e. systems where the collision kernel $(\partial f_k/\partial t)_{coll}$ drives the evolution of f_k [65]. Applying the *"molecular chaos"* assumption[2], the basis of the DSMC method is the *ad hoc* assumption that particle motion and collisions are decoupled over the small time-step Δt [65]. During a DSMC *"push"* step, simulated macro-particles are moved ballistically over Δt. During the collision step, Markov processes, implied by the molecular chaos assumption, describe the interaction of super-particles according to kinetic theory [62, 67]. Phenomenological collision models[3] approximate the physical interaction to varying degrees

[2] The molecular chaos assumption is that *"velocities of colliding particles are uncorrelated, and independent of position"* [66]

[3] Semi-empirical models with physical arguments designed to reproduce macroscopic properties from microscopic interactions.

of fidelity (see Hard Sphere (HS), Variable Hard Sphere (VHS), and Variable Soft Sphere (VSS) described in [65]). Macroscopic properties are then sampled directly from the particle distribution, as in Eqn. 2.1, by applying time-averaging or ensemble-averaging for steady-state or transient systems respectively.

A common feature in most DSMC collision procedures involves the sorting of macro-particles into *"collision cells"* [57, 68], the exception being gridless DSMC methods [69, 70]. In collision cell approaches, candidate collision pairs are selected from a computational cell based on collision rates described by kinetic theory [65]. Collision pairs then undergo an acceptance-rejection test e.g. the No-Time-Counter (NTC) method [65]. The basis of the NTC method lies in determining the differential scattering cross-section (σ) between particles p and q i.e. σ_{pq}. Calculation of σ_{pq} is through a phenomenological model, where semi-empirical coefficients are tuned to match collision rates and viscosity coefficients at a reference temperature ($(T_{ref})_{pq}$). A list of VHS and VSS coefficients may be found in [68].

2.1.3 The Particle-in-Cell Method

The PIC method determines solutions to the Vlasov-Maxwell system where the contribution of collisions in Eqn. 2.2 are neglected i.e. collective dominated systems ($\Lambda \gg 1$). The numerical realisation of the PIC method is similar to the DSMC method. Super-particle trajectories are traced through time using appropriate integration techniques e.g. the Leapfrog or Boris methods [71]. ρ_c is calculated by weighting the contribution of macro-particles p to a computational mesh with nodes n according to some shaping function S and *vice versa* [64] . The processes of determining ρ_c and $\mathbf{E}$ at a super-particle are referred to as the *"assignment"* and *"interpolation"* steps respectively. Figure 2.1 illustrates the concept of charge assignment in one dimension, higher order shaping functions available to reduce numerical fluctuations in ρ_c as particles traverse cells [64].

$$\rho_c(n) = \sum_p q_p S(\mathbf{x}_n - \mathbf{x}_p) \tag{2.6}$$

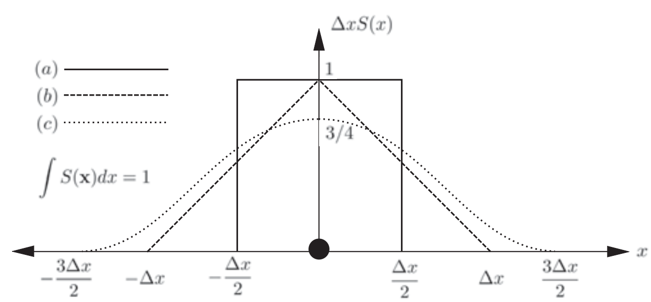

Figure 2.1: Shaping functions for charge and fields: (a) nearest grid point; (b) linear; (c) second-order.

While a variety of approaches have been developed to capture increasingly higher order shaping effects with reduced computational cost necessary for electromagnetic and relativistic PIC codes [72–74], the comprehensive review of numerical issues inherent in coupling particle and field domains through S by Birdsall and Langdon [64] remains the relevant treatise on the subject for electrostatic PIC codes, such as that used in this work. The key points are: the shaping functions must conserve charge between assignment and interpolation steps; and the same shaping function should be applied between the assignment and interpolation steps to avoid numerical self-forcing (self-forcing being a purely numerical force on a particle caused by its own charge [64]).

2.2 Overview of pdFOAM

pdFOAM supports both fully-kinetic (FK) and hybrid-fluid kinetic (HK) simulations. FK simulations model neutral, ion, and electron particle distributions directly; HK simulations approximate the electron particle distribution by a non-linear Boltzmann electron fluid (EF). The advantage of the HK approach is a significant reduction in computational expense compared to FK simulations, but at the expense of physical fidelity i.e. electron kinetic phenomena. Both HK and FK simulations begin by solving for **E** given an initial particle distribution and use this field to set up the Leapfrog method, a time-centered particle integration technique [64]. At this point the computational cycle outlined in Figure 2.2 begins (the italicised processes are those that have been developed and implemented here):

1. Particles are pushed to a new position and boundary models are applied. The particle tracking algorithm is described in Macpherson, Niklas, and Weller [75].
2. Cell occupancy is updated to include boundary interactions e.g. particle injection, deletion, reaction.
3. Collision partners are selected. *To reconcile disparate spatial discretisation requirements of the PIC and DSMC methods pdFOAM implements a new collision selection procedure developed here (the Transient Conglomerated Cell (TCC) method.*
4. Collision pairs are collided. pdFOAM supports HS, VHS and VSS phenomenological collision models, including reactions, with the Larsen-Borgnakke and Quantum-Kinetic (Q-K) energy redistribution models [76].
5. Particle cell occupancy is updated to account for the creation/annihilation of reacting particles.
6. *Charge is weighted to the mesh domain to determine ρ_c. pdFOAM supports nearest volume (NV) and Composite Linear Volume (CLV) shaping functions.*
7. *Poisson's equation is solved using a preconditioned conjugate gradient (PCG) Finite Volume Method (FVM) supplied in OpenFOAM [56]. Newton's method is used in HK simulations to solve the non-linear contribution of the Boltzmann electron fluid.*
8. *Fields are weighted to particles using the inverse shaping function of step 6.*

The above process is repeated until the system either achieves a *steady-state*, is identified as *transient*, or reaches a predefined end condition e.g. end time. In this work, we define steady-state as when the total number of particles, charge in the system, and the linear kinetic and potential energy of the system achieves a dynamic equilibrium.

2.2.1 Numerical Methods in pdFOAM

Composite Linear Volume Method

The composite linear volume method applies multiple linear weighting functions to transform from particle to cell nodes and then cell nodes to cell volumes in logical space (l). The physical to logical space transformation uses the tri-linear interpolation method described in [77]. The concept of performing particle assignment and interpolation in PIC codes has been successfully demonstrated by the CPIC [78] and DEMOCRITUS [63] codes.

The charge assignment step determines the inverse linear volume weighting centred at the particle position to cell vertices. The charge is then distributed to surrounding cell vertices and weighted to the surrounding volumes. After solving for the field distribution, fields are interpolated back to particle positions using the inverse the charge assignment process e.g given the cell occupied by the particle, the surrounding cell nodes gather volume weighted fractions of surrounding field quantities and then interpolate these back onto the particle using a linear volume gather (summation instead of decomposition). Figure 2.3 illustrates the charge assignment and field interpolation

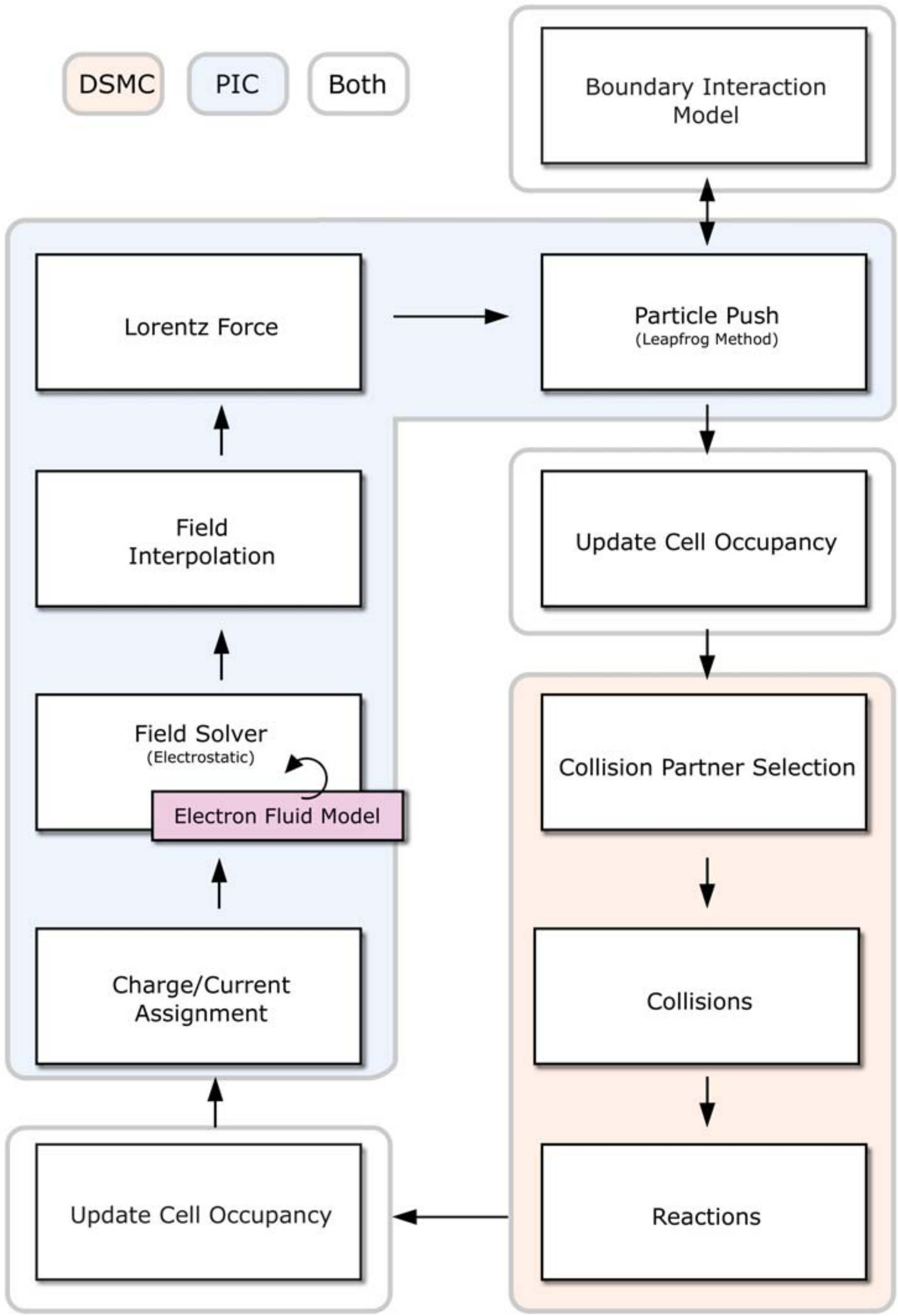

Figure 2.2: Standard computational cycle in pdFOAM with DSMC, PIC and PIC-DSMC methods colored

processes with the linear weighting function shown in Eqn. 2.7,

$$\begin{aligned}
\rho_{c_n}(i,j) &= \frac{q_i}{A_c}\frac{(\Delta x - x)(\Delta y - y)}{\Delta x \Delta y}, \quad & \rho_{c_n}(i+1,j) &= \frac{q_i}{A_c}\frac{x(\Delta y - y)}{\Delta x \Delta y} \\
\rho_{c_n}(i,j+1) &= \frac{q_i}{A_c}\frac{(\Delta x - x)y}{\Delta x \Delta y}, \quad & \rho_{c_n}(i+1,j+1) &= \frac{q_i}{A_c}\frac{xy}{\Delta x \Delta y}
\end{aligned} \tag{2.7}$$

The advantage of the composite linear volume method is that it allows the use of cell-centered numerical methods without needing to employ co-located or staggered meshes, while also facilitating parallelisation in OpenFOAM. The composite linear volume method fills the niche for cell-centered data on a single grid at the expense of an increased computation cost compared to the co-located grid approach - OpenFOAM does not currently support co-located or staggered grids. As an alternative, pdFOAM also includes a nearest volume approach were charge is assumed to be uniformly distributed within the cell occupied by the particle - equivalent to a Nearest-Grid-Point (NGP) approach. At the expense of physical fidelity, the nearest volume offers a significantly faster alternative to the CLV method in pdFOAM.

To illustrate the effect of the composite linear volume and nearest volume shaping functions on particle motion (also know as *"aliasing"*), Figure 2.4 plots the oscillation of an electron about a stationary ion in position-velocity phase space compared against theory predicted by pdFOAM and compared against theory. Motion in X demonstrates that neither method adds a significant amount of numerical energy over the simulated period i.e. the oscillation amplitude remaining constant. Motion in u_x illustrates the aliasing effect of the nearest volume method, the x-axis acceleration a_x constant throughout each cell and 0 in the central cell. Comparatively, the CLV method provides a significantly better approximation of the electron's motion.

It should be noted that Figure 2.4 shows the best case where the ion is at a cell center. Disagreements between the nearest volume method and theory increase when the ion is not at a cell center (the composite linear volume method still provides a good match with theory). It should also be noted that PIC methods are generally not used to study single particle motion but instead plasma collective phenomena. The main purpose of Figure 2.4 is to demonstrate that the shaping functions do not add numerical energy to the system, which they do not.

Non-Linear Boltzmann Electron Fluid Model

Directly simulating electrons comes at a significant computational cost. To maintain numerical stability, Δt must be smaller than the fastest plasma frequency ω_p i.e. $\Delta t < \omega$ [62] [4]. In a similar manner, the stability requirements of the Leapfrog method (see Hockney and Eastwood [71]) require a spatial discretisation (Δx) of $\Delta x < \lambda_{D,e}/2$. As a result, the numerical requirements of FK-PIC simulations are limited by electron length and time scales i.e. the electron Debye length $\lambda_{D,e}$ and plasma frequency $\omega_{p,e}$. Hence, the numerical cost of PIC simulations can be significantly reduced if the electron distribution can be approximated by a fluid i.e. a Hybrid Fluid-Kinetic PIC simulations (HK-PIC). HK-PIC simulations benefit from an increase in allowable time-step, cell-size and reduction in simulated particles (no electrons) at the expense of solving an extra set of equations to capture the electron fluid. In most cases, the benefits of HK-PIC simulations outweigh the cost of solving for the electron fluid distribution.

The approach taken here for HK-PIC simulations is to assume that the electron distribution function can be described by an isothermal, currentless (electrostatic), unmagnetised ($\mathbf{B} = 0$), inertia-less ($m_e/m_i \to 0$) electron fluid; this approach has been used successfully for the study of

[4] $\Delta t < 0.01\omega$ is often used in FK-PIC simulations to avoid numerical heating of the electron distribution [64].

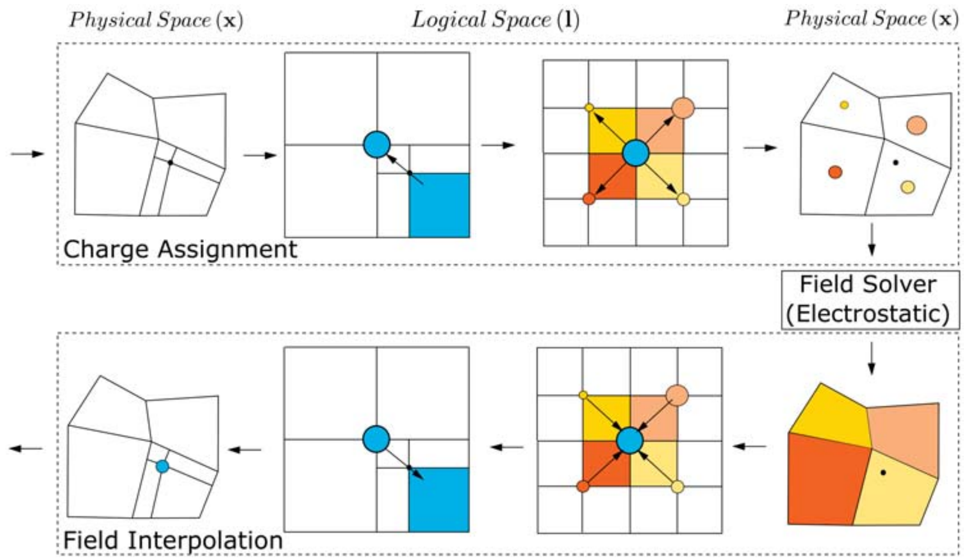

Figure 2.3: Illustration of Composite Linear Volume (CLV) method applied in charge assignment and field interpolation steps. Only the process for a single node/particle is shown for brevity.

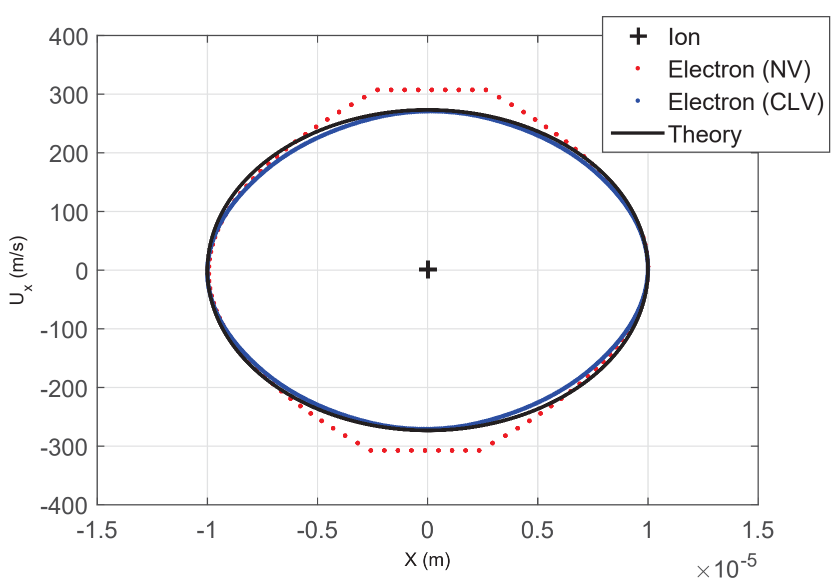

Figure 2.4: Theoretical 1D electron oscillation about stationary ion compared to observed oscillation in pdFOAM for the Composite Linear Volume (CLV) and Nearest Volume (NV) methods in position-velocity phase-space.

plasma-body interaction in a charging/arcing context [50] and in the analysis of plasma thrusters [79]. Under these assumptions, magnetohydrodynamic equations of continuity, momentum, and energy reduce to [79],

$$n_e = n_{e,\infty} \exp\left[\frac{q_e \phi(\mathbf{x}) - \phi_\infty}{k_B T_e}\right] \tag{2.8}$$

where k_B is the Boltzmann constant, T_e is the electron temperature, $n_{e,\infty}$ is the freestream electron number density and ϕ_∞ is the freestream potential (assuming a quasi-neutral freestream $\phi_\infty \approx 0$).

Poisson's equation then becomes a non-linear function of potential,

$$\varepsilon_0 \nabla^2 \phi - q_e n_{e,\infty} \exp\left[\frac{q_e \phi}{k_B T_e}\right] = -q_i n_i \tag{2.9}$$

Applying Newton's method, solutions to Eqn. 2.9 become an iterative process in t,

$$\left(\varepsilon_0 \nabla^2 - \frac{\varepsilon_0}{\lambda_{D,e}^2} \exp\left[\frac{q_e \phi^{(t)}}{k_B T_e}\right]\right) \phi^{(t+1)} = -q_i n_i + \left(q_e n_{e,\infty} - \frac{1}{\lambda_{D,e}^2} \phi^{(t)}\right) \exp\left[\frac{q_e \phi^{(t)}}{k_B T_e}\right] \tag{2.10}$$

Hockney and Eastwood [71] demonstrated that the convergence of Eqn. 2.10 is quadratic provided the initial guess is sufficiently near the solution; this is the case for time-stepping simulations, such as the PIC method, where the initial solution t at time-step n is taken as the converged solution at $n-1$.

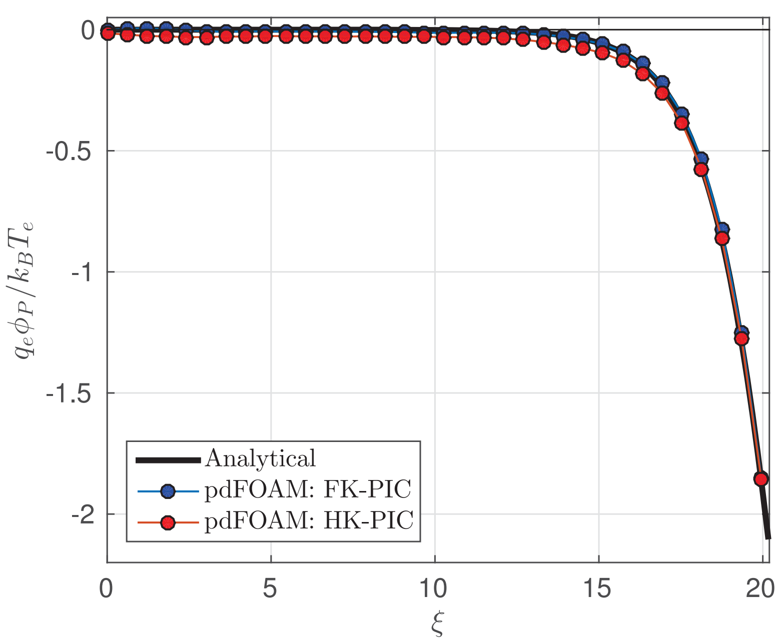

Figure 2.5: Comparison of numerical sheath structure, calculated by FK-PIC and HK-PIC simulations in pdFOAM, and analytical sheath structure, calculated using the method described in Appendix appdendixA. Ion acoustic Mach number M_i is 2.1.

Figure 2.5 compares the one-dimensional sheath structure formed near a flat plate in a flowing plasma predicted by HK-PIC and FK-PIC simulations against theory. Figure 2.5 demonstrates that the structure of FK-PIC and HK-PIC simulations closely match theoretical predictions, the FK-PIC simulation exhibiting a source sheath structure caused by the refluxing electrons (electrons repelled by the sheath) meeting the inflowing electrons at the boundary i.e. the source sheath is a numerical boundary phenomenon. A detailed investigation of this phenomenon can be found in Birdsall and Langdon [64].

Transient Conglomerated Cell Method

The numerical requirements of DSMC and PIC methods differ. While both approaches are stochastic as a result of their particle nature, the acceptance/rejection scheme in the DSMC collision step applies a further stochastic method compared to the PIC method. DSMC best practice is to maintain a constant number of particles per cell throughout the flowfield to avoid numerically biasing a particular region [68]. Furthermore, the size of collision cells should not exceed $\lambda/3$ [68]. PIC cells must satisfy the requirement $\Delta x < \lambda_{D,e}/2$ in order for the leapfrog method to remain stable [71]. Hence, in general, PIC requirements limit PIC-DSMC simulations. As a result, PIC-DSMC simulations using a single mesh require orders of magnitude more particles than pure DSMC simulations to satisfy both the particles per cell and $\Delta x < \lambda_{D,e}/2$ requirements.

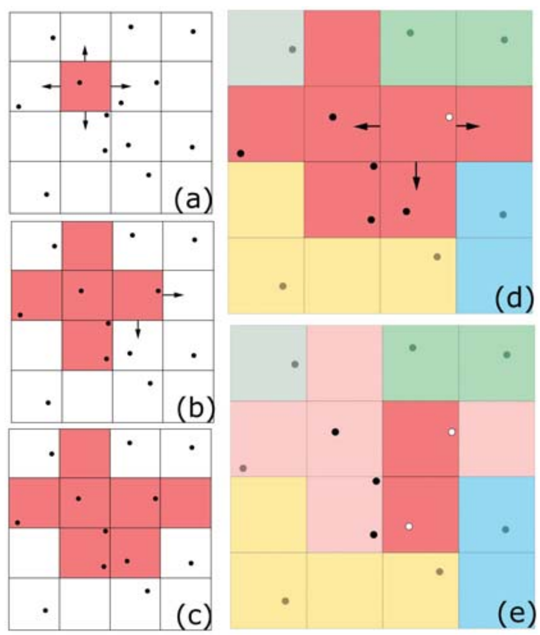

Figure 2.6: TCC collision cell procedure: (a) Collision cell construction begins, (b) Cells with common faces are added to collision cell, (c) Cells are iteratively added until construction requirements are met, (d) Cells surrounding candidate are searched (e) Closest cell containing collision candidates is selected and a partner randomly chosen.

Several approaches have been proposed to reconcile the numerical requirements of the PIC and DSMC method [70, 80]. The Transient Conglomerated Cell (TCC) method developed and implemented here in pdFOAM has been adapted from the approach taken in the DSMC codes DS2V/3V [68]. DS2/3V uses a fine background mesh to construct collision cells from a conglomeration of sub-cells about randomly scattered node points. Similarly, the TCC method constructs collision cells from the PIC mesh based on the instantaneous particle distribution at each time-step. Cell clusters are built by iterating out through cells with common face indices as illustrated in Figure 2.6 (a) - (c).

The TCC method promotes nearest neighbour collisions by preferentially searching the collision cell decomposition to minimise mean collision distance. Figure 2.6 (d) and (e) illustrates the TCC collision partner selection procedure. First, a collision candidate p is selected randomly from the collision cell. Next, adjacent collision sub-cells are iteratively searched to find the nearest cell containing particles. A collision candidate q is then randomly selected from this sub-cell.

As only an integer number of collisions may occur during a time-step, the remainder is isotropically distributed over the collision cell's sub-cells and carried forward to the next time-step. By linking the collision remainder to the mesh instead of collision cell index, the random motion of the collision cell index compared to physical location does not cause the transport of collisions to non-physical locations.

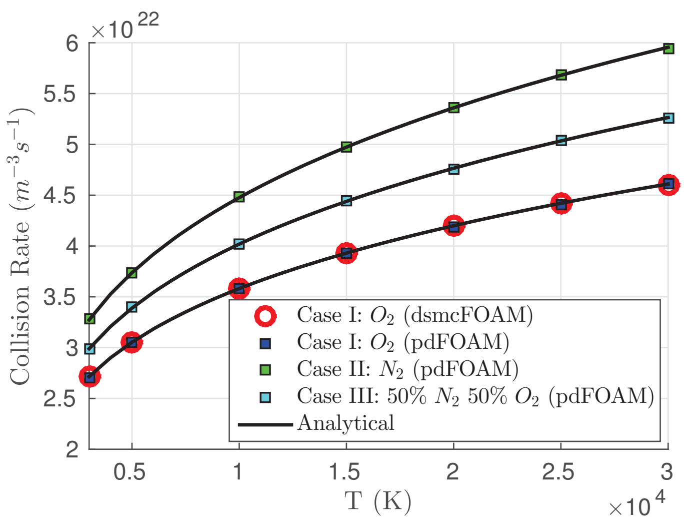

Figure 2.7: Comparison of numerical and theoretical collision rates using the TCC method.

Figure 2.7 compares theoretical collision rates for three gases with increasing temperature calculated using the standard collision selection procedure in dsmcFOAM and the TCC method implemented here in pdFOAM. Figure 2.7 demonstrates the ability of the TCC method to correctly reproduced analytical collision rates in both single species and gas mixtures. The advantages of the TCC method are detailed further in Section 2.3.

2.2.2 Guidelines for PIC simulations in pdFOAM

Birdsall and Langdon [64] and Hockney and Eastwood [71] presented extensive studies into numerical effects caused by the discretization of a plasma into super-particles (see also Melzani et al. [81]. These studies include the stability of the particle movers, aliasing effects caused by particle shaping functions, and the effect of statistical fluctuations caused by an insufficient number of simulation particles. To minimise numerical effects the following general rules guide PIC simulations presented in this work:

1. The time-step Δt must be smaller than the time-scales scales of studied phenomena e.g. the electron plasma frequency ω_{pe} that describes the oscillation frequency of electrons in FK-PIC simulations.

2. The time-step Δt must be sufficiently small such that particles do not jump multiple cells i.e. $\Delta t < \Delta x / v_i$
3. Δx must both resolve length scales of studied phenomena and satisfy the stability requirement $\Delta x < \lambda_{D,e}/2$.
4. If thermal effects are considered, ensure there is a sufficient representation of high energy species by demonstrating the independence of results on super-particle density.
5. The plasma should remain collisionless i.e. if collision rates become significant ion-neutral collisions must be modelled with the DSMC portion of the code.
6. A sufficient number of particles per cell should be maintained to minimise numerical fluctuations. This should be tested case by case by demonstrating the independence of results the on the number of particles per cell (achieved by varying the number of real particles represented by each simulated particle).
7. Demonstrate independence of numerical solution from mesh topology.

All simulations presented in this work assume a steady-state solution. Steady-state is defined as having been reached when the number of particles, charge in the system and linear kinetic energy of the system reach some dynamic equilibrium. In the case of self-consistent charging simulations, floating potential is also used to identify when steady-state has been achieved.

2.3 Validation of pdFOAM

Section 2.2 described the implementation of the PIC method in pdFOAM and presented the validation of several novel numerical methods implemented here. This Section further develops confidence in the ability of pdFOAM to model the interaction of LEO objects with the space environment with two studies that verify the ensemble implementation of the PIC and DSMC methods in pdFOAM:

1. The Mach 10 $Kn = 0.25$ cylinder case from [82] is repeated and compared with data from MONACO [83], an established DSMC code.
2. The self-consistent charging of a flat plate and a cylinder in a flowing, collisionless, unmagnetised plasma is compared to theoretical predictions of floating potential at different ion drift velocities. Predictions are compared against those made by the PIC code, PICLas [59].

2.3.1 Simulation Topology

The following simulations are 2D and use a common cylinder topology with body radius r_B as illustrated in Figure 2.8. Figure 2.8 lists particle and field boundary conditions, while case specific boundary conditions are described in the appropriate sections.

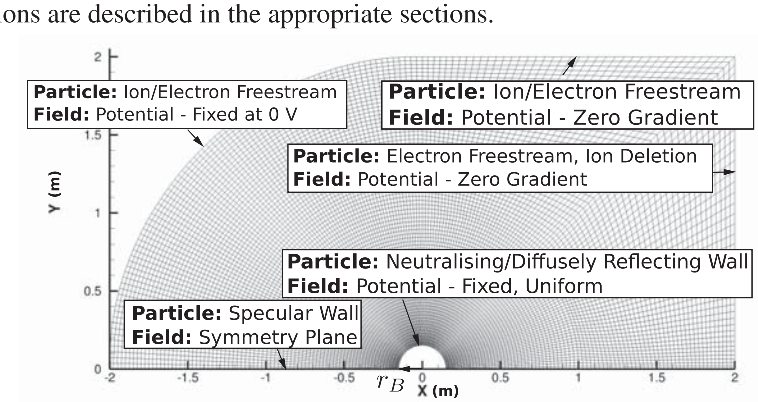

Figure 2.8: Domain topology and boundary conditions. Every 10th grid node displayed for clarity.

2.3.2 Hypersonic Cylinder

Lofthouse, Boyd, and Wright [82] investigated the breakdown of the continuum assumption on the aerothermodynamics of a hypersonic cylinder in a reacting flow. They investigated a Mach (M) 10 flow of Argon (Ar) over a two-dimensional, 12 in (0.3048 m) diameter cylinder with a fixed surface temperature of 500 K for a variety of Kn by varying the freestream number density (n_∞). The purpose of this validation case is to demonstrate that pdFOAM retains the ability of its underlying DSMC capability to predict rarefied gas dynamics and in particular gas-surface interactions. While the nature of these gas-surface interactions will likely differ from plasma-surface interactions, they serve as an appropriate approximation in the context of this work. The assumption being that, upon colliding with the object surface they are neutralised and re-emitted diffusely (as a normal neutral gas-surface interaction). Additional plasma effects may include the secondary emission of electrons (ion collisions cause the secondary ejection of electrons from the surface) and sputtering (ion collisions cause the secondary emission of surface atoms/molecules). These phenomena are not considered in this work to isolate the underlying physics of plasma-body interactions in LEO to quantify whether ionospheric aerodynamic is significant compared to neutral aerodynamics.

Numerical Setup

Freestream number density, temperature and velocity are $1.699 \times 10^{19} m^{-3}$, $200K$ and $2634.1 m/s$ respectively. Gas-surface interactions are that of a diffusely reflecting wall with complete thermal accommodation to a fixed surface temperature of $500K$. VHS coefficients are $T_{ref} = 1000K$, $d_{ref} = 3.959 \times 10^{-10} m$, and $\omega = 0.734$ to be consistent with [82].

Results and Discussion

The total linear kinetic energy and number of simulated macro-particles achieved a dynamic equilibrium (steady-state) after $10,000$ time-steps, with 1.6 million macro-particles in the system. At steady-state there were ≈ 1500 collision cells and a 99.9% reduction in calls to the collision partner selection procedure compared to the full mesh (≈ 4 million cells). Results were sampled over $60,000$ time-steps after the steady-state had been reached to reduce statistical fluctuations. Figure 2.9 visualises the conglomerated collision cells constructed in the fore-body (bottom left) and rear (bottom right) of the cylinder on the full mesh. Clustering of collision cells in Figure 2.9 demonstrates the ability of the TCC method to capture high and low-density regions as well as the transition region with no *a priori* knowledge of the flow.

Figure 2.10 compares contours of temperature between pdFOAM (top) and MONACO (bottom). Figure 2.11 compares the surface pressure (c_P) and heat flux (c_H) coefficients.

$$c_P = \frac{2\left(P - P_\infty\right)}{\rho_\infty u_\infty^2} \quad c_H = \frac{2Q}{\rho_{m_\infty} u_\infty^3} \tag{2.11}$$

where P is pressure, Q heat flux and ρ_m is the mass density.

There is good agreement between pdFOAM and MONACO - differences being a small increase in peak translational temperature in the ram position in the pdFOAM simulation and an extension of the warm wake region. Both the small increase in peak heating and extension of the wake region are believed to be a reflection of different collision selection procedures causing a small difference in localised viscosity. A drawback of the TCC method is the use of small cells resulting in higher numerical fluctuations caused by a comparatively lower number of particles per sampling cell than in MONACO. However, as the basis of the TCC method is to reconcile PIC and DSMC spatial requirements, PIC being significantly smaller than DSMC, this is expected.

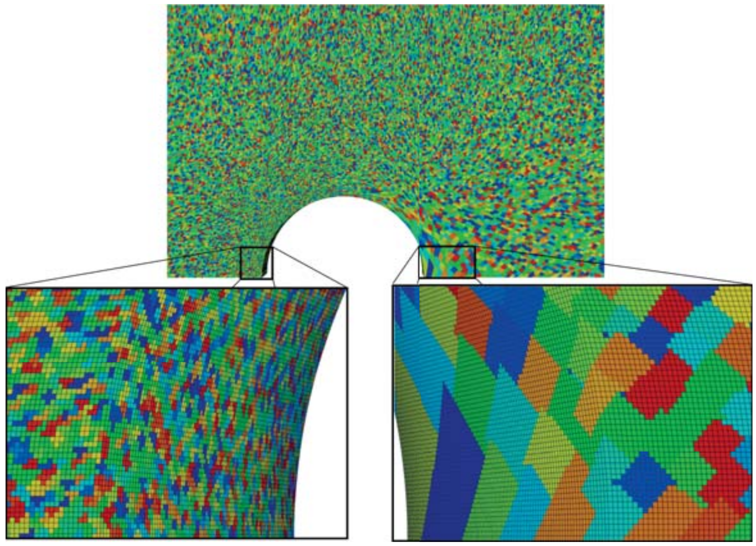

Figure 2.9: Visualisation of collision cells. Colours are random.

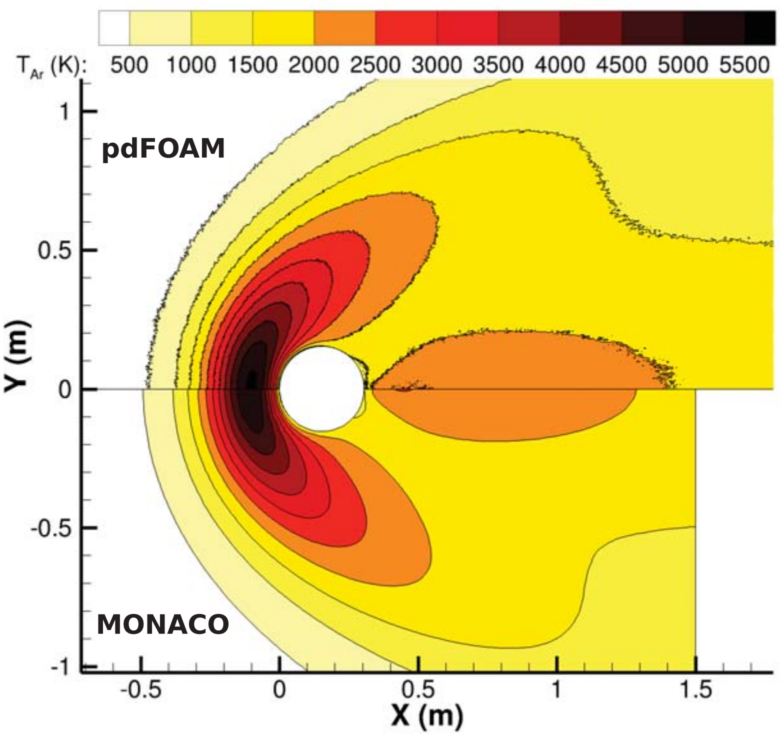

Figure 2.10: Contours of temperature: pdFOAM (top) and MONACO (bottom)

Comparing surface properties, pdFOAM over-predicts peak c_P by 2.27% and under-predicts peak c_H by 2.7% compared to MONACO. A comparison of MONACO with other established DSMC codes for the $Kn = 0.002$ case in [82] shows that a 2.7% under-prediction of peak c_H is within the code-to-code uncertainty reported in Bird [84]. Similarly, the distribution of coefficients is similar, the over-prediction of c_P likely due to the different apparent viscosity caused by different collision selection procedures. Overall, pdFOAM is able to reproduce the interaction from [82] and in particular the surface force distribution. This later result is important in a charged aerodynamic context, the purpose of this validation case primarily being to demonstrate the ability of pdFOAM to correctly predict forces due to gas-surface interactions. Based on results in Figure 2.11, confidence can be placed in pdFOAM's ability to accurately capture diffusely reflecting gas-surface interactions.

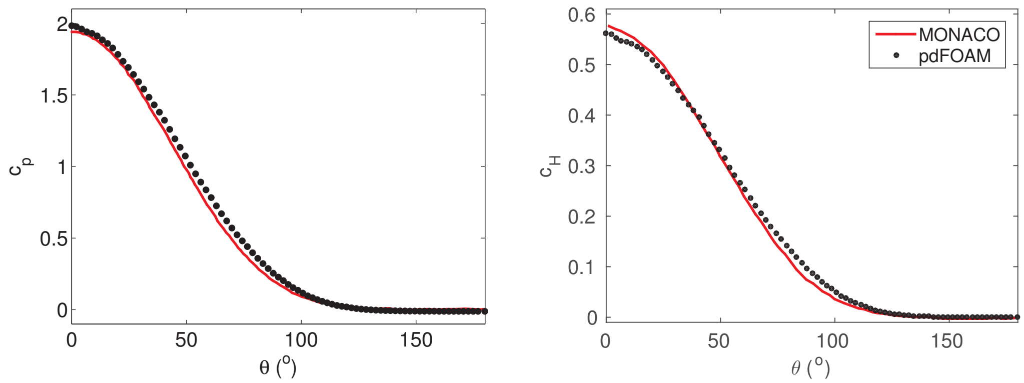

Figure 2.11: Comparison of pdFOAM and MONACO surface distributions.

2.3.3 Self-Consistent Charging in a Flowing Plasma

The self-consistent charging of a body immersed in plasma is a complex problem in plasma physics [17, 21, 85]. Validation of pdFOAM's PIC method has included unbounded plasma kinetic phenomena (two-stream instability) and bounded plasma-body interactions (planar sheath structure)). Self-consistent charging requires accurate replication of both kinetic and boundary phenomena to reproduce the electron and ion current balance needed to achieve a dynamic equilibrium at floating potential ϕ_B.

pdFOAM supports both absorbing and catalytic walls - the former deleting incident particles, the latter transforming them into one or more particles. Reflected particles may be re-emitted in either a diffuse or specular manner with a degree of thermal accommodation to the wall. pdFOAM treats wall charging in one of three ways: as a perfectly conducting wall where charge is distributed evenly across the surface before calculating fields (the effect of surface currents on the system is neglected); as a perfectly insulating wall where charge accumulates on wall cell faces and does not transport about the surface (arcing is not currently considered); as a fixed potential wall where charge is absorbed, and the surface potential remains fixed based on initial conditions.

The following validation cases compare the numerical floating potential of a conducting flat plate (one-dimensional) and cylinder (two-dimensional) in a drifting plasma predicted by pdFOAM with established theoretical relationships developed to analyse plasma probe measurements. As such, Section 2.3.3 provides a discussion of charging theory, Section 2.3.3 outlines the numerical setup and Section 2.3.3 presents the results. The implementation of more advanced wall boundary conditions to include effects such as secondary electron emission and sputtering is the subject of ongoing work. The above boundary conditions sufficient for enabling the study of LEO plasma-body interactions in this work.

Background: Charging in a Flowing Plasma

Consider the charging of a large, perfectly conducting, flat plate in a collisionless, unmagnetised, single ion species plasma, with ion drift velocity u_∞. The electron current (I_e) from random particle flux per unit surface area to a surface with potential ϕ_B can be written as [44],

$$I_e = q_e n_{e_\infty} \left(\frac{8T_e k_B}{\pi m_e}\right)^{1/2} \exp\left[-\frac{q_e \phi(\phi_B)}{k_B T_e}\right] \tag{2.12}$$

As ion thermal velocity $u_{t,i} \rightarrow u_\infty$, the ion velocity distribution is described by a shifted-Maxwellian function [86],

$$f_i(v) = \left(\frac{m}{2\pi k_B T_i}\right)^{1/2} \exp\left[-\frac{m(v-u_\infty)^2}{2k_B T_i}\right] \tag{2.13}$$

where ion current (I_i) is given by,

$$I_i = q_e n_{i_\infty} \int_0^\infty v f_i(v) d^3v \tag{2.14}$$

For a flat plate, Eqn. 2.14 becomes [44],

$$I_i = q_e n_{i_\infty} u_\infty \frac{1}{2}\left(1 + \text{erf}[y] + \frac{1}{\sqrt{\pi}S_i}\exp\left[-S_i^2\right]\right), \quad S_i = u_\infty \left(\frac{2k_B T_i}{m_i}\right)^{-1/2} \tag{2.15}$$

Here S_i is the ion drift ratio, and the system reaches an electrical dynamic equilibrium when $I_i = I_e$. Equating Eqn. 2.12 and Eqn. 2.15, the floating potential of a large flat plate in a drifting plasma is described by,

$$\begin{aligned} \phi_p &= \frac{k_B T_e}{q_e}\left(\ln(f) - \ln\left(\sqrt{\frac{m_i}{2\pi m_e}}\right)\right), \\ f &= \frac{S_i}{\sqrt{2}}\left(1 + \text{erf}(S_i) + \frac{1}{S_i\sqrt{\pi}}\exp\left[-S_i^2\right]\right) \end{aligned} \tag{2.16}$$

The charging of a cylinder in a collisionless, unmagnetised, single species plasma, with drift velocity u_∞, is similar to the flat plate case but must also take into account conservation of angular momentum of ions about the body. In the OML regime, Hoegy and Wharton [87] demonstrated that I_i can be approximated as,

$$I_i = I_{i,t}\frac{2}{\pi^{1/2}}\left(|\Phi| + S_i^2 + \frac{1}{2}\frac{|\Phi| + 1/2S_i^2}{|\Phi| + S_i^2}\right)^{1/2}, \quad |\Phi| + S_i^2 > 0, \Phi = \frac{q_e \phi_B}{k_B T_e} \tag{2.17}$$

where $I_{i,t}$ is the random ion thermal current to the surface with area A,

$$I_{i,t} = A q_e n_i \sqrt{\frac{k_B T_i}{2\pi m_i}} \tag{2.18}$$

The electron current, similar to Eqn. 2.12, is given by,

$$I_e = A q_e n_e \sqrt{\frac{k_B T_e}{2\pi m_e}} \exp\left[-\frac{q_e \phi(\phi_B)}{k_B T_e}\right] \tag{2.19}$$

Equating Eqn. 2.17 and Eqn. 2.19, the floating potential for a given condition may be solved numerically - Newton's method is used in this work [71].

Numerical Setup

Flow and numerical properties for the flat plate and 0.3 m radius cylinder charging cases are listed in Table 2.1. Cylinder flow conditions are taken from Hastings [17] and represent the average conditions experienced by the EOS during a period of mean sunspot activity. Flat plate conditions are based on similar work in Delzanno et al. [78]. Gas-surface interactions used in both flat plate and cylinder charging simulations are those of a perfectly conducting, absorbing wall, where incident particles are neutralised and removed from the simulation; this is appropriate as the system is collisionless. All simulations are fully-kinetic. At steady-state, simulations are time-averaged over $10,000$ time-steps to reduce the statistical scatter of the data. Simulated floating potentials are then compared against analytical predictions calculated using the methods described above, the floating potential occurs at the point where $I_i = I_e$.

Table 2.1: Computational parameters for charging simualtions

	Flat Plate	Cylinder
Plasma Parameters		
$n_{i/e,\infty}$ (m^{-3}	1×10^{12}	4×10^{10}
T_i (K)	1000	1537
T_e (K)	1000	1997
Gas Properties		
Species	H^+	O^+
m (kg)	1.67×10^{-27}	26.55×10^{-27}
Computational Parameters		
ρ_{part}	2	45
Δt (s)	2.5×10^{-9}	5×10^{-9}
Case	$u_{H^+,\infty}$ (m/s)	$u_{O^+,\infty}$ (m/s)
I	0	0
II	6038	2722
III	11501	5445
IV	-	7500
V	-	9076

Results and Discussion

Figure 2.12 compares theoretical floating potentials for a flat plate and a 0.03 m radius cylinder with those predicted by pdFOAM. Charging simulations using the conditions listed in Table 2.1 using PIC-DSMC code, *PICLas*, provided by T. Binder (personal communications, 13/12/2016) are included for comparisons. There is excellent agreement between theory and simulated floating potentials for all flat plate cases. Cylinder floating potential are well predicted for all $S_i > 2$, the maximum disagreement between pdFOAM and PICLas being 0.25%. The mean floating potential at $S_i = 0$ is under-predicted by both pdFOAM and PICLas when compared to Hoegy and Wharton [87]. However, fluctuations in floating potential were observed in both pdFOAM and PICLas for the $S_i = 0$ case suggesting either the presence of time-dependent phenomena or that the system is numerically sensitive. One explanation for the under-prediction of floating potential for the stationary case is the presence of ion absorption barriers.

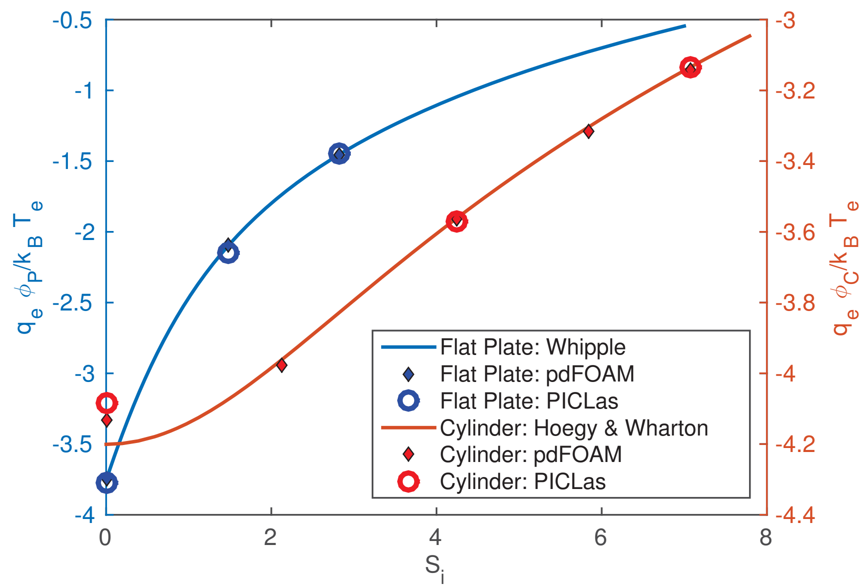

Figure 2.12: Comparison of floating potential in a flowing plasma predicted by pdFOAM (diamonds) and PICLas (circles) for the flat plate (blue) and cylinder (red) cases compared against theory.

For example, Delzanno et al. [78] performed a similar charging simulation on an axi-symmetric sphere using the PIC code, CPIC. Delzanno et al. [78] observed a 1.6% over-prediction in floating potential when compared to OML based predictions (compared to a 1.6% under-prediction by pdFOAM for the cylinder case seen in Figure 2.12). OML assumptions do not capture the absorption barrier phenomena discussed (for example) in Al'Pert, Gurevich, and Pitaevskii [88], Allen [36] and Fortov et al. [89]. This is reflected in Delzanno et al. [78] and the stationary cylinder case presented here as the over and under-prediction of the floating potential. As the relative kinetic energy of the flow increases, the effect of ion absorption barriers decreases and the floating potential approaches Eqn. 2.17, supporting the assertion in Hoegy and Wharton [87] that Eqn. 2.17 is valid for $\Phi + S_i^2 > 0$ (see also McMahon, Xu, and Laframboise [39]). We therefore conclude that pdFOAM accurately reproduces the self-consistent charging interaction of a perfectly conducting flat plate and a cylinder in a flowing plasma and, therefore, the underling plasma sheath structure required to achieve this floating potential.

2.4 Summary

The use of OML type assumptions regarding sheath structure is as a key limitation of ionospheric aerodynamic literature. To address this limitation, the Particle-in-Cell (PIC) method was identified as an appropriate numerical method for capturing the self-consistent sheath structure surrounding an object immersed in a mesothermal plasma flow. The purpose of this chapter was to describe the implementation of the PIC method within the hybrid PIC-DSMC code, pdFOAM, developed here as the primary research tool used throughout this work.

pdFOAM is limited to electrostatic, non-relativistic plasma simulations; sufficient for the scope of this work. To demonstrate that pdFOAM can be used confidently to capture the underlying physics of charged aerodynamics, two validation cases were presented in this chapter. The first validation case demonstrated the ability of pdFOAM to predict the forces on a body caused by diffusely reflecting gas-surface interactions thermalised to a 500 K wall when compared with the established DSMC code, MONACO i.e. direct aerodynamics forces. A 2.2% over-prediction of peak surface pressure coefficient when compared to MONACO was observed. This over-prediction is within the uncertainty seen in similar DSMC code-to-code comparisons and pdFOAM was concluded to correctly capture direct aerodynamic surface forces to the same level of accuracy as other DSMC codes, and to the level needed to be able to explore flow physics and extract underlying phenomena.

The second validation case demonstrated the ability of pdFOAM to predict the self-consistent floating potential of a flat plate and a cylinder in a flowing plasma when compared against both probe theory and the PIC code, PICLas. By reproducing the self-consistent floating potential, this validation case developed confidence in the ability of pdFOAM to capture the physical structure of the plasma sheath of mesothermal plasma-body interactions and, therefore, address one of the limitations of past charged aerodynamic analyses. While excellent agreement was observed for mesothermal flows, the floating potential was under-predicted by both pdFOAM and PICLas for a quiescent plasma when compared against probe theory. Comparisons with a similar floating potential study of a sphere suggest this under-prediction is caused by ion absorption barriers not captured in the OML based floating potential predictions. As the flow velocity increased into the range where the OML equations are valid, the numerical and theoretical floating potential showed excellent agreement. Therefore, it was concluded that pdFOAM captures the self-consistent sheath structure about a conducting body.

In summary, based on these two results, pdFOAM can be confidently used for high-fidelity physics-based studies of the effect of ionospheric aerodynamics on LEO objects.

3. Scaling of Plasma-Body Interactions

The reduction of parameters through dimensional analysis is an established approach for investigating highly dimensional, complex systems. The scaling of plasma interactions has been treated by a variety of authors [48, 90–96]. Beiser and Raab [90] applied the Buckingham Pi theorem to the Navier-Stokes and Maxwell equations to determine the hydromagnetic similarity parameters of a dielectric, conducting, viscous medium. Lacina [94] approached the same problem from a microscopic perspective, applying the Buckingham Pi theorem to the Vlasov-Maxwell system of equations which describes the motion of ions in a plasma. These works share a common limitation; they do not directly consider the disturbance caused by the interaction of the plasma with a body i.e. the aerodynamics of plasma-body interactions. Instead, they consider the self-similar response of the plasma to a disturbance e.g. the expansion of a plasma into a vacuum in the wake of a body with a thin plasma sheath [48].

The purpose of this chapter is to determine the general set of dimensionless parameters that describes the scaling of plasma-body interactions in the near-Earth environment. This will aid in developing a fundamental understanding of the underlying phenomena involved in plasma-body interaction, while reducing the number of independent variables required to characterised the behaviour of this phenomena. As such, this section is laid out as follows: Section 3.1 determines the dimensionless parameters that govern the electrostatic Vlasov-Maxwell equations and compares these parameters against those predicted by the Buckingham Pi theorem to resolve important gaps in existing scaling approaches that limit the applicability of previous methods. Section 3.2 discusses the physical implications of the identified scaling parameters. Section 3.3 presents Particle-in-Cell (PIC) simulations that demonstrate the ability of the scaling parameters to predicted the self-similarity of plasma-body interactions in the near-Earth environment.

3.1 Derivation of Scaling Laws

To address the limitation of prior plasma scaling relationships, this work considers the electrostatic interaction of a collisionless, unmagnetised multi-species plasma with multiply charged ions with a body at a fixed potential with respect to a quasi-neutral freestream plasma. The collisionless, unmagnetised assumptions are generally considered appropriate for LEO objects [38, 44, 46, 63]. Within these assumptions, the electron distribution is approximated by an isothermal, inertia-less electron fluid - also known as a Boltzmann electron fluid [44]. Freestream quantities are denoted by ∞, body quantities are denoted by B, and free quantities are denoted (0) (quantities that may be taken at points between ∞ and B).

3.1.1 Vlasov-Maxwell Equations

The phase space distribution function f of particles of species k within the volume element $dx_1dx_2dx_3$ with velocity $\mathbf{c}_k$ at time t can be defined as,

$$f_k\left(\mathbf{x},\mathbf{c}_k,t\right) \tag{3.1}$$

The evolution of f_k through time is described by the Boltzmann equation,

$$\frac{\partial f_k}{\partial t} + \mathbf{c}_k \cdot \nabla_x f_k + \frac{\mathbf{F}_\alpha}{m_k} \cdot \nabla_c f_k = \left(\frac{\partial f_k}{\partial t}\right)_{coll} \tag{3.2}$$

From left to right, the left-hand side terms of Eqn. 3.2 describe: the rate of change of f_k with time; the diffusion of f_k; and the influence of external forces $\mathbf{F}_k$ on f_k. The right-hand side describes the rate of change of f_k as a result of particle collisions. In the collisionless limit ($(\partial f/\partial t)_{coll} = 0$), Eqn. 3.2 is also known as the Vlasov equation [62].

In a plasma, $\mathbf{F}_k$ represents the Lorentz force, which describes the interaction of charge species through their mutual electric ($\mathbf{E}$) and magnetic ($\mathbf{B}$) fields [62],

$$\mathbf{F}_k = q_k\left(\mathbf{E}(\mathbf{x},t) + \mathbf{c}_k \times \mathbf{B}_k(\mathbf{x},t)\right) \tag{3.3}$$

Under the assumptions decribed at the start of this section, Maxwell's equations are greatly simplified; the description of $\mathbf{E}$ reducing to Poisson's equations for the electrostatic field potential (ϕ) [64],

$$\mathbf{E} = -\nabla\phi, \qquad \varepsilon_0\nabla^2\phi = -\rho(\mathbf{x}) \tag{3.4}$$

where the space-charge density ($\rho(\mathbf{x})$) of a plasma with K ion species is given by [64],

$$\rho(\mathbf{x}) = \left(\sum_k^K q_k n_k\right) - q_e n_e, \qquad n_k = \int f_k d\mathbf{c} \tag{3.5}$$

and n_e may be described by a Boltzmann electron fluid with reference electron number density $n_{e,(0)}$,

$$n_e = n_{e,(0)}\exp\left[\frac{q_e\phi(\mathbf{x})}{k_B T_e}\right] \tag{3.6}$$

Defining $n_{e,(0)}$ with respect to a quasi-neutral freestream, $n_{e,\infty}$ can be written as,

$$n_{e,\infty} = \frac{1}{q_e}\sum_k^K q_k n_{k,\infty} \tag{3.7}$$

Substituting Eqn. 3.5-3.7 into Eqn. 3.4, the equations governing the distribution of a K-species plasma are,

$$\frac{\partial f_k}{\partial t} + \mathbf{c}_k \cdot \nabla_x f_k - \frac{q_k}{m_k} \nabla_x \phi \cdot \nabla_c f_k = 0, \tag{3.8}$$

$$\nabla^2 \phi = -\frac{q_e}{\varepsilon_0} \sum_k^K \frac{q_k}{q_e} \left(n_k - n_{k,\infty} \exp\left[\frac{q_e \phi(\mathbf{x})}{k_B T_e} \right] \right) \tag{3.9}$$

To express Eqn. 3.8-3.9 in dimensionless form, we now introduce the following transformations:

$$\begin{aligned} \mathbf{x} &= r_{(0)} \mathbf{X}, & t &= \tau/\omega_{(0)}, & \mathbf{c}_k &= v_{k,(0)} \mathbf{u}_k \\ f_k &= n_{k,\infty} F_k, & \phi &= \phi_{(0)} \Phi, & q_k &= q_e Z_k \\ n_k &= n_{k,\infty} N_k, & \nabla_x &= \hat{\nabla}_X / r_{(0)}, & \nabla_c &= \hat{\nabla}_u / v_{k,(0)} \end{aligned} \tag{3.10}$$

Here, $r_{(0)}$, $\omega_{(0)}$ and $v_{(0)}$ represent some characteristic disturbance length, frequency and velocity respectively, the subscript (0) referring to some arbitrary reference point. $\mathbf{X}$, τ, $\mathbf{u}$, F, Φ, Z, and N_k are dimensionless parameters, and ∇_X and ∇_u are the dimensionless gradient operators in physical and velocity space.

Substituting the transformations in Eqn. 3.10 into Eqn 3.8-3.9 gives,

$$\left(\frac{\omega_{(0)} r_{(0)}}{v_{k,(0)}} \right) \frac{\partial F_k}{\partial \tau} + \mathbf{u}_k \cdot \hat{\nabla}_X F_k - Z_k \left(\frac{q_e \phi_{(0)}}{m_k v_{k,(0)}^2} \right) \hat{\nabla}_X \Phi \cdot \hat{\nabla}_u F_k = 0 \tag{3.11}$$

$$\hat{\nabla}_X^2 \Phi = \sum_k^K -Z_k \frac{r_{(0)}^2 q_e n_{k,\infty}}{\varepsilon_0 \phi_{(0)}} \left(N_k - \exp\left[\left(\frac{q_e \phi_{(0)}}{k_B T_e} \right) \Phi \right] \right) \tag{3.12}$$

The effect of ion thermal effects can be made explicit by separating $v_{k,(0)}$ into a drift ($v_{d,k,(0)}$) and thermal ($v_{t,k,(0)}$) component ($v_{k,(0)} = v_{d,k,(0)} + v_{t,k,(0)}$. The drift component represents the relative velocity between the disturbance and the freestream plasma i.e. body velocity $v_{k,B}$ (the d subscript dropped for compactness). The thermal component is taken to be described by the freestream ion thermal velocity,

$$v_{t,k,\infty} = \sqrt{\frac{2 k_B T_{k,\infty}}{m_k}} \tag{3.13}$$

Again for compactness, the ion drift ratio of the k^{th} ion species (S_k) shall be written as $S_k = v_{k,B}/v_{t,k,\infty}$. As a result, the drift and thermal effects can be separated in Eqn. 3.11 such that,

$$\begin{aligned} &\left(\frac{\omega_{(0)} r_{(0)}}{v_{k,B}} \right) \frac{\partial F_k}{\partial \tau} + \left(1 + S_k^{-1}\right) \mathbf{u}_k \cdot \hat{\nabla}_X F_k \\ &\qquad - Z_k \left(\frac{q_e \phi_{(0)}}{m_k v_{k,B}^2} \right) \left(1 + S_k^{-1}\right)^{-1} \hat{\nabla}_X \Phi \cdot \hat{\nabla}_u F_k = 0 \end{aligned} \tag{3.14}$$

From inspection, there are five dimensionless parameters that govern the behaviour of Eqn. 3.14 and 3.12. These are,

$$\begin{aligned} \alpha_k &= -Z_k \left(\frac{q_e \phi_{(0)}}{m_k v_{k,B}^2} \right), & \mu_e &= \left(\frac{q_e \phi_{(0)}}{k_B T_e} \right), \\ \xi_k &= -Z_k \left(\frac{r_{(0)}^2 n_{k,\infty} q_e}{\varepsilon_0 \phi_{(0)}} \right) & \Omega_k &= \left(\frac{\omega_{(0)} r_{(0)}}{v_{k,B}} \right) \\ S_k &= v_{k,B} / \sqrt{2 k_B T_{k,\infty}/m_k} \end{aligned} \tag{3.15}$$

Substituting the dimensionless parameters in Eqn. 3.15 into Eqn. 3.12 and Eqn. 3.14 gives,

$$\Omega_k \partial F_k/\partial\tau + \left(1+S_k^{-1}\right)\mathbf{u}_k\cdot\hat{\nabla}_X F_k + \alpha_k\left(1+S_k^{-1}\right)^{-1}\hat{\nabla}_X\Phi\cdot\hat{\nabla}_u F_k = 0 \tag{3.16}$$

$$\hat{\nabla}_X^2\Phi = \sum_k^K \xi_k\left(N_k - \exp\left[\mu_e\Phi\right]\right) \tag{3.17}$$

Hence, the $4+5K$ quantities (each ion species introducing ion properties m_k, q_k, $T_{k,\infty}$ and $n_{k,\infty}$) describing plasma-body interactions have reduced to $1+4K$ dimensionless parameters (each ion species described by its own α_k, ξ_k, S_k and Ω_k).

The relative effect of each species on Φ can be made more explicit by introducing the dimensionless parameters χ and β_k,

$$\chi = \left(\sum_k^K \xi_k\right)^{1/2}, \quad \beta_k = \frac{\xi_k}{\chi^2} \tag{3.18}$$

Eqn. 3.17 can then be re-written as,

$$\hat{\nabla}_X^2\Phi = \chi^2\left(\sum_k^K(\beta_k N_k) - \exp\left[\mu_e\Phi\right]\right) \tag{3.19}$$

The physical significance of these dimensionless parameters and the advantage of this latter form in Eqn. 3.19 are discussed in Section 3.2.

3.1.2 Buckingham Pi Analysis

Section 3.1 derived the $1+4K$ set of independent dimensionless parameters that govern the Vlasov-Maxwell system of equations that describes plasma-body interactions defined by $7+5K$ quantities (including constants) with 5 independent dimensions. According to the Buckingham Pi theorem however, a system described by n quantities with m independent dimensions can be described by $m-n$ dimensionless parameters [97] - two more parameters than indicated in Eqn. 3.15. This raises the question, *are there additional dimensionless groups not accounted for in Eqn. 3.15?* This section applies the Buckingham Pi theorem to address this question.

The general procedure of the Buckingham Pi theorem is simple: (1) select m repeating or *"independent"* quantities with independent dimensions. (2) express the remaining *"dependent"* quantities as a product of the independent quantities. (3) take the ratio of dependent and independent variables. These ratios are Pi-groups, the set of which describes the dimensionless function Θ. We refer the reader to [97] for a comprehensive discussion of the Buckingham Pi theorem and its application.

From inspection, Eqn. 3.12 and Eqn. 3.14 are described by the quantities $r_{(0)}$, $\omega_{(0)}$, $\phi_{(0)}$, $n_{k,\infty}$, T_e, T_k, $v_{k,B}$, q_k, q_e, m_k, k_B and ε_0. For simplicity we shall consider a two ion species (K=2) plasma with species x and y. Table 3.1 outlines these quantities and their dimensions. Applying the Buckingham Pi theorem, the independent quantities listed in Table 3.1 result in the following dimensionless parameters:

$$\begin{array}{lll}
\Pi_1 = n_{x,\infty}r_{(0)}^3 & \Pi_2 = n_{y,\infty}r_{(0)}^3 & \Pi_3 = m_x/m_y \\
\Pi_4 = q_x/q_e & \Pi_5 = q_y/q_e & \Pi_6 = \omega_{(0)}r_{(0)}/v_{x,B} \\
\Pi_7 = \dfrac{q_e\phi_{(0)}}{m_x v_{x,B}^2} & \Pi_8 = \dfrac{m_x v_{x,B}^2}{k_B T_e} & \Pi_9 = \dfrac{q_e^2}{r_{(0)}m_x v_{(0)}^2\varepsilon_0} \\
\Pi_{10} = T_e/T_x & \Pi_{11} = T_e/T_y & \Pi_{12} = v_{x,B}/v_{y,B}
\end{array} \tag{3.20}$$

Table 3.1: Set of independent and dependent quantities that describe plasma-body interactions.

Independent Quantities	Symbol	Dimensions
Disturbance Length	$r_{(0)}$	$[L]$
Ion Mass x	m_x	$[M]$
Electron Temperature	T_e	$[T]$
Disturbance Velocity x	$v_{x,B}$	$[L][t]^{-1}$
Electron Charge	q_e	$[A][t]$
Dependant Quantities		
Freestream Number Density x	$n_{x,\infty}$	$[L]^{-3}$
Freestream Number Density y	$n_{y,\infty}$	$[L]^{-3}$
Ion Mass y	m_y	$[M]$
Ion Charge x	q_x	$[A][t]$
Ion Charge y	q_y	$[A][t]$
Disturbance Frequency	ω	$[t]^{-1}$
Disturbance Potential	$\phi_{(0)}$	$[M][L]^2[t]^{-3}[A]^{-1}$
Boltzmann Constant	k_B	$[M][L]^2[t]^{-2}[T]^{-1}$
Permittivity of Freespace	ε_0	$M^{-1}L^{-3}[t]^4[A]^2$
Ion Temperature x	T_x	$[T]$
Ion Temperature y	T_y	$[T]$
Disturbance Velocity y	$v_{y,B}$	$[L][t]^{-1}$

Substituting Eqn 3.20 into Eqn. 3.12 and Eqn. 3.14 gives,

$$\Pi_6 \frac{\partial F_x}{\partial t} + \left(1 + (\Pi_8 \Pi_{10})^{-1/2}\right) \mathbf{u}_x \cdot \hat{\nabla}_X F_x \tag{3.21}$$

$$-\Pi_4 \Pi_7 \left(1 + (\Pi_8 \Pi_{10})^{-1/2}\right)^{-1} \hat{\nabla}_X \Phi \cdot \hat{\nabla}_u F_x = 0$$

$$\Pi_6 \Pi_{12} \frac{\partial F_y}{\partial t} + \left(1 + (\Pi_5 \Pi_8 \Pi_{11})^{-1/2}\right) \mathbf{u}_y \cdot \hat{\nabla}_X F_y \tag{3.22}$$

$$-\Pi_3 \Pi_5 \Pi_7 \left(1 + (\Pi_5 \Pi_8 \Pi_{11})^{-1/2}\right)^{-1} \hat{\nabla}_X \Phi \cdot \hat{\nabla}_u F_i = 0$$

$$\hat{\nabla}_X^2 \Phi = -\Pi_1 \Pi_4 \Pi_7^{-1} \Pi_9 \left(N_x - \exp\left[\Pi_7 \Pi_8 \Phi\right]\right) - \Pi_2 \Pi_5 \Pi_7^{-1} \Pi_9 \left(N_y - \exp\left[\Pi_7 \Pi_8 \Phi\right]\right) \tag{3.23}$$

From inspection, the relationship between the Π-groups and the dimensionless parameters is,

$$\begin{aligned}
\alpha_x &= -\Pi_3 \Pi_4 & \alpha_y &= -\Pi_3 \Pi_4 \\
\xi_x &= -\Pi_1 \Pi_4 \Pi_7^{-1} \Pi_9 & \xi_y &= -\Pi_2 \Pi_5 \Pi_7^{-1} \Pi_9 \\
S_x &= (\Pi_8 \Pi_{10})^{1/2} & S_y &= (\Pi_5 \Pi_8 \Pi_{11})^{1/2} \\
\Omega_x &= \Pi_6 & \Omega_y &= \Pi_6 \Pi_{12} \\
\mu_e &= \Pi_4 \Pi_5
\end{aligned} \tag{3.24}$$

In words, each set of Π-group that scale a particular phenomenon can be grouped as a single scaling parameter. Provided that the full set of Π-groups is represented in the set of dimensionless parameters, the Buckingham Pi theorem is satisfied. Hence, the results from the previous section are recovered; the $1+4K$ identified dimensionless parameters described by the complete set of Π-groups. As a result, the identified parameters describe *physically relevant scaling laws* for plasma interaction phenomena. Hence, we refer to them as *"scaling parameters"*.

3.2 Physical Interpretation of Scaling Parameters

The non-dimensionalisation of the K species Vlasov-Maxwell system of equations in Section 3.1 resulted in the identification of $1+4K$ independent dimensionless parameters ($2+4K$ dimensionless parameters in the χ, β_k form). A subsequent Buckingham Pi analysis of the system demonstrated that these scaling parameters constitute a complete set of Π-groups. We now consider the physical nature of these scaling parameters in plasma-body interactions based on Eqn. 3.16 and Eqn. 3.19.

3.2.1 α_k: Ion Deflection Parameter

α_k can be expressed as,

$$\alpha_k = -\frac{1}{2}\frac{2Z_k q_e \phi_{(0)}}{m_k v_{(0)}^2} = -\frac{1}{2}\frac{P.E.}{K.E.} \tag{3.25}$$

Physically, α_k is the ratio of disturbance potential energy (P.E.) to kinetic energy (K.E). The role of α_k in Eqn. 3.16 is to scale the deflection of ions by electrical disturbances i.e. $\nabla\Phi$. The relative sign between Z_k and $\phi_{(0)}$ controls the direction of ion deflection. For example, positive ions will be deflected toward a negative disturbance ($\phi_{(0)} < 0$), following the potential gradient $\nabla\Phi$. Conversely, negative ions will be deflected away from positive disturbances, impeded by $-\nabla\Phi$.

The magnitude of the ion deflections is related to $|\alpha_k|$. As $|\alpha_k| \to 0$, the ion kinetic energy dominates the motion of the ions, decoupling their motion from the electric field. In the converse limit, when $|\alpha_k| \to \infty$, the motion of the ions becomes dominated by the disturbance potential energy. In essence, α_k describes the deflection of ions by field effects, and hence, it is called here the *"ion deflection parameter"*. Examples of α_k can be found appearing in orbital motion theory, for example, the Orbital Motion (OM) critical impact parameter b_* that describes the ion absorption barrier used in probe theory and dusty plasma physics [36, 88, 89],

$$b_*/r_B = \left(1 - \frac{2q_e\phi_B}{m_i v_B^2}\right)^{1/2} = (1+2\alpha)^{1/2} \tag{3.26}$$

3.2.2 S_k: Ion Thermal Ratio

By splitting $v_{k,(0)}$ into a drift and thermal component, the effect of ion thermal energy on Eqn. 3.16 becomes explicit. For the mesothermal case, such as that in LEO (where $v_{t,k,\infty} \gg v_{k,B} \gg v_{t,e}$), $S_k \gg 1$ and the evolution of F_k is decoupled from ion thermal effects. In the converse limit ($S_i \ll 1$), the diffusion term in Eqn. 3.16 is enhanced by the ion temperature i.e. thermal diffusion. At the same time, a large S_i suppresses the deflection of ions by field effects i.e. increased ion thermal energy increases the resistance of ions to field effects. As with $v_{k,B}$, if $S_k \to 0$ (thermal velocity dominates over drift velocity) and $m_k v_{t,k,\infty} \gg q_e\phi_{(0)}$, then ion motion is decoupled from field effects and the system becomes thermally dominated.

In a LEO context, thermally dominated interactions are unlikely, however transition thermal effects may be present as $S_k \to 1$. Based on the above discussion, transition thermal effects will tend to diffuse plasma phenomena. This is consistent with prior observations and predictions of ion thermal effects [47, 98, 99].

3.2.3 χ: General Shielding Ratio

A commonly referenced scaling parameter is the shielding ratio $r_B/\lambda_{D,e}$. Considering a high-temperature (weakly-coupled), single species plasma with cold ions, χ becomes,

$$\chi = r_{(0)} \left(\frac{Z_i n_{i,\infty} q_e^2}{\varepsilon_0 k_B T_e} \right)^{1/2} = \left(\frac{r_{(0)}}{\lambda_{D,e}} \right) \tag{3.27}$$

The role of $r_B/\lambda_{D,e}$ as a shielding parameter can be seen in Eqn. 3.17. As the body size becomes large compared to $\lambda_{D,e}$, $\nabla^2\Phi \to \infty$ and the distance that electrical disturbances travel approaches 0 i.e. the electric fields of space-charge disturbances are strongly shielded. In the converse limit, as $r_B/\lambda_{D,e} \to 0$, $\nabla^2\Phi \to 0$ and the disturbance is described by Laplace's equation i.e. electrical disturbances move toward infinity. However, Eqn. 3.27 is only valid for systems where $q_e\phi_{(0)} \ll k_B T_e$ and $T_i \ll T_e$.

Here, we introduce the new length parameter λ_ϕ,

$$\lambda_\phi = \left(-\frac{\varepsilon_0 \phi_{(0)}}{q_e \sum_k^K Z_k n_{k,\infty}} \right)^{1/2} \tag{3.28}$$

Interpreted the same way as $\lambda_{D,e}$, λ_ϕ is the distance required to electrically shield the disturbance $\phi_{(0)}$ in a k species plasma i.e. λ_ϕ describes a general plasma sheath thickness. Letting the potential energy of the disturbance equal the thermal energy of the freestream plasma $\phi_\infty = k_B \left(T_e + \sum_k^K Z_k^{-1} T_k \right) / q_e$, the general shielding length λ_ϕ becomes

$$\lambda_{\phi,\infty} = \left(\frac{\varepsilon_0 k_B / q_e^2}{n_e/T_e + \sum_k^K Z_k^2 n_k / T_k} \right)^{1/2} = \lambda_D \tag{3.29}$$

where the quasi-neutral identity $q_e n_e = \sum_k^K q_k n_k$ has been applied.

Hence the general Debye length λ_D has been recovered in the high-temperature (weakly-coupled) limit. As another example, Benilov [100] applied the Child-Langmuir law to predict the sheath thickness (d_{sh}) about a high-voltage cathode as,

$$d_{sh} = (2^{5/4}/3)\sqrt{\varepsilon_0 \phi_B / q_i n_i} = (2^{5/4}/3)\lambda_\phi \tag{3.30}$$

In words, space-charged limited sheaths are described by λ_ϕ.

In effect, χ (or more precisely λ_ϕ) provides a link between low and high-voltage plasma phenomena. Following from this, χ may now be written in a similar form as the shielding ratio $r_{(0)}/\lambda_{D,e}$,

$$\chi = r_{(0)}/\lambda_\phi \tag{3.31}$$

Where we refer to χ as the *"general shielding ratio"* and λ_ϕ as the *"general shielding length"*. The physical interpretation of λ_ϕ being the distance required to electrically screen the space-charge disturbance $\phi_{(0)}$. This disturbance may be caused by an immersed body or by a localised space-charge discontinuity.

3.2.4 β_k: Ion Coupling Parameter

While β_k is a function of ξ_k, Eqn. 3.19 provides a clearer physical interpretation of multi-species plasma interactions. β_k can be re-written as,

$$\beta_k = \left(\frac{Z_k n_{k,\infty}}{\sum_k^K Z_k n_{k,\infty}} \right) \tag{3.32}$$

Hence, β_k describes the relative contribution of ion species k to electrical disturbances through its contribution to the total ion space-charge density. As $\beta_k \to 0$, the contribution of k goes to zero and Φ is governed by the remaining species. In essence, β_k describes the relative coupling of ions species k with electrical disturbances and, hence, we call it the *"ion coupling parameter"*.

3.2.5 μ_e: Electron Energy Coefficient

μ_e is a common non-dimensionalisation of potential, being a relatively easily measurable quantity [34, 38, 44, 91]. It is the ratio of disturbance potential energy to electron thermal energy and physically describes the depth of penetration of an average electron into potential barriers [91]. Based on Eqn. 3.19, the role of μ_e is to dampen or enhance the ability of the electron distribution to respond to electrical disturbances caused by the ion distribution). The disturbance caused by a localised abundance of ions ($\phi_{(0)} > 0$) attracts electrons and causes an increase in N_e scaled by μ_e as described by the dimensionless Boltzmann electron fluid,

$$N_e = \exp\left[\mu_e \Phi\right] \tag{3.33}$$

The converse is also true, a localised depletion of ions ($\phi_{(0)} < 0$) dampens the ability of electrons to populate this area. The degree of enhancement or damping is then described by the relative energy of the electrons compared to the disturbance energy. In essence, μ_e describes the relative energy between a disturbance and the Boltzmann electron fluid, and we refer to it as the *"electron energy coefficient"*.

3.2.6 Ω_k: Ion Temporal Parameter

Ω_k describes the transit time of a disturbance relative to its frequency $\omega_{(0)}$. The effect of Ω is to scale any temporal fluctuations in F_k. It implies that if temporal effects are to be scaled, then the scaling of any frequency effects must preserve the transit time of an ion across the disturbance [38]. Conversely, in the steady-state limit, Ω_k can be neglected. Stone [38] also identified this parameter and referred to it as the ion *"temporal parameter"* Ω, hence we follow this nomenclature.

3.3 Self-Similar Transformations of Plasma-Body Interactions

A consequence of the Buckingham Pi theorem is that two systems will be identical in dimensionless space if the product of dimensioned quantities within the Π-groups caused the two systems to have an identical and complete set of Π-groups values. This is known as *"self-similarity"*, where two systems with different system quantities experience an identical interaction because of phenomena in each system, described by the scaling parameters, are identical[97]. The purpose of this section is to develop confidence in the identified scaling parameters as a means to organise and scale plasma-body interactions by demonstrating the ability of the scaling parameters to predict self-similar flow transformations.

Four self-similarity transformations are demonstrated: three single species transformations matching dissimilar ion species, body size, and body potential respectively; and a multi-species transformation matching the interaction of plasma mixtures with dissimilar ion charges. The general approach in each transformation is to consider a two reference interactions R_1 and R_2 that differ in some aspect e.g. ion species. The self-similarity transformation required to make the R_2 match R_1 is then denoted as $S_{2\to1}$.

3.3.1 Transformation 1: Ion Mass

Considering two identical single species plasma-body interactions with ion mass $m_{(R_1)}$ and $m_{(R_2)}$ where $m_{(R1)} \neq m_{(R_2)}$. The self-similarity of different ion species requires the scaling of only α_k, the remaining scaling parameters being independent of m_k (except for S_k as will be discussed in Section 3.3.3). One application of this scaling transformation is in experimental facilities. An available experimental parameter is the flow velocity v_B. By scaling $v_{B,(R_2)}$, the ion deflection parameters $\alpha_{(R_1)}$ and $\alpha_{(S_{2\to1})}$ are similar when,

$$v_{B,(S_{2\to1})} = \left(m_{(R_1)}/m_{(R_2)}\right)^{1/2} v_{B,(R_1)} \tag{3.34}$$

Figure 3.1 (top) compares the flow of an O^+ (Case 1) and H^+ (Case 2) plasma over a 0.3 m cylinder with a surface potential of -50 V compared to the freestream plasma Table 3.2 lists the full set of interactions conditions for Cases 1-3. The general features of mesothermal plasma-body interactions are reproduced. In the frame of the body, the expansion of the plasma into the ion void caused by the body causes a rarefaction wave (ion gradient) that moves outward perpendicular to the flow at the ion acoustic wave speed. In the frame of the body this appears as a Mach wave defined by the angle θ_r,

$$\theta_r = \sin\left(M_k^{-1}\right) \tag{3.35}$$

Based on conditions listed in Table 3.2, the ion acoustic Mach number in the O^+ flow (Case 1) is 4.61, and 1.16 in the H^+ flow (Case 2) $\gamma_k = 3$ in a collisionless plasma). From Eqn. 3.35, θ_r should be 14.3^o and 80^o for Cases 1 and 2. These compare well with the indicate rarefaction wave angle measures in Figure 3.1; Case 1 having a rarefaction wave angle of $16.1^o \pm 1^o$, and $74.3^o \pm 10^o$ in Case 2. The larger uncertainty in Case 2 is a reflection of transition ion thermal effects ($S_k = 1.48$) diffusing the wave edge and increasing simulation noise. Also evident in Figure 3.1 is the presence of a) bounded and b) unbounded ion jets predicted by orbital motion theory[36, 88, 89]; the reduction in incident kinetic energy in the H^+ (Case 2) compared to the O^+ (Case 1) flow increasing the proportion of ions captured by the body's potential well (sheath).

Figure 3.1 (bottom) compares the scaled flow $S_{2\to1}$ (Case 3) against the reference flow R_1 (Case 1). Excellent qualitative agreement is shown between Case 1 and 3: the sheath compression, wake elongation, rarefaction wave angle and collection of unbounded and bounded ion jets of the O^+ case all reproduced by the H^+ case. Hence, by balancing the ratio of body potential energy and incident ion kinetic energy, the flow physics R_1 is preserved in $S_{2\to1}$, supporting the concept of α_k describing the deflection of ions by field effects.

Table 3.2: Interaction parameters for self-similar scaling of ion mass example. Bold numbers highlight the effect of scaled parameters on dimensionless parameters.

Case	$\phi_{(B)}$ (V)	$r_{(B)}$ (m)	$v_{(B)}$ (km/s)	m $(10^{-27}kg)$	n_∞ $(10^{10}m^{-3})$	T_e (K)
1 (R_1)	-50	0.3	7.5	26.55	4	1997
2 (R_2)	-50	0.3	7.5	**1.67**	4	1997
3 ($S_{2\to1}$)	-50	0.3	**29.9**	**1.67**	4	1997
	α_k		χ		μ_e	
1 (R_1)	5.364		1.1414		-290.5	
2 (R_2)	**85.2785**		1.1414		-290.5	
3 ($S_{2\to1}$)	**5.364**		1.1414		-290.5	

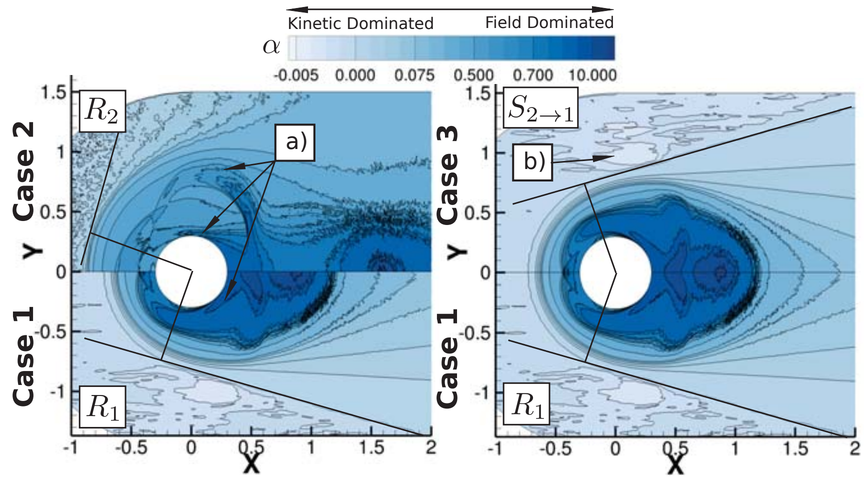

Figure 3.1: Self-similar transformation of O^+ (R_1) and H^+ flows (R_2). Rarefaction angle are overlaid to aid comparison. a) bounded ion jets. b) unbounded ion jets

3.3.2 Transformation 2: Body Scale

A typical application of dimensional analysis is the study of scaled models in small test facilities. This may be achieved in plasma-body interactions by scaling the general shielding ratio χ.

Consider for example two identical plasma flows about a body $r_{B,(R_1)}$ and $r_{B,(R_2)}$ where $r_{B,(R_1)} \neq r_{B,(R_2)}$. By scaling $n_{(R_1)}$ to $n_{\infty,(S_{2\to1})}$, the physics scaled by the general shielding ratio χ will be preserved when,

$$n_{\infty,(S_{2\to1})} = \left(\frac{r_{B,(R_1)}}{r_{B,(R_2)}}\right)^2 n_{\infty,(R_1)} \tag{3.36}$$

Note that $T_{e,(R_2)}$ or $\phi_{B,(R_2)}$ could also have been scaled in this interaction. The drawback of these variables is that T_e scales both χ and μ_e, while $\phi_{(0)}$ scales χ, α and μ_e; the latter is demonstrated in Section 3.3.3.

Figure 3.2 (top) compares the interaction of an O^+ plasma with two cylinders with radii 0.3 m (Case 4) and 0.03 m (Case 5) at $-25V$. Table 3.3 lists the full set of interactions conditions for Cases 4-6. Again the general features of mesothermal plasma body interactions have been reproduced. As predicted, r_B has no effect on the rarefaction angle, the measured rarefaction angle in Case 4 and Case 5 being $13.4^o \pm 2^o$ and 14.5 ± 2^o respectively. Again, this compares well with a predicted θ_r of 14.3.

As discussed in Section 3.2, the commonly used shielding ratio $r_B/\lambda_{D,e}$ does not accurately predict sheath thickness near high-voltage objects (fundamentally limited by $q_e\phi_B \ll k_B T_e$ and $T_e > T_i$ assumptions). The electron Debye length in Case 4 and 5 is 1.54 cm compared to a predicted general shielding length of 18.58 cm. Comparing this with Figure 3.2 (top) and taking the sheath edge where $\alpha = 0.1$, the sheath thickness in Case 4 and Case 5 is 19.5 ± 1 cm and 18 ± 1 cm, agreeing well with λ_ϕ. The definition of sheath edge varies across a variety of works [39, 54, 101]. A comprehensive study of an appropriate definition of sheath edge is outside the scope of this work. Irrespective of the definition of sheath edge, Figure 3.2 illustrates that λ_ϕ provides a superior approximation of sheath thickness than $\lambda_{D,e}$.

Table 3.3: Interaction parameters for self-similar scaling of body scale example. Bold numbers highlight the effect of scaled parameters on dimensionless parameters. Ion thermal effects are not scaled.

Case	$\phi_{(B)}$ (V)	$r_{(B)}$ (m)	$v_{(B)}$ (km/s)	m $(10^{-27}kg)$	n_∞ $(10^{10}m^{-3})$	T_e (K)
4 (R_1)	-25	0.3	7.5	26.55	4	1997
5 (R_2)	-25	**0.03**	7.5	26.55	4	1997
6 ($S_{2\to1}$)	-25	**0.03**	7.5	26.55	**400**	1997
	α_k		χ		μ_e	
4 (R_1)	2.682		1.6142		-145.27	
5 (R_2)	2.682		**0.1614**		-145.27	
6 ($S_{2\to1}$)	2.682		**1.6142**		-145.27	

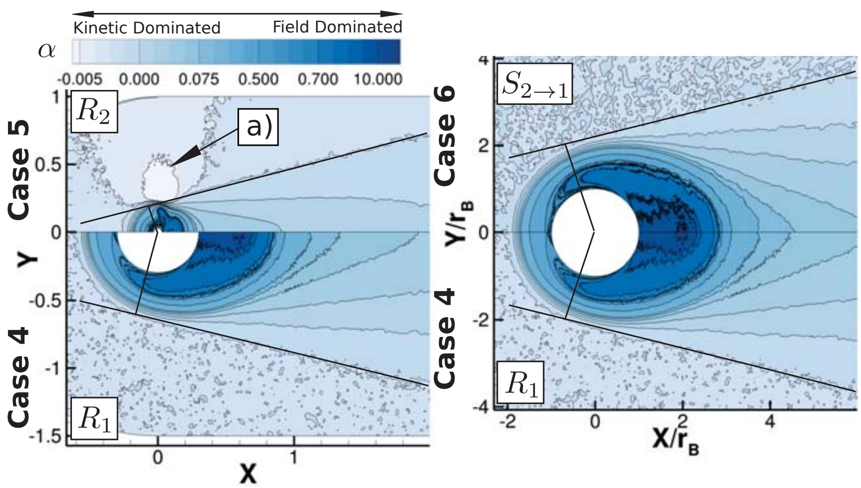

Figure 3.2: Self-similar transformation of 0.3 m radius cylinder (R_1) and 0.03 m radius cylinder (R_2). Rarefaction angle measures are overlaid to aid comparison of fields. a) unbounded ion jets

Figure 3.2 (bottom) further supports our assertion that λ_ϕ describes the shielding of an object at an arbitrary surface potential, showing the reference flow R_1 (Case 4) compared against the scaled flow $S_{2\to1}$ (Case 6) (with a 10^2 increase ion number density) in dimensionless space r_B/λ_ϕ. Figure 3.2 demonstrates the scaling of sheath structure in dimensionless space, the increase in number density causing a reduction in sheath thickness in Case 6 to match Case 4. Overall, χ has been demonstrated to successfully predict self-similar transformations.

It is worth noting that the number density transformation is implied by both λ_ϕ and λ_D. To demonstrate that λ_ϕ is correct requires a scaling transformation of λ_ϕ not implied by λ_D e.g. the body potential ϕ_B.

3.3.3 Transformation 3: Body Potential

A key limitation of previous scaling parameters is their limitation to low voltage objects, whether explicit or implicitly through the use of λ_D. This section demonstrates the ability of the scaling parameters to predict the self-similar scaling transformation of two high-voltage objects, R_1 and R_2. To preserve the flow physics of the R_1 requires scaling of α_k, χ and μ_e. This can be achieved, for example, by scaling v_B, $n_{i,\infty}$ and T_e such that,

$$\begin{aligned} v_{B,(S_{2\to1})} &= \left(\phi_{B,(R_2)}/\phi_{B,(R_1)}\right)^{1/2} v_{B,(R_1)} \\ n_{\infty,(S_{2\to1})} &= (\phi_{B,(R_2)}/\phi_{B,(R_1)}) n_{\infty,(R_1)} \\ T_{e,(S_{2\to1})} &= (\phi_{B,(R_2)}/\phi_{B,(R_1)}) T_{e,(R_1)} \end{aligned} \tag{3.37}$$

The scaling parameters are limited to geometrically similar objects. This section considers the scaling of a thin flat plate to demonstrate that this is the case. Figure 3.3 (top) compares the interaction of a thin 0.3 m wide flat plate at -25 V (Case 7) and -10 V (Case 8). Table 3.4 lists the full set of interactions conditions for Cases 7-9. Unlike the previous similarity two examples, it is difficult to decouple the physical influence of α_k, χ and μ_e on flow phenomena between Case 7 and 8. The net effect of increasingly negative ϕ_B from Case 8 to Case 7 appears as an expansion of the sheath and the field dominated region in the wake. This is consistent with above observations of α_k and χ. An important point to note is the similar rarefaction wave angle, θ_r being independent of ϕ_B.

Figure 3.3 (bottom) compares the interaction of the reference flow R_1 (Case 7) with the scaled flow $S_{2\to1}$ (Case 9). The flow velocity, ion number density and electron temperature all reduced to match in Case 9 to match α_k, χ and μ_e in Case 7. Figure 3.3 (bottom) demonstrates that the scaling parameters, again, correctly predict the self-similar scaling transformations. Note however that while the majority of the structures in Case 7 are reproduced in Case 9, there exists a region of disagreement in the wake region a). This error corresponds to a region where there are relatively few simulated particles. While it is tempting to attribute this error to statistical fluctuations, another explanation is a disagreement between the relative influence ion thermal effects.

The transformation of α_k caused a reduction in velocity from 7.5 km/s to 4.73 km/s, S_i reducing from 5.9 to 3.74. In other words, the contribution of thermal effects to ion deflections almost doubles between Case 9 and Case 7. The final similarity transformation demonstrates that this region of dissimilarity is caused by ion thermal effects.

Table 3.4: Interaction parameters for self-similar scaling of body scale example. Bold numbers highlight the effect of scaled parameters on dimensionless parameters. Ion thermal effects are not scaled.

Case	$\phi_{(B)}$ (V)	$r_{(B)}$ (m)	$v_{(B)}$ (km/s)	m $(10^{-27}kg)$	n_∞ $(10^{10}m^{-3})$	T_e (K)
7 (R_1)	-25	0.3	7.5	26.55	4	1997
8 (R_2)	**-10**	0.3	7.5	26.55	4	1997
9 ($S_{2\to1}$)	**-10**	0.3	**4.73**	26.55	**1.6**	**798.8**

Case	α_k	χ	μ_e
7 (R_1)	2.682	1.6142	-145.27
8 (R_2)	**1.0728**	**2.5524**	**-58.1097**
9 ($S_{2\to1}$)	**2.6973**	**1.6142**	**-145.27**

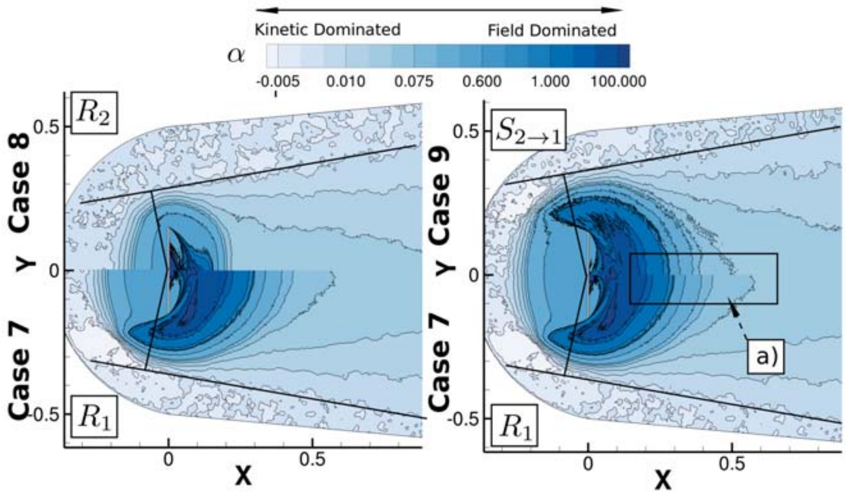

Figure 3.3: Self-similar transformation of -25 V cylinder (R_1) and -10 V cylinder (R_2). Rarefaction angle measures are overlaid to aid comparison of fields. a) Region of dissimilarity.

3.3.4 Transformation 4: Multi-Species Ion Charge

Past work has focused on the scaling of singly charged ions in a single ion species plasma. The scaling parameters presented in this work suggest that there exist transformations such that the interaction of multi-species plasmas with dissimilar ion charges can be made similar. This section demonstrates that this is the case.

Consider a plasma composed of a heavy ion species x and a light ion species y, where $Z_{y,(R_2)}$ is the test variable. R_1 and R_2 are similar when,

$$\begin{aligned}
n_{x,\infty,(S_{2\to1})} &= (Z_{y,(R_2)}/Z_{x,(R_1)})n_{x,\infty,(R_1)} \\
\phi_{B,(S_{2\to1})} &= (Z_{y,(R_2)}/Z_{x,(R_1)})\phi_{B,(R_1)} \\
m_{y,(S_{2\to1})} &= (Z_{y,(R_2)}/Z_{x,(R_1)})m_{y,(R_1)} \\
T_{e,(S_{2\to1})} &= (\phi_{B,(S_{2\to1})}/\phi_{B,(R_1)})T_{e,(R_1)} \\
v_{y,\infty,(S_{2\to1})} &= \left(\phi_{B,(S_{2\to1})}/\phi_{B,(R_1)}\right)^{1/2} v_{y,\infty,(S_{2\to1})} \\
v_{x,\infty,(S_{2\to1})} &= \left(\phi_{B,(S_{2\to1})}/\phi_{B,(R_1)}\right)^{1/2} v_{x,\infty,(S_{2\to1})}
\end{aligned} \tag{3.38}$$

The first three transformations capture the scaling required by $Z_{y,(R_2)}$, while the second three correct for the secondary scaling of phenomena caused by scaling of $\phi_{B,(S_{2\to1})}$. As discussed in Section 3.2.2 however, the scaling of $v_{k,B}$ or m_k will effect S_k, scaling ion thermal effects. Provided that the system is mesothermal, the system phenomena should be insensitive to ion thermal effects. *Care must be taken when scaling mesothermal phenomena however as ion thermal effects may become significant as a consequence of reduced mass or velocity.* To account for ion thermal effects in the above multi-species example would require the additional transformations,

$$\begin{aligned}
T_{x,(S_{2\to1})} &= \left(v_{x,\infty,(S_{2\to1})}/v_{x,\infty,(R_1)}\right)^2 T_{x,(R_1)} \\
T_{y,(S_{2\to1})} &= \left(\frac{m_{y,(S_{2\to1})}}{m_{y,(R_1)}}\right)\left(\frac{v_{y,\infty,(S_{2\to1})}}{v_{y,\infty,(R_1)}}\right)^2 T_{y,(R_1)}
\end{aligned} \tag{3.39}$$

Figure 3.4 (top) compares the relative contribution of species x and y in an $O^+ - H^+$ plasma (Case 10) and $O^+ - H^{++}$ (Case 11) interacting with a -25 V 0.3 m radius cylinder ($O^+ = x$,

Table 3.5: Two species self-similarity example with dissimilar ion charges and including ion thermal effects. Bold numbers highlight the effect of scaled parameters on dimensionless parameters.

Case #	10		11		12		13	
	$(R_1)_x$	$(R_1)_y$	$(R_2)_x$	$(R_2)_y$	$(S_{2\to1})_x$	$(S_{2\to1})_y$	$(S_{2\to1})_x$	$(S_{2\to1})_y$
$\phi_{(B)}$ (V)	-25	-25	-25	-25	**-50**	**-50**	**-50**	**-50**
$r_{(B)}$ (m)	0.3	0.3	0.3	0.3	0.3	0.3	0.3	0.3
$v_{(B)}$ (km/s)	7.5	7.5	7.5	7.5	**10.6**	**10.6**	**10.6**	**10.6**
m $(10^{-27}kg)$	26.55	1.67	26.55	1.67	26.55	**3.34**	26.55	**3.34**
Z_x	1	1	1	**2**	1	**2**	1	**2**
n_∞ $(10^{10}m^{-3})$	4	4	4	4	**8**	4	**8**	4
T_e (K)	1997	1997	1997	1997	**3994**	**3994**	**3994**	**3994**
T_i (K)	1537	1537	1537	1537	1537	1537	**3074**	**6124**
α	2.682	42.63	2.682	**85.2785**	**2.6854**	**42.6924**	**2.6854**	**42.6924**
χ	2.2828	2.2828	**2.7959**	**2.7959**	**2.2828**	**2.2828**	**2.2828**	**2.2828**
β	0.5	0.5	**0.33**	**0.66**	**0.5**	**0.5**	**0.5**	**0.5**
μ_e	-145.5	-145.5	-145.5	-145.5	**-145.5**	**-145.5**	**-145.5**	**-172.5**
S_k	5.932	1.488	5.932	1.488	**8.385**	**2.974**	**5.932**	**1.488**

$H^+ = H^{++} = y$. Table 3.5 lists the full set of interactions conditions for Cases 10-13. Figure 3.4 (top) illustrates how, by doubling its charge, the y ion species dominates the rarefaction wave, causing the rarefaction angle to increase. Other flow features in Cases 10 and 11 include a light species dominated wake-core and heavy species dominated sheath structure. These features appear a reflection of ion mobility.

Figure 3.4 (middle) compares the reference case R_1 (Case 10) against the scaled case $S_{2\to1}$ without accounting for ion thermal effects (Case 12). While a majority of flow features have been matched, dissimilarities in wake structure similar to those observed in Figure 3.3 can be seen at both a) and b). Further, the rarefaction wave angle of Case 12 is suppressed (smaller) compared to the reference case (Case 10); the rarefaction wave angle in Case 10 is super-imposed on Case 12 as a dotted line to illustrate this point.

Figure 3.4 (bottom) demonstrates that ion thermal effects cause these discrepancies. By scaling ion thermal effects, Figure 3.4 (bottom) confirms that observed regions of dissimilarity in Figure 3.4 (middle) (and Figure 3.3 (bottom)) are caused unscaled ion thermal effects. Figure 3.4 demonstrates the ability of the identified scaling parameters to preserve the flow physics of multi-species plasma-body interactions near high-voltage objects.

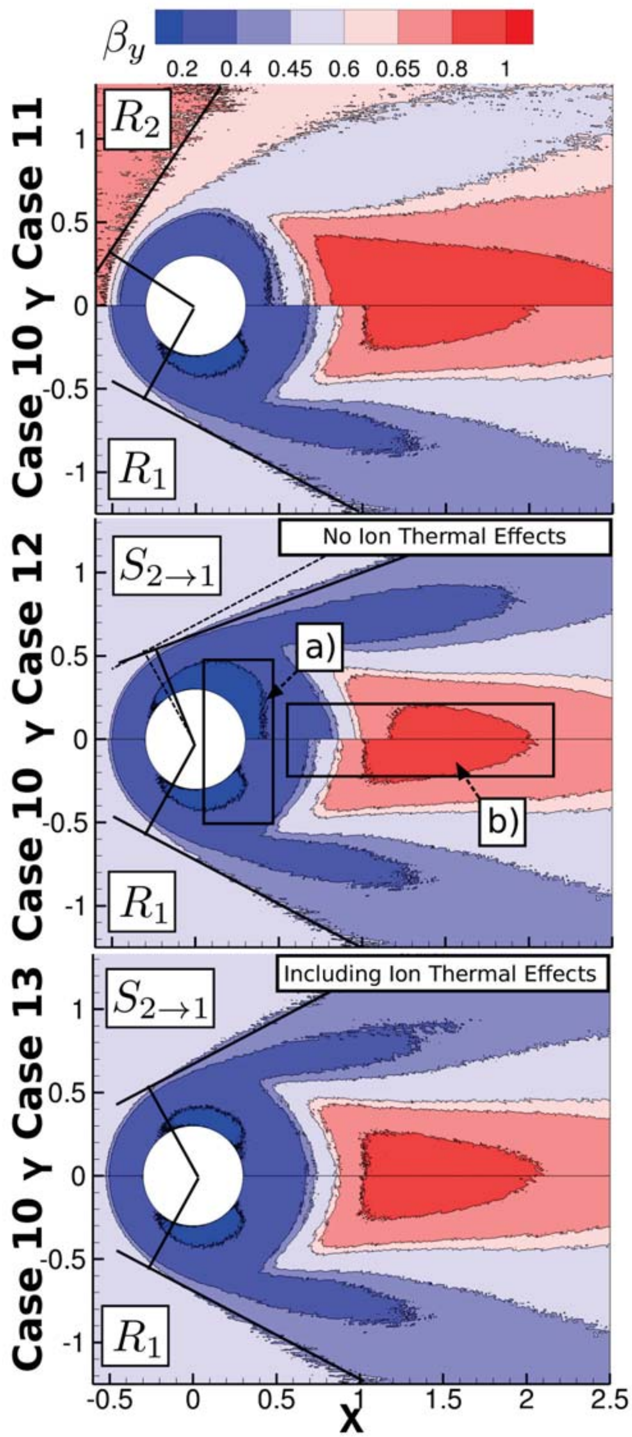

Figure 3.4: Self-similar transformation of a multi-species plasma with dis-similar ion charges interacting with a -25 V cylinder. Contours are of β_y, blue regions dominated by x, red regions by y. Full flow conditions are listed in Table 3.5. Rarefaction angle measures are overlaid to aid comparison of fields. Labeled features include: a) x dissimilarity, b) y dissimilarity.

3.4 Summary

The complex, non-linear relationship between interaction quantities and plasma-body interaction phenomena was identified as a key challenge to the study of ionospheric aerodynamics at the end of the previous chapter. To address this challenge, the set of dimensionless parameters that scale plasma-body interactions were derived here.

Based on the unmagnetised Vlasov-Maxwell equations and validated against the Buckingham Pi theorem, the $7+5K$ quantities (including constants) that define K species plasma-body interactions (including constants) were expressed as $1+4K$ independent dimensionless parameters (or $2+4K$ dimensionless parameters in the χ, β_k form). The reason for expressing ξ_k as χ and β_k became clear when considering a disturbance with potential energy equal to the surrounding thermal energy of the plasma. Introducing the new general shielding length scale λ_ϕ, Section 3.2.3 demonstrated that the general shielding length λ_ϕ becomes the general Debye length λ_D in the limit that the potential energy of the disturbance is on the order of the thermal energy of the surrounding plasma (and becomes the electron Debye length with an additional cold ion restriction). In essence, the general shielding length λ_ϕ provides a consistent link between the shielding of low and high-voltage plasma phenomena.

The validity of the scaling parameters was demonstrated in Section 3.3 by successfully predicting the self-similar transformations required to preserve the flow physics between two plasma-body interactions with dis-similar flow and body quantities. While this sort of analysis is typical in fluid mechanics, to date this is the first demonstration of self-similarity transformations of plasma-body interactions using a PIC code. Furthermore the final multi-species similarity transformation is the first demonstration of self-similarity between two multi-species plasmas with dis-similarly charged ions including ion thermal effects in a mesothermal plasma. The above scaling parameters represent a powerful tool for studying both plasma phenomena and the phenomena resulting from plasma-body interactions, ionospheric aerodynamics being a subset of plasma phenomena described within the phase-space described by the scaling parameters.

Summary of Scaling Parameters

$$
\begin{aligned}
&\text{Ion Deflection Parameter} && \alpha_k &&= -Z_k\left(\frac{q_e\phi_{(0)}}{m_k v_{k,B}^2}\right),\\
&\text{Electron Energy Coefficient} && \mu_e &&= \left(\frac{q_e\phi_{(0)}}{k_B T_{e,\infty}}\right),\\
&\text{General Body Shielding Ratio} && \chi &&= \frac{r_{(0)}}{\lambda_\phi},\\
&\text{Ion Temporal Parameter} && \Omega_k &&= \left(\frac{\omega_{(0)} r_{(0)}}{v_{k,B}}\right),\\
&\text{Ion Thermal Ratio} && S_k &&= \frac{v_{k,B}}{\sqrt{2k_B T_{k,\infty}/m_k}},\\
&\text{Ion Coupling Parameter} && \beta_k &&= \left(\frac{Z_k n_{k,\infty}}{\sum_k^K Z_k n_{k,\infty}}\right)
\end{aligned}
\tag{3.40}
$$

$$
\text{General Shielding Length} \quad \lambda_\phi = \left(-\frac{\varepsilon_0\phi_{(0)}}{q_e\sum_k^K Z_k n_{k,\infty}}\right)^{1/2} \quad [m] \tag{3.41}
$$

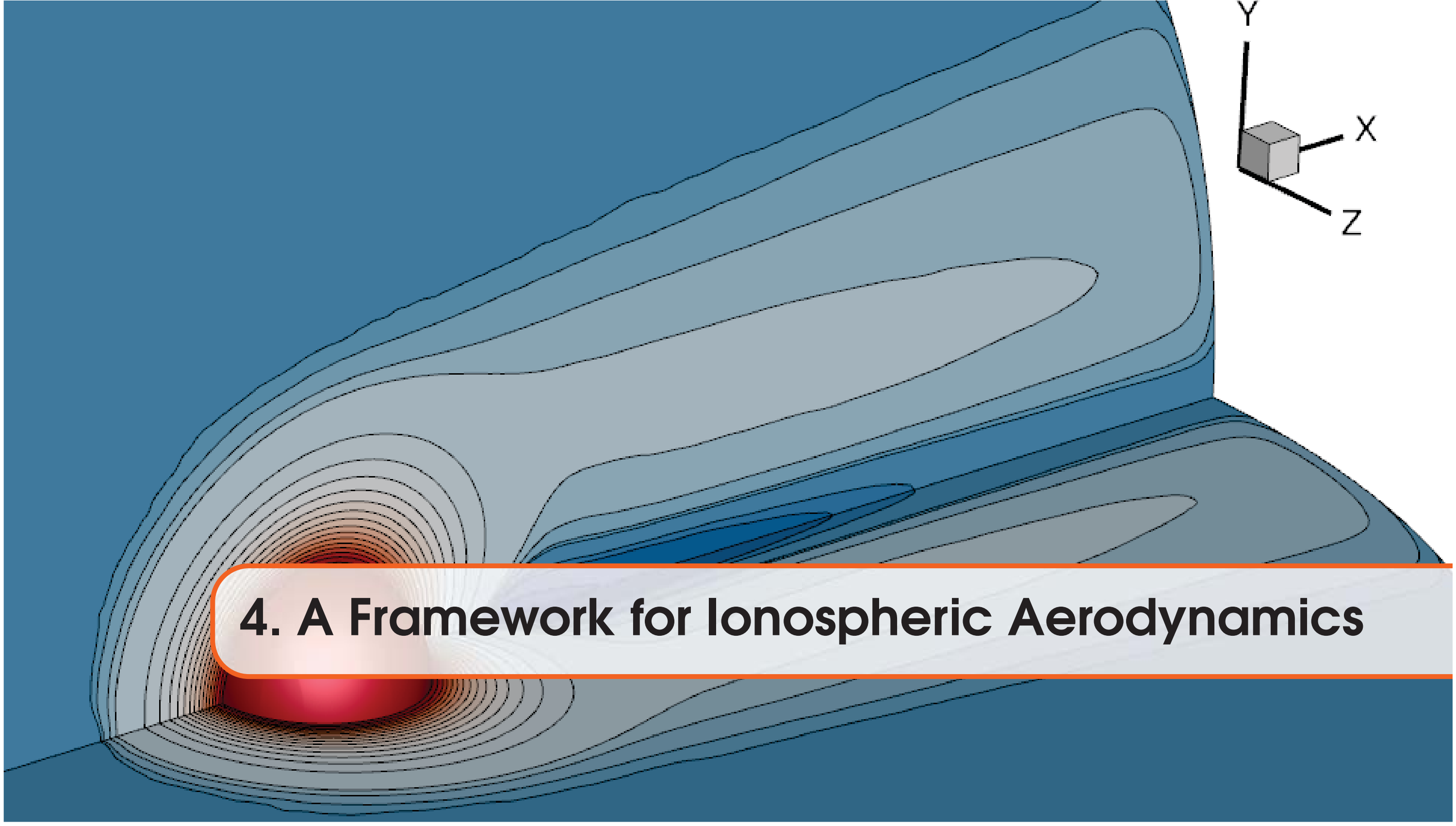

4. A Framework for Ionospheric Aerodynamics

The purpose of this chapter is to map out the relationship between the flow physics, charged aerodynamic forces and points within a dimensionless phase-space $\mathscr{P}(\alpha_k, \chi)$ to develop a framework within which to understand and quantify the influence of ionospheric aerodynamics on near-Earth objects. To this end, this section is laid out as follows: Section 4.1 determines develops a control surface methodology for capturing the momentum exchange in mesothermal plasma-body interactions that occurs in the near-Earth environment. Section 4.2 explores the links between plasma interaction phenomena, charged drag forces and the plasma scaling parameters α and χ. Section 4.3 then takes these observations and constructs a response surface described by α and χ capable of predicting an approximate charged drag coefficient $C_{D,C}$ for a uniformly charged cylindrical body.

4.1 Momentum Balance in a Flowing Plasma

To determine the influence of the plasma interaction phenomena on ionospheric aerodynamic forces, here we shall consider the general momentum balance of a mesothermal plasma-body interaction by applying the approach taken in Allen [102] and including the more general derivation of the Maxwell stress tensor by Miller, Vandome, and John [103]. For completeness, we shall allow for magnetic fields and time-varying phenomena, later these will be neglected under assumptions appropriate for ionospheric aerodynamic applications.

In a mesothermal flow, the ion thermal pressure p_i is assumed to be negligible compared to the streaming energy, and *vice a visa* for the electrons. Under these assumptions, the ion (i) and electron (e) momentum equations may be written as,

$$n_i m_i \left[\frac{\partial \mathbf{v}}{\partial t} + (\mathbf{v}\cdot\nabla)\,\mathbf{v}\right] = q_i n_i\,(\mathbf{E} + \mathbf{v}\times\mathbf{B}) \tag{4.1}$$

$$n_e m_e \left[\frac{\partial \mathbf{v}}{\partial t}\right] + \nabla p_e = -q_e n_e\,(\mathbf{E} + \mathbf{v}\times\mathbf{B}) \tag{4.2}$$

where p_e is the thermal electron pressure, $q_i(e)$ is ion (electron) charge, $\mathbf{E}$ the electric field vector, $\mathbf{B}$ the magnetic field vector, $\mathbf{v}$ the flow velocity vector and $n_{i(e)}$ the ion (electron) number density.

Adding these equations together and introducing the total charge density ρ_c ($\rho_c = (\sum_k^K Z_k q_e n_k) - q_e n_e$) and current density $\mathbf{J}$ ($\mathbf{J} = \rho_c \mathbf{v}$) gives,

$$(m_i n_i + m_e n_e) \frac{\partial \mathbf{v}}{\partial t} + m_i n_i (\mathbf{v} \cdot \nabla) \mathbf{v} + \nabla p_e = \rho_c \mathbf{E} + \mathbf{J} \times \mathbf{B} \tag{4.3}$$

Next we introduce Gauss's law and the Maxwell-Ampere equation in divergence form to express ρ_c and $\mathbf{J}$ in terms of $\mathbf{E}$ and $\mathbf{B}$[103],

$$\rho_c = \varepsilon_0 \nabla \cdot \mathbf{E} \tag{4.4}$$

$$\mathbf{J} = \frac{1}{\mu_0} (\nabla \times \mathbf{B}) - \varepsilon_0 \frac{\partial \mathbf{E}}{\partial t} \tag{4.5}$$

Substituting Eqns 4.4 and 4.5 into Eqn 4.3 gives,

$$\begin{aligned}(m_i n_i + m_e n_e) \frac{\partial \mathbf{v}}{\partial t} + m_i n_i (\mathbf{v} \cdot \nabla) \mathbf{v} + \nabla p_e = \\ \varepsilon_0 (\nabla \cdot \mathbf{E}) \mathbf{E} + \frac{1}{\mu_0} (\nabla \times \mathbf{B}) \times \mathbf{B} \\ - \varepsilon_0 \frac{\partial \mathbf{E}}{\partial t} \times \mathbf{B}\end{aligned} \tag{4.6}$$

The time derivative of the electric field can be re-written in terms of $\partial/\partial t\,(\mathbf{E} \times \mathbf{B})$ using the product rule and Faraday's law, such that[103],

$$\begin{aligned}\frac{\partial}{\partial t} (\mathbf{E} \times \mathbf{B}) &= \frac{\partial \mathbf{E}}{\partial t} \times \mathbf{B} + \mathbf{E} \times \frac{\partial \mathbf{B}}{\partial t} \\ &= \frac{\partial \mathbf{E}}{\partial t} \times \mathbf{B} - \mathbf{E} \times (\nabla \cdot \mathbf{E})\end{aligned} \tag{4.7}$$

Substituting Eqn 4.7 into Eqn 4.6 gives,

$$\begin{aligned}(m_i n_i + m_e n_e) \frac{\partial \mathbf{v}}{\partial t} + m_i n_i (\mathbf{v} \cdot \nabla) \mathbf{v} + \nabla p_e = \\ \varepsilon_0 [(\nabla \cdot \mathbf{E}) \mathbf{E} - \mathbf{E} \times (\nabla \times \mathbf{E})] \\ + \frac{1}{\mu_0} [(\nabla \cdot \mathbf{B}) \mathbf{B} - \mathbf{B} \times (\nabla \times \mathbf{B})] \\ - \varepsilon_0 \frac{\partial}{\partial t} (\mathbf{E} \times \mathbf{B})\end{aligned} \tag{4.8}$$

Note that the $(\nabla \cdot \mathbf{B}) \mathbf{B}$ term is added to maintain symmetry between $\mathbf{E}$ and $\mathbf{B}$ by applying Gauss's law of magnetism (i.e. absence of magnetic monopoles $\nabla \times \mathbf{B} = 0$)[103]. The curls in Eqn 4.8 can then be eliminated by applying the vector calculus identity,

$$\mathbf{A} \times (\nabla \times \mathbf{A}) = \frac{1}{2} \nabla (\mathbf{A} \cdot \mathbf{A}) - (\mathbf{A} \cdot \nabla) \mathbf{A} \tag{4.9}$$

Eqn 4.8 then becomes,

$$\begin{aligned}(m_i n_i + m_e n_e) \frac{\partial \mathbf{v}}{\partial t} + m_i n_i (\mathbf{v} \cdot \nabla) \mathbf{v} + \nabla p_e = \\ \varepsilon_0 [(\nabla \cdot \mathbf{E}) \mathbf{E} + (\mathbf{E} \cdot \nabla) \mathbf{E}] \\ + \frac{1}{\mu_0} [(\nabla \cdot \mathbf{B}) \mathbf{B} + (\mathbf{B} \cdot \nabla) \mathbf{B}] \\ - \frac{1}{2} \nabla \left(\varepsilon_0 E^2 + \frac{1}{\mu_e} B^2 \right) \\ - \varepsilon_0 \frac{\partial}{\partial t} (\mathbf{E} \times \mathbf{B})\end{aligned} \tag{4.10}$$

The Maxwell stress tensor $\bar{\mathbf{T}}$ is then introduced as,

$$\bar{\mathbf{T}}_{ij} = \varepsilon_0 \left(E_i E_j - \frac{1}{2}\delta_{ij} E^2 \right) + \frac{1}{\mu_0} \left(B_i B_j - \frac{1}{2}\delta_{ij} B^2 \right) \tag{4.11}$$

where δ_{ij} is a Kronecker delta.

$$\delta_{ij} = \begin{cases} 0 \text{ if } i \neq j, \\ 1 \text{ if } i = j \end{cases} \tag{4.12}$$

Taking the divergence of $\bar{\mathbf{T}}$ and introducing the Poynting vector $\mathbf{S} = \mu_0^{-1} (\mathbf{E} \times \mathbf{B})$, Eqn. 4.10 can be written in a more compact form as,

$$\begin{aligned} m_i n_i (\mathbf{v} \cdot \nabla) \mathbf{v} + \nabla p_e - \nabla \cdot \bar{\mathbf{T}} = \\ - (m_i n_i + m_e n_e) \frac{\partial \mathbf{v}}{\partial t} - \varepsilon_0 \mu_0 \frac{\partial \mathbf{S}}{\partial t} \end{aligned} \tag{4.13}$$

Considering a fixed volume of plasma V, the left-hand side terms represent the instantaneous mechanical and electrical momentum stored within V. Similarly, the right-hand side of Eqn. 4.13 represents the time derivative of the momentum density in V, the first term containing the time derivative of mechanical momentum, the second term containing the time derivative of electromagnetic momentum stored in V. The following discussion shall now be limited to steady systems where the time derivative terms on the right-hand side tend to zero.

To obtain a control surface formulation of Eqn. 4.13, we then consider the surface S containing V defined by the outward unit normal vector $\hat{\mathbf{n}}$ such that Eqn. 4.13 becomes,

$$\underbrace{\int_S n_i m_i (\mathbf{v} \cdot \hat{\mathbf{n}}) \mathbf{v} dS}_{\text{ion momentum}} + \overbrace{\int_S p_e \hat{\mathbf{n}} dS}^{\text{electron pressure}} - \underbrace{\int_S \bar{\mathbf{T}} \cdot \hat{\mathbf{n}} dS}_{\text{Maxwell stress}} = 0 \tag{4.14}$$

In words, the variations in mechanical and (net) electromagnetic forces acting within the volume causes the flow of mechanical momentum entering the volume to differ from the flow of mechanical momentum out of the volume, i.e. conservation of momentum in an electromagnetic field must account for the momentum stored by the fields.

The influence of the plasma on a body may then be considered by defining a second surface S_2 within the surface S. Eqn 4.14 is then written as [102],

$$\begin{aligned} &\int_S \left(n_i m_i (\mathbf{v} \cdot \hat{\mathbf{n}}) \mathbf{v} + p_e \hat{\mathbf{n}} - \bar{\mathbf{T}} \cdot \hat{\mathbf{n}} \right) dS \\ + &\int_{S_2} \left(n_i m_i (\mathbf{v} \cdot \hat{\mathbf{n}}) \mathbf{v} + p_e \hat{\mathbf{n}} - \bar{\mathbf{T}} \cdot \hat{\mathbf{n}} \right) dS_2 = 0 \end{aligned} \tag{4.15}$$

Taking S_2 as the body's surface, however, the integral is simply the force exerted on the body by the plasma $\mathbf{F}_C$. Considering an equipotential surface, such as a uniformly charged body, the contribution of the electron pressure can be neglected [27] and Eqn. 4.15 can be written as,

$$\mathbf{F}_C = - \underbrace{\int_S n_i m_i (\mathbf{v} \cdot \hat{\mathbf{n}}) \mathbf{v} dS}_{\text{direct force}} + \underbrace{\int_S \bar{\mathbf{T}} \cdot \hat{\mathbf{n}} dS}_{\text{indirect force}} \tag{4.16}$$

Eqn. 4.16 provides a different but consistent interpretation of indirect charged aerodynamics compared with the *"binary collision"* and *"linear dielectric response"* formalisms found in dusty

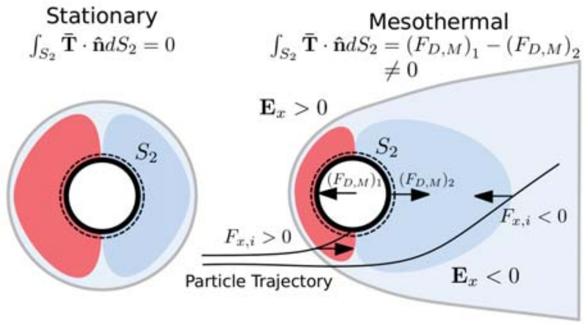

Figure 4.1: Illustration of the linked between sheath structure and indirect charged aerodynamics.

(complex) plasma literature [25, 26, 89, 104], the former focusing on calculating the momentum exchanged between body and scattered ions according to a modified form of Chandrasekhar [13]'s equation for dynamic friction applied to electrostatic fields [**northrop1990**, 14, 26], the latter approach assigning a permittivity to the plasma and calculating the force due to the non-uniform polarisation of the surrounding plasma (the assumption being that linear theory suffices to predict field polarisation - as Allen [102] points out, this is not necessarily the case). Hutchinson [26, 27] provides a similar argument to justify the use of the above control surface approach, citing the various uncertainties and ambiguities inherent in analytical approaches.

Here, the interpretation of Eqn. 4.16 is that the field stress on the surface, captured by the Maxwell stress tensor, imparts a force on the body to reflect the deformation of fields by the self-consistent plasma sheath setup by ion and electron deflections. For a stationary/quiescent flow, the plasma sheath is symmetric, and the surface integral of the Maxwell stress goes to zero. The directed velocity of the ions in mesothermal interactions, however, results in a deformation of the symmetric sheath structure, compressing the fore-body sheath and extending the wake sheath. As a result, the Maxwell stress appears as a negative pressure on the bodies surface (the off-diagonal components of $\bar{\mathbf{T}}$ contributing an electromagnetic shear force) - units of the Maxwell stress term are N/m^2. Figure 4.1 illustrates this relationship, the acceleration of the fore-body ions tending to pull the body forward (thrust), the deflection of the wake ions tending to pull the body backwards (drag).

4.2 Ionospheric Aerodynamic Mechanisms

To demonstrate the utility of the above control surface methodology, this section investigates the influence of plasma interaction phenomena described by the ion deflection parameter α_k and general shielding ratio χ, which form a part of the plasma interaction phase-space $\mathscr{P}(\alpha_k, \chi, S_i, \mu_e, \beta_k, \Omega_k)$. Quantifying the influence of the remaining scaling parameters to ionospheric aerodynamics is the subject of future work, initial observations suggesting that α and χ dominate the momentum exchange in mesothermal plasma-body interactions i.e. ionospheric aerodynamics.

This section will focus on the drag forces on a uniformly charged cylinder with a fixed surface potential with respect to the environment. Numerical setup is identical to previous chapters. Flow conditions considered in this section are listed in Table 4.1 and are based on representative of conditions experienced within Earth's ionosphere by the Earth Observation System (EOS) during a mean period of solar flare activity at a nominal altitude of 705 km at an inclination of 98.25^o [17].

Table 4.1: Plasma interaction quantities, scaling parameters and drag measurements

	Plasma Interaction Quantities							Scaling Parameters				Drag Coefficients		
#	ϕ_B (V)	r_B (m)	v_B (km/s)	m_i	n_∞ (m^{-3})	T_i (K)	T_e (K)	α_k	χ	μ_e	S_i	$C_{D,d}$	$C_{D,m}$	$C_{D,C}$
1	0	0.3	7.5	O^+	4×10^{10}	1531	1997	0.000	0.0	0.0	5.93	2.167	0.030	2.197
2	-1	0.3	7.5	O^+	4×10^{10}	1531	1997	0.100	8.07	-5.81	5.93	2.566	-0.151	2.415
3	-5	0.3	7.5	O^+	4×10^{10}	1531	1997	0.536	3.61	-29.05	5.93	3.761	-0.703	3.058
4	-10	0.3	7.5	O^+	4×10^{10}	1531	1997	1.073	2.55	-58.1	5.93	4.934	-1.302	3.632
5	-25	0.3	7.5	O^+	4×10^{10}	1531	1997	2.682	1.61	-145	5.93	7.908	-3.192	4.716
6	-50	0.3	7.5	O^+	4×10^{10}	1531	1997	5.364	1.14	-290	5.93	12.93	-6.958	5.977
7	0	0.3	7.5	H^+	4×10^{10}	1531	1997	0.000	0.0	0.0	1.48	3.124	0.268	3.391
8	-1	0.3	7.5	H^+	4×10^{10}	1531	1997	1.705	8.07	-5.81	1.48	6.100	-1.269	4.832
9	-5	0.3	7.5	H^+	4×10^{10}	1531	1997	8.528	3.61	-29.0	1.48	11.67	-5.177	6.495
10	-10	0.3	7.5	H^+	4×10^{10}	1531	1997	17.05	2.55	-58.1	1.48	16.83	-9.219	7.616
11	-25	0.3	7.5	H^+	4×10^{10}	1531	1997	42.63	1.61	-145	1.48	29.60	-19.30	10.30
12	-50	0.3	7.5	H^+	4×10^{10}	1531	1997	85.28	1.14	-290	1.48	48.27	-35.50	12.77
13	0	0.03	7.5	O^+	4×10^{10}	1531	1997	0.000	0.0	0.0	1.48	2.178	0.017	2.195
14	-1	0.03	7.5	O^+	4×10^{10}	1531	1997	0.107	0.80	-5.81	5.93	2.600	-0.134	2.467
15	-10	0.03	7.5	O^+	4×10^{10}	1531	1997	1.073	0.25	-58.1	5.93	6.222	0.693	6.914
16	-25	0.03	7.5	O^+	4×10^{10}	1531	1997	2.682	0.16	-145	5.93	12.19	6.143	18.33
17	-50	0.03	7.5	O^+	4×10^{10}	1531	1997	5.364	0.11	-290	5.93	22.48	7.785	30.26
18	0	0.03	7.5	H^+	4×10^{10}	1531	1997	0.000	0.0	0.0	1.48	3.149	0.171	3.320
19	-1	0.03	7.5	H^+	4×10^{10}	1531	1997	1.705	0.80	-5.81	1.48	8.137	-0.370	7.767
20	-5	0.03	7.5	H^+	4×10^{10}	1531	1997	8.528	0.36	-29	1.48	23.28	-8.565	14.71
21	-25	0.03	7.5	H^+	4×10^{10}	1531	1997	42.63	0.16	-145	1.48	83.73	-58.00	25.73
22	-50	0.03	7.5	H^+	4×10^{10}	1531	1997	85.28	0.11	-290	1.48	153.2	-120.7	32.46
23	-10	0.3	26.76	O^+	4×10^{10}	1531	1997	0.084	2.55	-58	21.2	2.366	-0.138	2.228
24	-10	0.3	11.97	O^+	4×10^{10}	1531	1997	0.42	2.55	-58	9.46	3.517	-0.502	3.015
25	-10	0.3	7.5	O^+	4×10^{10}	1531	1997	1.072	2.55	-58	5.93	4.938	-1.302	3.637
26	-10	0.3	3.78	O^+	4×10^{10}	1531	1997	4.227	2.55	-58	2.98	8.607	-3.895	4.712
27	-10	0.3	2.676	O^+	4×10^{10}	1531	1997	8.426	2.55	-58	2.12	11.84	-5.838	6.002
28	-10	0.3	1.889	O^+	4×10^{10}	1531	1997	16.90	2.55	-58	1.49	16.69	-8.983	7.715
29	-10	0.3	7.5	O^+	3.07×10^{9}	1531	1997	1.072	0.7	-58	5.93	5.900	-0.459	5.441
30	-10	0.3	7.5	O^+	6.14×10^{9}	1531	1997	1.072	1	-58	5.93	5.713	-0.804	4.909
31	-10	0.3	7.5	O^+	3.07×10^{10}	1531	1997	1.072	2.55	-58	5.93	5.061	-1.268	3.793
32	-10	0.3	7.5	O^+	1.53×10^{11}	1531	1997	1.072	5	-58	5.93	4.429	-1.305	3.124
33	-10	0.3	7.5	O^+	3.07×10^{11}	1531	1997	1.072	7.07	-58	5.93	4.249	-1.362	2.887
34	-10	0.3	7.5	O^+	6.14×10^{11}	1531	1997	1.072	10	-58	5.93	4.098	-1.339	2.759
35	-5	0.3	26.76	O^+	4×10^{10}	1531	1997	0.042	3.6	-29	21.2	2.202	-0.073	2.129
36	-5	0.3	11.97	O^+	4×10^{10}	1531	1997	0.201	3.6	-29	9.46	2.856	-0.304	2.552
37	-5	0.3	8.46	O^+	4×10^{10}	1531	1997	0.421	3.6	-29	6.69	3.482	-0.560	2.923
38	-5	0.3	5.98	O^+	4×10^{10}	1531	1997	0.842	3.6	-29	4.72	4.379	-1.058	3.322
39	-5	0.3	2.67	O^+	4×10^{10}	1531	1997	4.213	3.6	-29	2.12	8.330	-3.285	5.045
40	-5	0.3	1.89	O^+	4×10^{10}	1531	1997	8.451	3.6	-29	1.49	11.45	-5.092	6.358
41	-5	0.3	7.5	O^+	1.53×10^{9}	1531	1997	0.5	0.7	-29	5.93	4.173	-0.441	3.732
42	-5	0.3	7.5	O^+	3.07×10^{9}	1531	1997	0.5	1	-29	5.93	4.124	-0.475	3.649
43	-5	0.3	7.5	O^+	6.14×10^{9}	1531	1997	0.5	1.41	-29	5.93	4.051	-0.519	3.532
44	-5	0.3	7.5	O^+	3.07×10^{10}	1531	1997	0.5	3.61	-29	5.93	4.938	-0.703	4.236
45	-5	0.3	7.5	O^+	3.07×10^{11}	1531	1997	0.5	10	-29	5.93	3.407	-0.756	2.651
46	-25	0.3	7.77	O^+	7.67×10^{9}	1531	1997	2.5	0.707	-145	6.09	9.441	-2.480	6.961
47	-25	0.3	1.73	O^+	7.67×10^{9}	1531	1997	50	0.707	-145	1.36	48.45	-35.21	13.25
48	-25	0.3	7.77	O^+	3.07×10^{12}	1531	1997	2.5	14.14	-145	6.09	5.217	-2.437	2.781
49	-25	0.3	1.73	O^+	3.07×10^{12}	1531	1997	50	14.14	-145	1.36	18.76	-13.66	5.103
50	-5	0.3	7.77	O^+	7.67×10^{9}	1531	1997	0.5	1.58	-29	6.09	3.910	-0.522	3.388
51	-5	0.3	1.73	O^+	7.67×10^{9}	1531	1997	10	1.58	-29	1.36	15.00	-7.481	7.522
52	-5	0.3	7.77	O^+	3.07×10^{12}	1531	1997	0.5	31.62	-29	6.09	3.096	-0.637	2.459
53	-5	0.3	1.73	O^+	3.07×10^{12}	1531	1997	10	31.62	-29	1.36	8.492	-4.415	4.078

4.2.1 Ion Deflection Parameter α_k

The ion deflection parameter α_k describes the ratio of kinetic energy to the potential energy [3],

$$\alpha_k = \frac{Z_i q_e \phi_B}{m_k v_B^2} = \frac{1}{2}\frac{P.E.}{K.E.} \tag{4.17}$$

Figure 4.2 plots three representative flowfields: an ion *"kinetic"* dominated flow ($\alpha_k \ll 1$), a field (*"potential"*) dominated flow ($\alpha_k \gg 1$), and a transient case where ion kinetic and field effects are balanced ($\alpha_k \approx 1$). Flow conditions are defined in Table 4.1. N_i is the freestream normalised ion density. The rarefaction wave angle lines are overlaid to emphasize the change in θ_r with α_k. A full investigation of the relationship between α_k and plasma interaction phenomena is outside the scope of this work, see instead [2, 27, 39, 54].

To summarise: 1) ion streaming energy causes a compression of the forebody sheath and elongation of the wake sheath is decreasing α_k; 2) α_k governs the velocity dependent critical impact parameter b_* describing Orbital Motion (OM) theory (see the following section); 3) α_k describes the rarefaction wave angle θ_r.

To investigate the influence of phenomena governed by α_k on charged aerodynamic forces, Figure 4.3 plots the normalised indirect ($\hat{f}_{D,m}$) and direct ($\hat{f}_{D,d}$) charged drag surface distributions in polar co-ordinates (normalisation is by net charged drag $F_{D,C}$). The purpose of Figure 4.3 is to emphasize how the relative contribution of forebody and wake phenomena to charged aerodynamics forces changes with α_k. Figure 4.3 also shows a breakdown of the total direct and indirect force components (bottom right), expressed in terms of a charged drag coefficient $C_{D,C}$, to illustrate their relative contribution to the net drag on the body. Note that direct forces are calculated numerically based on the momentum transfer of macro-particles that collide directly with the object surface, while indirect forces are calculated directly from the Maxwell stress on the body's surface.

Forebody Surface ($\theta \leq 90^o$):

Kinetic dominated flows are governed by direct forebody drag forces. Case 1 in Figure 4.2 ($\mathscr{P}(0.084, 2.55)$) is an example of this type of flow, where no forebody ion sheath is evident and $\theta_r \rightarrow 0$. The lack of a forebody ion sheath means that the flow is well approximated by a neutral interaction. As the ion kinetic energy decreases relative to the body potential energy, the forebody sheath expands into the flow, and the rarefaction wave angle increases, i.e. ions become increasingly susceptible to potential disturbances as α_k increases.

The expansion of the forebody sheath with α_k causes an increase the effective ion collection area of the body and, therefore, direct forebody drag. Provided that the flow is not *"sheath-limited"* (discussed in Section 3.2.3), forebody ion collection becomes Orbital Motion Limited (OML). OML ion collection is a limit studied in OM theory, where ion collection becomes limited by the underlying orbital energy of an ion. Applying assumptions regarding the structure of the sheath [36, 89], the maximum impact parameter (offset from flow axis) that an incoming ion will undergo a grazing collision is,

$$b_{\mathrm{OML}} = r_B \left(1 - 2\alpha_k\right)^{1/2} \tag{4.18}$$

Here, b_{OML} provides a rough estimation of the increase in effective ion collection area caused by the sheath [3]. As α_k increases, Figure 4.3 shows an increasing indirect forebody thrust. This indirect thrust counters the energy gained by sheath accelerated ions, the net direct forebody drag representing the effective ion collection area. Figure 4.3 however, shows that for potential dominated systems, the indirect thrust can counter the direct forebody drag. This is because it includes the acceleration of non-colliding ions past the forebody into the wake.

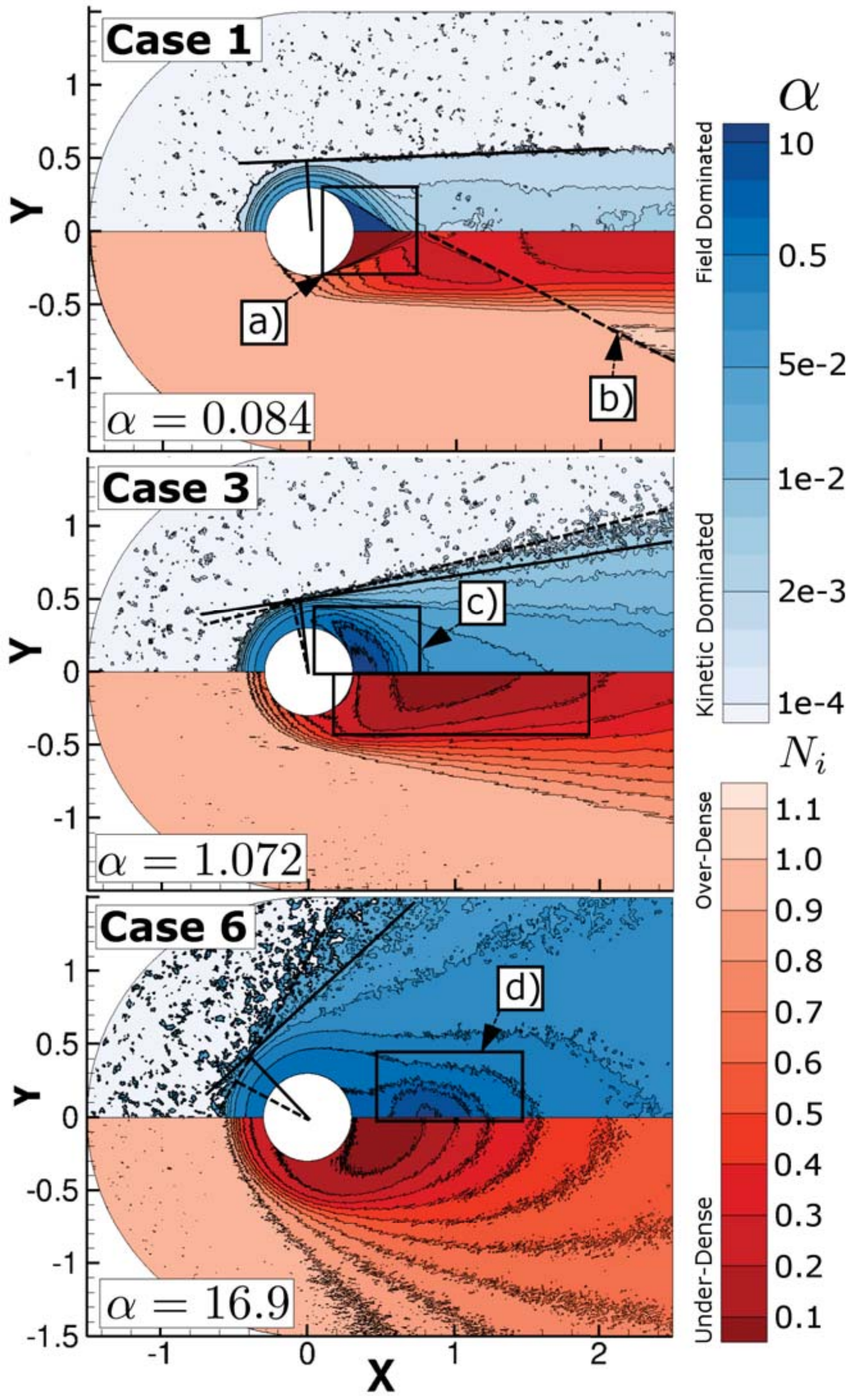

Figure 4.2: Effect of α_k on plasma-interaction phenomena. Labelled features include: a) kinetic dominated ion void, b) kinetic dominated pseudo-wave, c) bounded ion jet d) detached ion void.

Wake Surface ($\theta > 90^o$):

While the anisotropic structure of mesothermal sheaths introduces an additional degree of freedom into the classical problem considered in OM theory, its general results remain applicable. In particular, if the sheath thickness is greater than b_{OML} the structure of the sheath may result in potential energy barriers [36, 89]. These potential barriers correspond to energy dependent inflexion points in the flowfield where, instead of undergoing small angle deflections into the wake, ions are deflected into orbits about the body. These orbits form the bounded ion jets and ion pseudo-waves labelled in Figure 4.2 (and Figure 4.4).

The influence of bounded ion jets is evident in Figure 4.3 as a direct wake thrust. As α_k increases, the proportion of ions deflected into bounded orbits increases and the relative contribution of the direct wake thrust increases. However, as with the forebody ion acceleration, the deflection of these ions imparts an indirect drag countering this direct wake thrust force. Ions that undergo small angle deflections into the wake, however, also contributing to the indirect wake drag. The net effect being a wake drag.

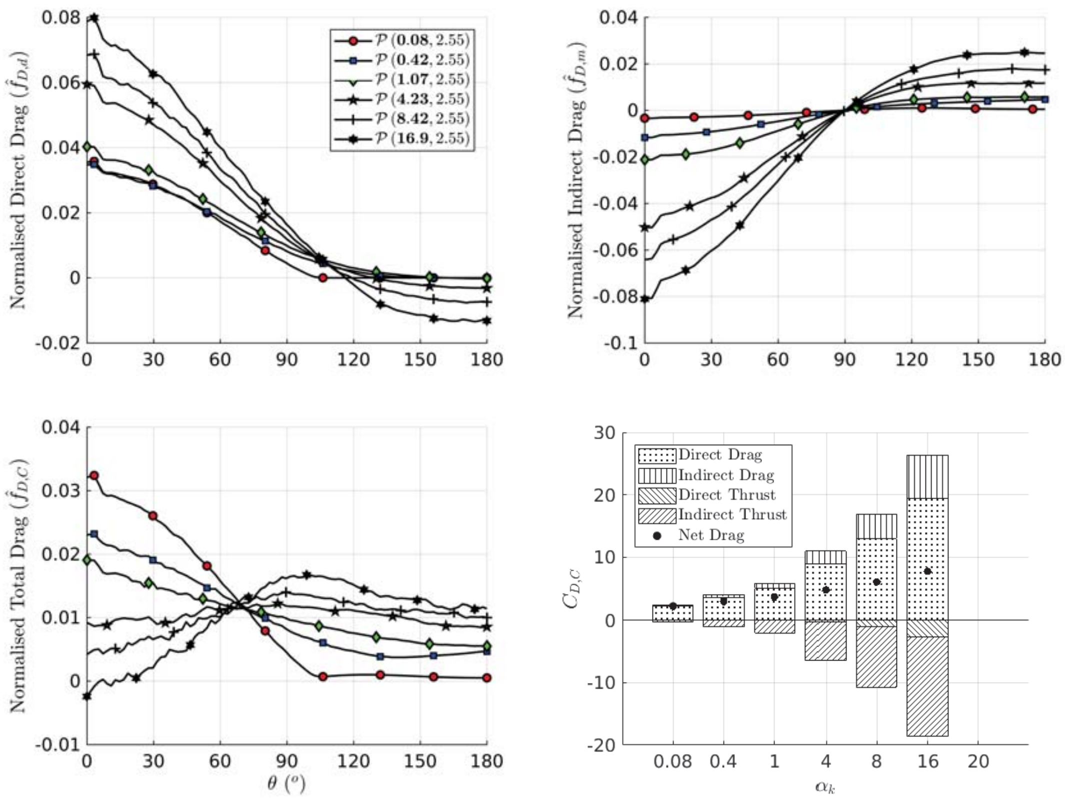

Figure 4.3: Influence of phenomena governed by the ion deflection parameter α_k on the charged drag distributions, and net direct and indirect drag and thrust forces.

Net Effect of α_k on Charged Drag:

Figure 4.3 also shows the integrated contributions of direct and indirect drag components to the net charged drag coefficient $C_{D,C}$ (bottom right panel). As mentioned, for the kinetic dominated case, direct drag forces represent the bulk of forces on a body (direct forebody drag comprising 95% the total drag on the body for $\mathscr{P}(0.084, 2.55)$). As a result, $C_{D,C}$ is 2.232, similar to that predicted by equivalent neutral aerodynamic simulations [7].

For the cases in the range $\mathscr{P}(0.084 \leq \alpha_k < 4.227, 2.55)$, no direct thrust force is evident. The implication being that no bounded ion jets are connecting to the wake surface. The indirect drag thrust does increase in this range, however, causing a 54% reduction in the net $C_{D,C}$ for the $\mathscr{P}(0.084, 2.55)$ case to 4.725. As α_k increases, direct thrust forces become appreciable. However, these direct thrust forces are more than offset by increases in the indirect drag, direct thrust forces countering only 37.6% of the indirect drag in the $\mathscr{P}(16, 2.55)$ case.

4.2.2 General Shielding Ratio χ

The general shielding ratio χ is the ratio of characteristic body radius r_B to the general shielding length λ_ϕ,

$$\chi = \frac{r_B}{\lambda_\phi}, \quad \lambda_\phi = \sqrt{\frac{\varepsilon_0 \phi_B}{q_e \sum_k^K Z_k n_{k,\infty}}} \tag{4.19}$$

For the case where the body potential energy is on the order of the plasma thermal energy ($\phi_B = k_B (T_e + \gamma_i T_i)/q_e$) and the plasma is quasi-neutral, λ_ϕ becomes the Debye length λ_D [3], Alternatively, applying the Child-Langmuir law to high-voltage cathodes, the ion sheath thickness d_{sh} can be written as [100],

$$\frac{d_{sh}}{r_B} = \frac{2^{5/4}}{3}\frac{1}{r_B}\sqrt{\frac{\varepsilon_0 \phi_B}{q_i n_i}} = \frac{2^{5/4}}{3}\chi^{-1} \tag{4.20}$$

In essence, χ describes the ratio of body size to sheath-thickness defined by λ_ϕ. This assertion is supported by Figure 4.4, which shows a thick-sheath ($\chi < 1$), thin-sheath ($\chi \gg 1$), and a transient shielding case. Figure 4.4 shows the formation of an ion density peak in the wake at a) and a dense ion pseudo-wave at b). This is an example of an OML limited flow, where a substantial portion of ions enter the sheath with an impact parameter greater than b_{OML} and are deflected at large angles through the sheath, the confluence point being the axial ion density peak.

Forebody Surface ($\theta \leq 90^o$):

The forebody drag on strongly shielded flows, shown in Figure 4.5, is dominated by direct drag where sheath ion collection enhancement is marginal. As the sheath thickness increases ($\chi \rightarrow 0$), direct charged drag forces asymptote as ion collection becomes OML. Indirect forebody thrust does not show the same asymptote, thrust caused by accelerated non-colliding ions increasing with sheath thickness. However, as with α_k trends, these ions are deflected into orbits about the body and contribute to indirect wake drag. Physical structures to support this conclusion correspond to the dense ion pseudo-waves and axial ion peak seen in Figure 4.4.

Wake Surface ($\theta > 90^o$):

The principal effect of the increasing sheath thickness in Figure 4.5 is to increase the indirect wake drag contribution. As the sheath thickness increases past the OML limit, direct charged drag forces become bounded given a constant α_k. The proportion of ions that enter unbounded orbits and contribute to ion pseudo-waves, however, increases with the sheath thickness. As a result, indirect wake drag continues to increase beyond the OML limit. It should be noted that indirect drag forces may become bounded for values of χ larger than those considered in this work. It is also worth noting that no bounded ion jets contributing to direct wake drag are observed. This is consistent with observations in this work for systems with $\alpha_k < 4.227$.

Net Effect of χ on Charged Drag:

Two asymptotic behaviours are evident in Figure 4.5 (bottom right panel), which shows the integrated direct and indirect contributions to the net charge drag coefficient $C_{D,C}$. For $\chi < 1$

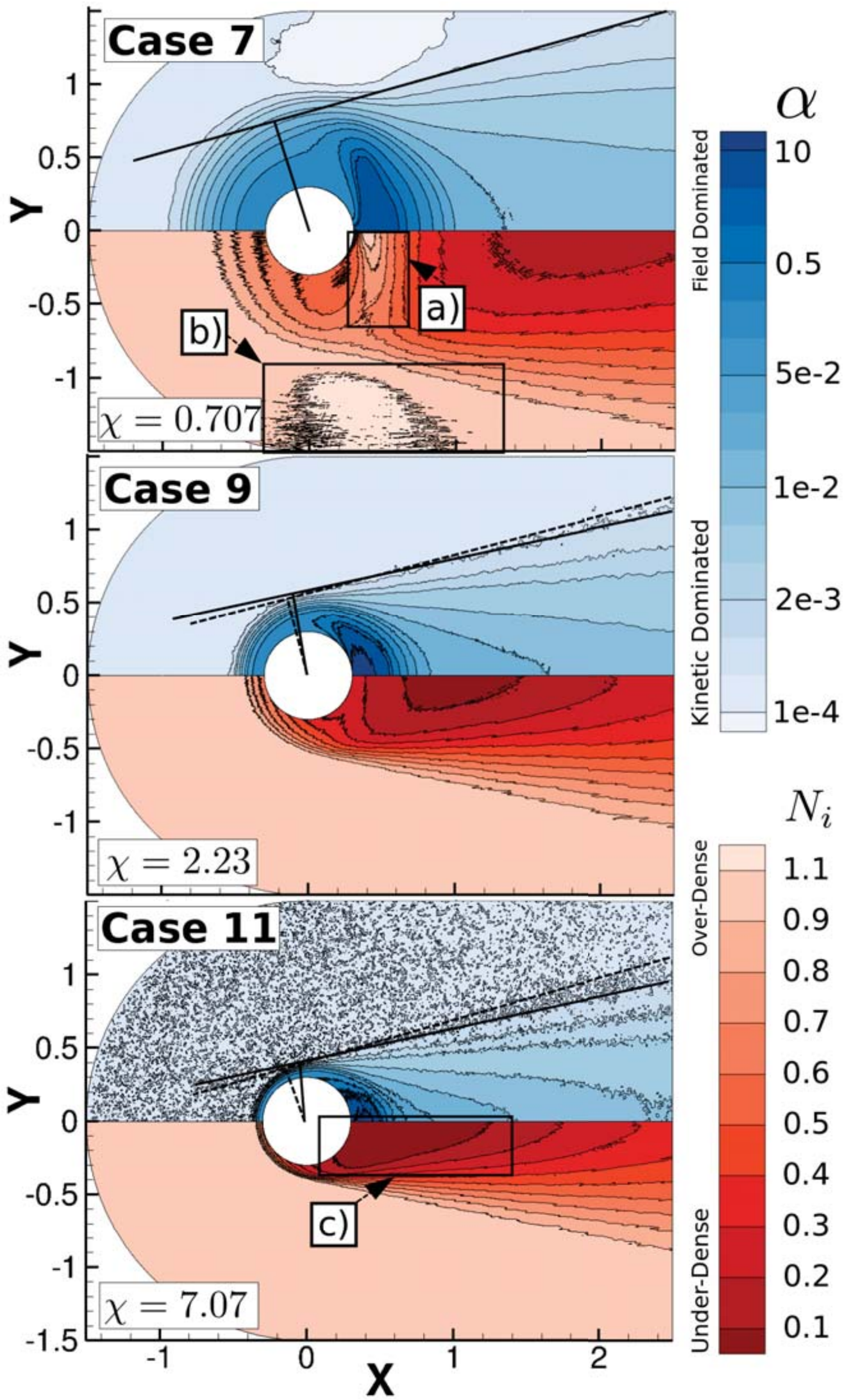

Figure 4.4: Effect of χ on phenomena. Cut-outs show $r_{i,S}$. Labels: a) ion density peak, b) ion pseudo-wave and c) ion void re-attachment.

(thick-sheath), direct drag forces become constant with χ. This supports previous assertions that ion collection becomes OML. For $\chi \gg 1$ (thin-sheath), indirect thrust forces become constant given a constant α_k.

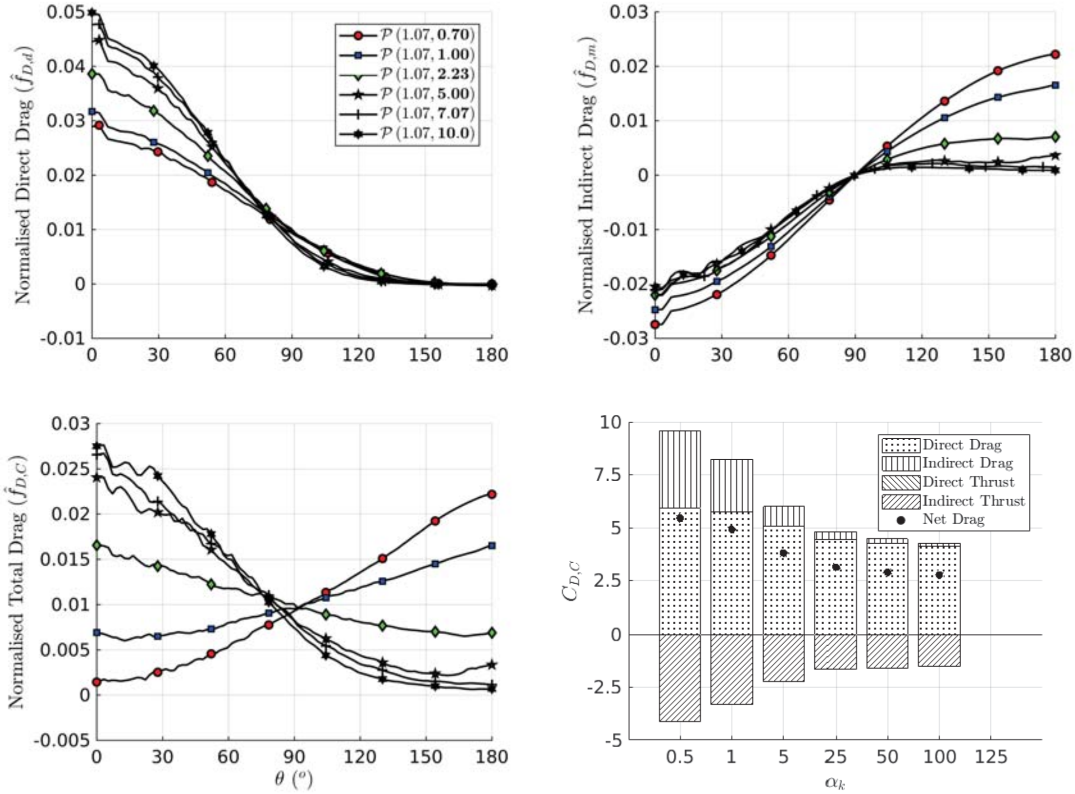

Figure 4.5: Influence of phenomena governed by the general shielding ratio χ on the charged drag distributions, and net direct and indirect drag and thrust forces.

4.3 Ionospheric Aerodynamics Response Surface

The purpose of this section is to to capture the general variations of the charged drag coefficient $C_{D,C}$ caused by plasma-body interaction phenomena defined within the parameter space $\mathscr{P}(\alpha_k, \chi)$. An approximate response surface to describe the variation of $C_{D,C}$ with α and χ can be written as the super-position of three functions that capture the variation of flow structures with α_k, χ and coupled effects i.e.

$$C_{D,C} = f(\alpha_k) + f(\chi) + f(\alpha_k, \chi) \tag{4.21}$$

Based on observations of plasma interaction flow phenomena in the previous section, the contribution of $f(\alpha_k)$ and $f(\chi)$ can be approximated as,

$$f(\alpha_k) = \mathscr{A}\,(1 + 2\alpha_k)^{0.5-a}\,, \quad f(\chi) = \mathscr{B}\chi^{-1} \tag{4.22}$$

Here, the first term $f(\alpha_k)$ has a form similar to the OML impact parameter [36], where $\mathscr{A}$ is some geometry dependent constant and a accounts for the reduction in direct charged drag caused by ion accelerations. The basis of the second term can be clearer by introducing the general shielding length λ_ϕ e.g.

$$\chi = \frac{r_B}{\lambda_\phi}, \quad \lambda_\phi = \left(\frac{\varepsilon_0 \phi_B}{q_e \sum_k^K Z_k n_{k,\infty}} \right)^{1/2} \tag{4.23}$$

As shown in the previous section, the Child-Langmuir law applied to predict the sheath thickness (d_{sh}) about a high-voltage cathode can be written as,

$$\frac{d_{sh}}{r_B} = \frac{1}{r_B}\frac{2^{5/4}}{3}\sqrt{\frac{\varepsilon_0 \phi_B}{q_i n_i}} = \frac{2^{5/4}}{3}\chi^{-1} \tag{4.24}$$

Hence, the $f(\chi)$ term simply describes the change in $C_{D,C}$ caused by the expansion/contraction of the sheath relative to a fixed body dimension. The final coupling term in Eqn. 4.21 will be given the form,

$$f(\alpha_k, \chi) = \mathscr{C}\frac{2\alpha_k^c + \mathscr{D}}{1+\chi} \tag{4.25}$$

$\mathscr{B}$, $\mathscr{C}$, $\mathscr{D}$ and c are all fitted constants. An appropriate physical form and argument for the coupling term and the influence of object geometry on the fitted constants shown in Table 4.2 is a subject for ongoing work.

Table 4.2: Fitted coefficients based on $C_{D,C}$ for cases 1-53.

Coefficient	Value	95% Confidence Interval
$\mathscr{A}$	2.503	(1.978, 3.027)
$\mathscr{B}$	1.973	(1.713, 2.232)
$\mathscr{C}$	53.85	(-195.1, 302.8)
$\mathscr{D}$	-1.996	(-2.03, -1.962)
a	0.3503	(0.2743, 0.4263)
c	0.02255	(-0.0797, 0.1248)

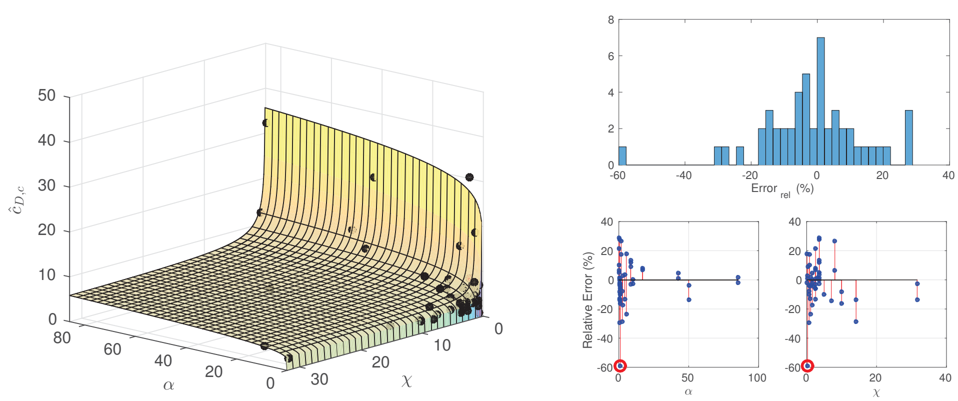

Figure 4.6: Left: Comparison of Eqn. 4.21 with $C_{D,C}$ measurements. Right: Relative error between Eqn. 4.21 and $C_{D,C}$ measurements.

Figure 4.6 (left) overlays Eqn. 4.21 on the $C_{D,C}$ measurements from cases 1-53 to illustrate qualitative agreement between Eqn. 4.21 and simulated $C_{D,C}$ measurements. Figure 4.6 (right) plots the spread of relative error between measured data and Eqn. 4.21. Figure 4.6 (right) highlights that, aside for the weakly shielded case with intermediate coupling case that corresponds to the 60% under-prediction of $C_{D,C}$, Eqn. 4.21 captures the general variation of $C_{D,C}$ for LEO objects.

4.4 Summary

By applying the control surface approach in Allen [102] to Particle-in-Cell simulations, this section has demonstrated the importance of accounting for both direct and indirect forces on LEO objects caused by their interaction with the ionosphere. In particular, this section studied how plasma interaction phenomena govern by the ion deflection parameter α_k and general shielding ratio χ influence the distribution of charged aerodynamic forces on a body and provide currently unconsidered physical mechanisms to explain anomalous accelerations experience by LEO objects.

The ion deflection parameter α_k was observed to have a strong influence on the deflection of ions and the balance of direct and indirect forces on forebody and wake surfaces. Charged drag in kinetic dominated systems ($\alpha_k \ll 1$) was shown to be well approximated by neutral aerodynamics; the $C_{D,C}$ of 2.232 for the $\alpha_k = 0.082$ system consistent with prior $C_{D,N}$ predictions. As the electrical body potential energy dominated the system ($\alpha_k > 1$), ion deflections were enhanced and the indirect forces became increasingly significant. This was illustrated by for the case where $\alpha_k = 16.9$, where direct forebody drag was reduced from a $C_{D,C}$ of 19.36 to 3.35 by an indirect forebody thrust effects (an 82% reduction) to balance the momentum of sheath driven ion accelerations. Indirect wake drag caused by the deflection of non-colliding particles into the wake, however, tended to increase with increasing α_k. This indirect wake drag countering the direct wake thrust produced by bounded ion jets, such that the net $C_{D,C}$ of for this case was 7.741. Note that this is approximately a 3.5 fold increase in charged drag coefficient for the kinetic dominated case.

A similar study of χ emphasised the role of relative sheath thickness in the study of ionospheric aerodynamics. Given a constant α_k, two limiting behaviours were observed with changing χ; sheath-limited flows ($\chi \gg 1$) and Orbital Motion Limited ($\chi \ll 1$) ion collection. An example of a sheath-limited flow is the $\chi = 0.7$ case ($\alpha_k = 1.072$), where indirect drag effects were marginal (3% of total drag forces), and indirect forebody thrust became constant with χ. For OML flows, direct forebody drag was seen to asymptote to approximately $C_{D,C} = 5.9$ for a constant α_k of 1.072. Indirect thrust and drag components, however, did not exhibit the same asymptotic behaviour for the OML cases, indirect drag increasing at a greater rate than indirect thrust - the net trend being an increase in $C_{D,C}$ as $\chi \to 0$.

Based on these observations, a response surface capable of predicting the $C_{D,C}$ of a cylinder was contrusted in terms of α and χ. The intention being to apply this responce surface to quantify whether there exist regions in the near-Earth environment where ionospheric aerodynamic forces become appreciable compared to neutral (thermospheric) aerodynamic forces.

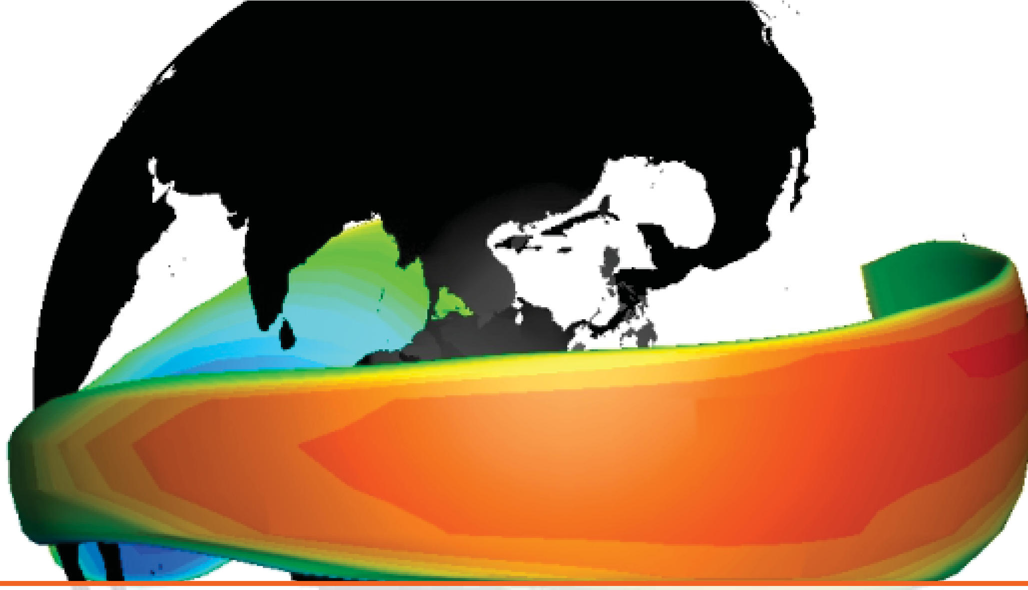

5. Influence of Ionospheric Aerodynamics

Two aspects make the study of ionospheric aerodynamics challenging. The first is the charged aerodynamic interaction in itself; predicting the momentum exchange between a mesothermal flowing plasma and a negatively charged body, requiring an understanding of the complex and nonlinear physical phenomena. The second is the predicting local ionospheric conditions; the ionosphere being a complex, time-varying structure driven by space weather.

To address the first issue, Chapter 3 considered the problem from a dimensional analysis perspective in order to determine the minimum set of scaling parameters that describe multi-species plasma-body interactions. By linking plasma interaction phenomena and charged aerodynamic forces within $\mathscr{P}(\alpha, \chi)$, Chapter 4 organised the complex plasma-body interaction into a usable framework. This chapter applies this framework to quantify whether ionospheric aerodynamics can have an appreciable effect on the orbital motion of LEO objects by considering two questions:

1. Are there regions in LEO where ionospheric aerodynamics forces becomes significant compared to neutral aerodynamics forces?
2. If so, do ionospheric aerodynamic forces in these regions have an appreciable effect on the orbit of LEO objects.

Section 5.1 begins by outlining the conditions considered and the methodology used in this section Section 5.2 then address the first question by predicting the approximate ratio of charged to neutral drag experienced by representative objects using atmospheric data from GITM to investigate regions in LEO where ionospheric aerodynamic forces represent an appreciable portion of the total aerodynamic force vector and have a significant effect on the motion of LEO objects.

5.1 Methodology

The Global Ionosphere/Thermosphere Model (GITM) from the University of Michigan was utilized within the \$15M funded Los Alamos National Laboratory (LANL) program IMPACT (Integrated Modeling of Perturbations in Atmospheres for Conjunction Tracking) [8] to provide a physics-based neutral density modelling and forecasting capabilities in LEO. An output from that work was 2 years' worth of GITM data, covering 2002 and 2007, where the coupled transport of neutral and charged (ion) species is solved directly. This dataset is the primary source used in this report for studying the relative effects from charged and neutral drag contributions to the total aerodynamic drag force experienced. For comparison purposes, data from the same times and altitudes were generated using a combination of the International Reference Ionosphere (IRI) [30] and NRLMSISE-00 [29]. These are used to give insight from the point of view of empirical models of the ionosphere and thermosphere.

5.1.1 GITM Data and Configuration

The GITM data used for this investigation was provided by LANL for the years 2002 and 2007, corresponding to a year of high and low solar activity respectively. The model was run in blocks of one year duration, so the first days of the year include a numerical spin-up period after it was initialised from empirical models. The data was output at a 90 minute cadence with a 2.5^o horizontal resolution corresponding to a 36×72 grid in latitude/longitude. The model runs specified 50 altitude levels, and GITM scales these to correspond to the scale heights of the atmosphere given the initial conditions [105]. This leads to the different years having different altitude grids, with the 2002 data spanning $100-608.5$ km altitude and the 2007 data spanning $100-510.4$ km altitude. GITM is limited to these heights as the fluid equations it solves (Vlasov-Maxwell) do not hold above the exobase, where the mean free path of particles exceeds a scale height.

The provided GITM dataset was run using the measured daily $F_{10.7}$ solar flux, solar wind data and hemispheric power indices as solar and geomagnetic activity inputs. The runs used the MSIS thermosphere model with tides when initialising, and all optional physics were enabled except for the dynamo calculation, which is used to calculate high latitude electric fields. Two high-latitude coupled sub-models available run with GITM - AMIE [106] and GLOW [33] - were also not used.

For the analysis of charged and neutral drag, four time periods were examined in both 2002 and 2007: the March equinox, June solstice, December solstice; and a period centred around April 20th, 2002 that experienced a solar storm in 2002 but was quiet in 2007. The analysis centred around plots at 300, 400, 500 and (where available) 600km altitude - these are the altitudes relevent to LEO objects.

5.2 Charged to Neutral Drag

To identify situations where the ion population has a tangible effect on RSOs this work examines the ratio of charged drag ($F_{D,C}$) to neutral drag ($F_{D,N}$) The total charged drag, $F_{D,C}$ is a sum over the 7 ion species calculated by GITM (O^+, ${O_2}^+$, H^+, He^+, N^+, NO^+ and ${N_2}^+$). The charged drag coefficient, $C_{D,C}$ is calculated using the response surface described in the previous chapter, where α and χ are calculated at each latitude, longitude and alittude using environmental inputs from GITM for specific bodies. For all cases v_B is the orbital velocity of a body in a circular orbit at the specified altitude and is approximately $7.6\text{m}/\text{s}$. If the work was to be extended to the vector case, v_B could be replaced with the vector sum of the orbit velocity and either the neutral or ion wind velocity, which may be provided by GITM.

5.2.1 2002 Global Data

The full 3D flow field from periods of the data from 2002 were probed to understand where in the atmosphere charged drag will be significant. The study focuses on electron (and therefore ion) number density distribution, neutral density distribution, and the ion to neutral density ratio. The charged to neutral force distribution is proportional to ion to neutral ratio for a given radius and surface potential, with higher ion density producing higher charged drag, higher neutral density producing higher neutral drag.

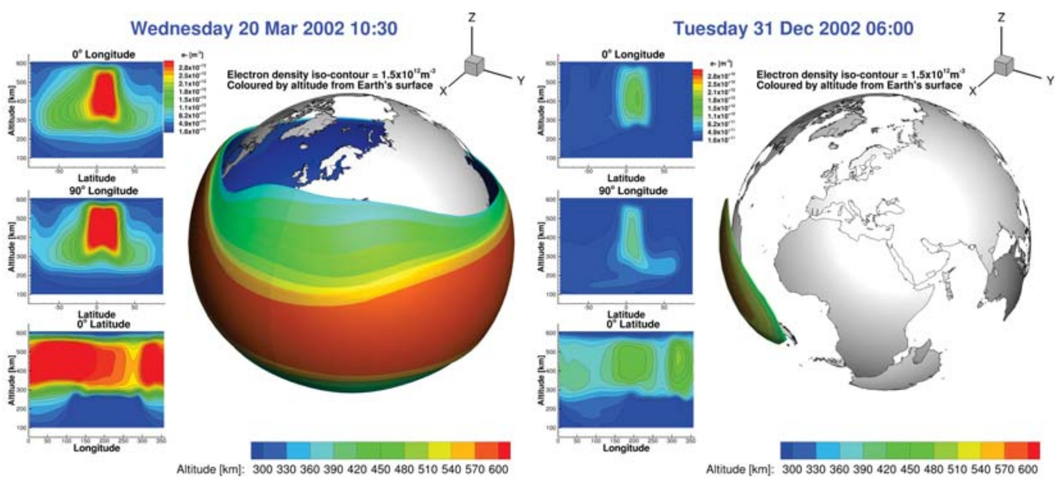

Figure 5.1: $1.5 \times 10^{12}\ m^{-3}$ electron density iso-contour with constant longitude and latitude slices. Left: 20/03/2002 10:30UT (Spring Equinox), Right: 31/12/2002 06:00UT

Figure 5.1 demonstrate the significant seasonal variation in electron density throughout the year. Here, the $1.5 \times 10^{12}\ m^{-3}$ electron density iso-contour illustrates that peak ion density is focused near the equator. Near the spring equinox (left), the electron density iso-contour spreads across latitudes ranging from approximately 45^o north to 45^o south, covering altitudes ranging from 247km to 582km above sea-level. Figure 5.1 right, however shows significantly less activity, with only a small region where the electron density reaches the iso-contour level. In both figures the electron density is maximum near the equator, with a small bias towards the northern hemisphere. This behaviour is consistent throughout the 2002 dataset. The equatorial slice demonstrates that the greatest concentration of ions is within the $400-550$ km altitude range.

The concentration of ions in the equatorial plane convects westward with the sun line as the Earth rotates. Figure 5.2 depicts a band of ions with number density that exceed $2.5 \times 10^{15}\ m^{-3}$ between $300-500$ km altitude at the equator. The sunline is located at 180^o longitude. The main frame illustrates the extent of the ion concentration in latitude, longitude, and altitude, coloured with contours of altitude. The slices in the sidebar to the left of the main frame are flooded with colour contours of electron (ion) number density, with the distribution of electron density plotted against latitude and altitude at 0^o longitude in the top frame; and 90^o longitude in the middle frame. The third (bottom) frame is an equatorial slice (0^o latitude). All three slices have lines of constant neutral density overlaid the colour contours of electron density. The highest altitude neutral density iso-line represents $1 \times 10^{-12}\ kg/m^3$ and the lowest altitude $5 \times 10^{-11}\ kg/m^3$.

The region of highest ion concentration wraps around the majority of the equator, beginning west of the sun line at approximately 150^o longitude and terminating at approximately 50^o. The contour scales selected for the post-processing don't have enough resolution to resolve any addi-

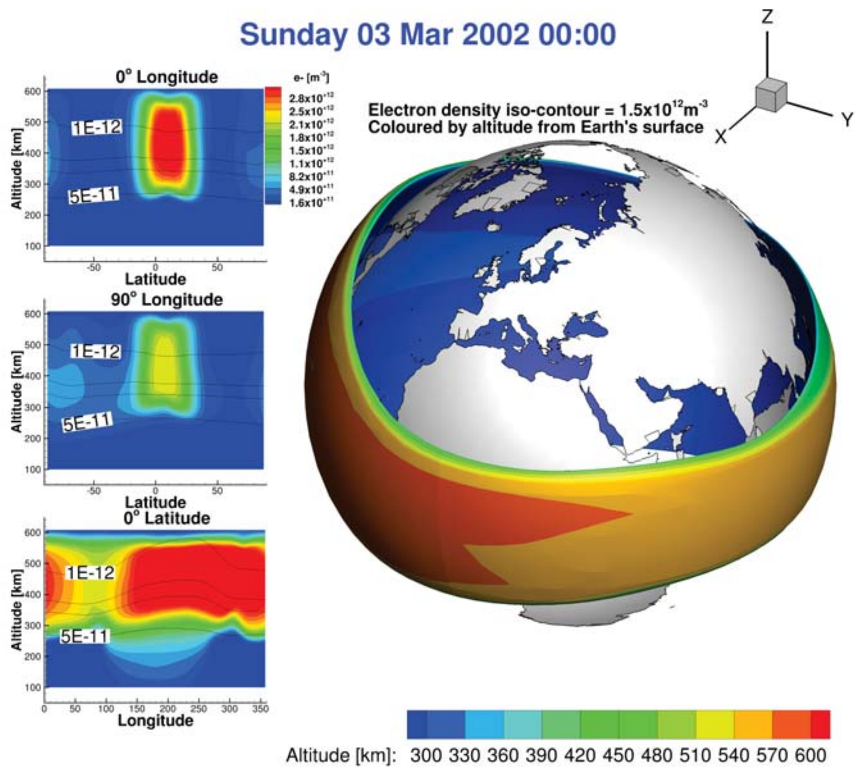

Figure 5.2: Date: 03/03/2002 00:00UT, $1.5x10^{12}m^{-3}$ electron density iso-contour. Slices coloured with e-, lines of constant density

tional structures within this region in Figure 5.4 (left). Figure 5.3 plots the progression of these features over 24 hours. By 6am, the concentration of ions in the equatorial plane has convected westward and two distinct structures are now evident.

The westward convection of the ion concentration is evident in the iso-contour in the main frame. The asymmetry of the electron density iso-contour can be seen to rotate from behind the Earth at midnight to approximately the 90^o longitude plane (second slices in the sidebar) at 6 am, to approximately 0^o at noon. The electron density iso-contour clearly extends into wider latitude bands on the day-side of the Earth. The iso-lines of neutral density plotted on the slices show that the ion concentrations peak in regions with significant expansion or contraction of the thermosphere (high curvature of the neutral desnity iso-lines).

The variation in ion distribution does not directly track the thermosphere expansion or contraction, however, and high ion concentrations persist in areas where the thermospheric density has dropped quickly. This is evident in Figure 5.4 (left). The iso-contour in the main frame represents where the ion to neutral density ratio exceeds 10%. This iso-contour represents the region where charged drag could be a significant contributor to the total aerodynamic drag vector. The slices in the side panel have colour contours of ion to neutral density ratio, with iso-lines of constant neutral density. The regions where the ratio of number densities is greatest coincides with a drop in thermospheric density, where ion concentration remains high but the neutral density has dropped. Comparing with Figure 5.4 (left) it is clear that the altitude range where the maximum ratio of charged to neutral particles occur is higher than where the maximum density occurs.

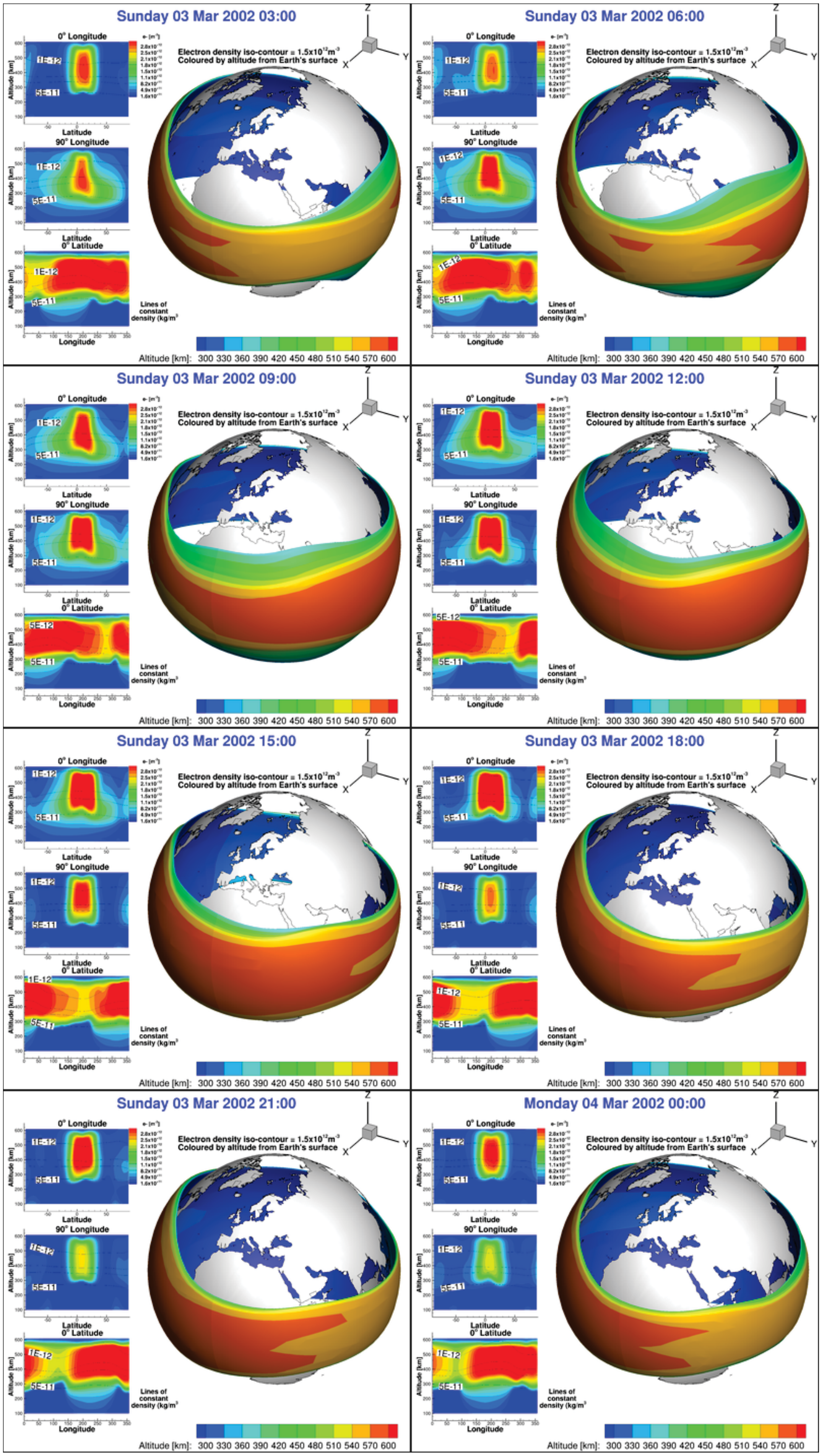

Figure 5.3: Date: 03/03/2002 03:00UT-04/03/2002 00:00UT, $1.5x10^{12}m^{-3}$ electron density iso-contour. Slices coloured with e-, lines of constant density

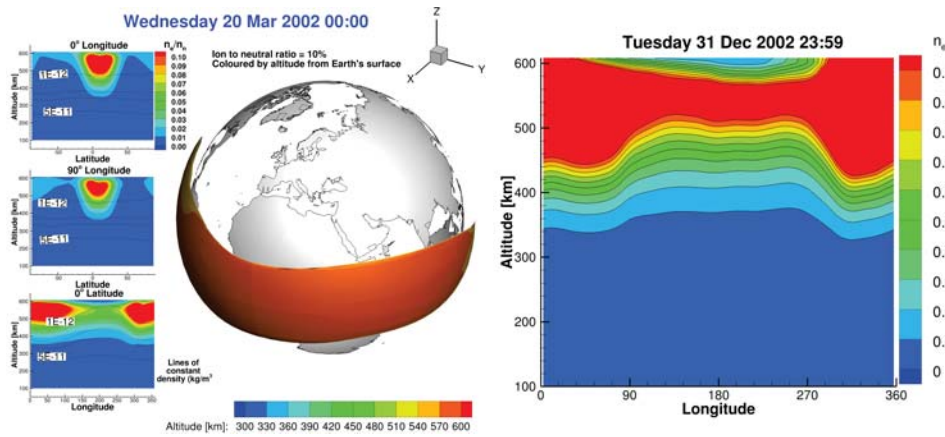

Figure 5.4: Left: 20/03/2002 00:00UT, 10% ion to neutral number density ratio (n_e/n_n) iso-contour. Slices coloured with n_e/n_n, lines of constant density. Right: 31/12/2002 23:59UT, Equatorial slice with colour contours of n_e/n_n

Figure 5.3 plots the progression of the ion to neutral ratio throughout the 3rd of March 2002. The figure shows that an RSO in a 500km equatorial orbit would experience an increase in total drag due to charged aerodynamics for most of its orbit. The same RSO in a polar orbit would experience this force augmentation twice per orbit, with the band covering a latitude range of approximately 45^o across the equator.

The ionospheric activity is significantly reduced during the winter solstice. Figure 5.6 shows similar features to Figure 5.3 described above. A notable difference is that a region of high ion concentration persists from around 300^o longitude throughout the day. It is unclear at this time whether this is a seasonal feature due to the change in sun vector with the tilt of the Earth or an anomaly within the data set. While the magnitude of the ion density decreases towards the end of the year, the ratio of charged to neutral particles increases significantly. Figure 5.4 (right) is an equatorial slice from the final timestep output from the 2002 simulation. There is a significant increase in the ratio of charged to neutral species compared with Figure 5.4 (left), with the charged to neutral ratio reaching 50% in the peak regions.

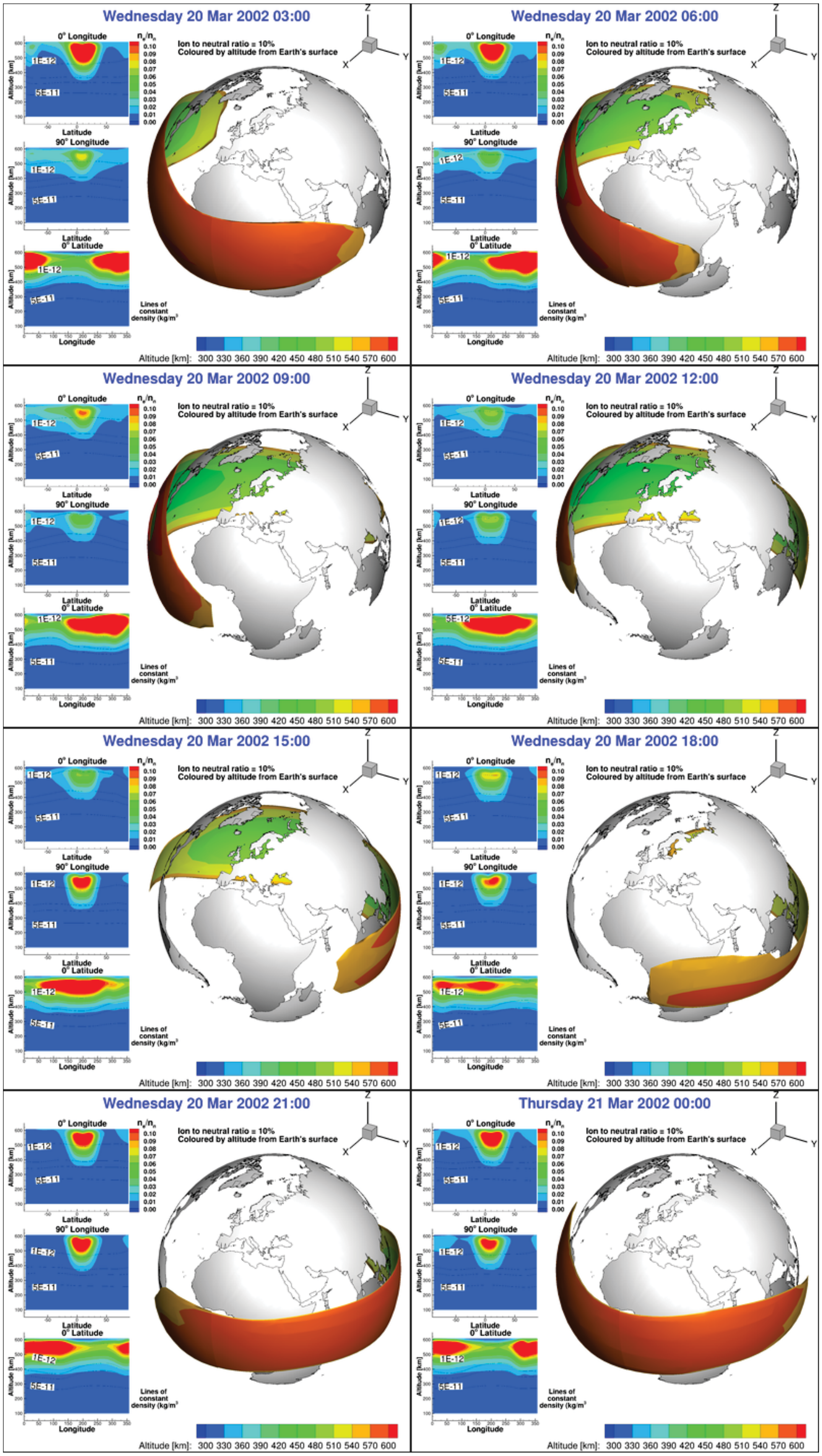

Figure 5.5: Date: 20/03/2002 03:00UT-21/03/2002 00:00UT, 10% ion to neutral number density ratio (n_e/n_n) iso-contour. Slices coloured with n_e/n_n, lines of constant density

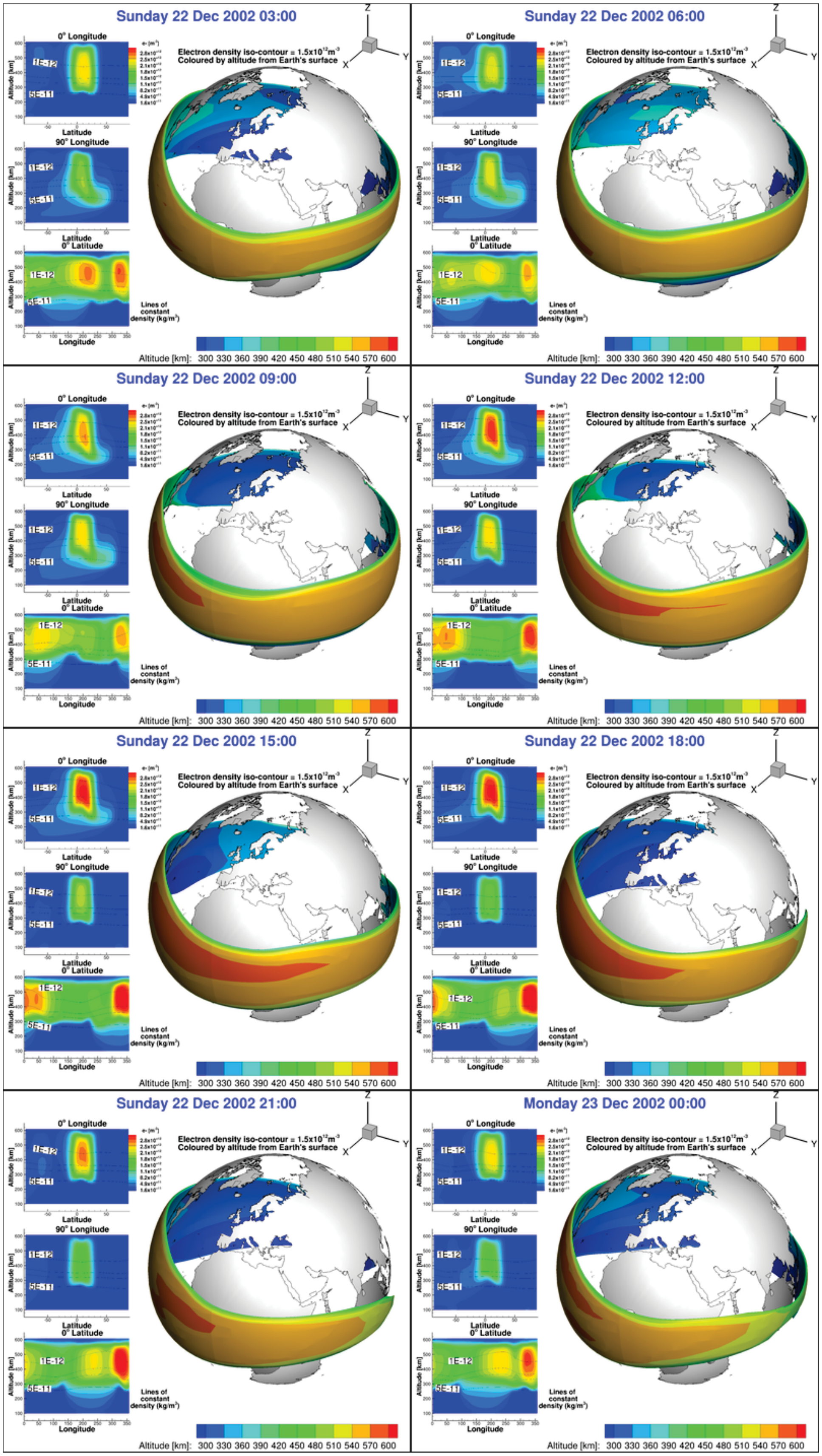

Figure 5.6: Date: 22/12/2002 03:00UT-23/12/2002 00:00UT, $1.5x10^{12}m^{-3}$ electron density iso-contour. Slices coloured with e-, lines of constant density

5.2.2 Charged Force: Basic Features

Figures 5.7 and 5.8 show the resulting plots of $F_{D,C}/F_{D,N}$ at 500 and 600 km for a weakly charged cubsat-sized cylinder during the March equinox in 2002 GITM data. The similar 300 and 400 km plots are omitted as the ratio does not exceed 0.03 due to the dominance of the neutral thermosphere at these lower altitudes. It can be seen in these figures that there are some small areas at 500 km altitude where the ratio approaches 0.15 i.e. the force due to charged drag approaches 15% that of neutral drag. There are larger areas at 500 km and smaller areas at 600 km where the drag ratio is in the $8-10\%$ range, which also represents a non-negligible fraction. For context, at the peak ratio location in Figure 5.7, the neutral drag is approximately 4.7×10^{-7} N and total charged drag is around 6.7×10^{-8} N.

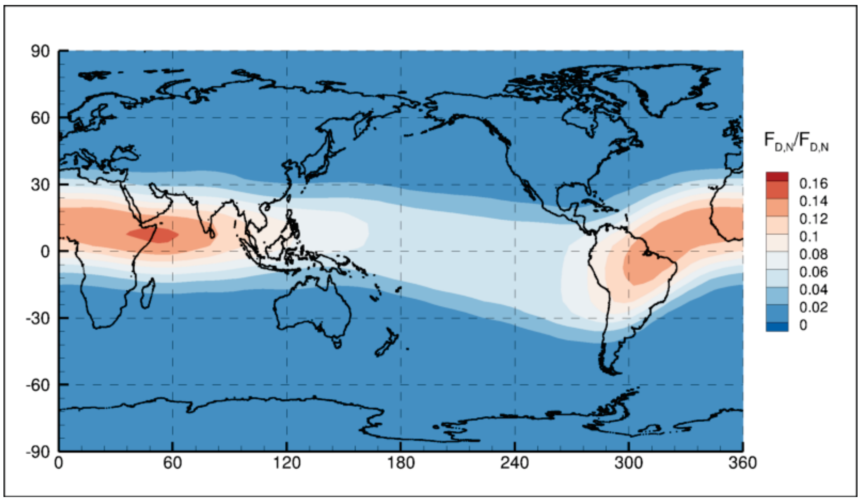

Figure 5.7: Date: 21/03/2002 00:00UT , Altitude = 500km, $r_B = 0.05$m, $\phi_{(0)} = -3$V.

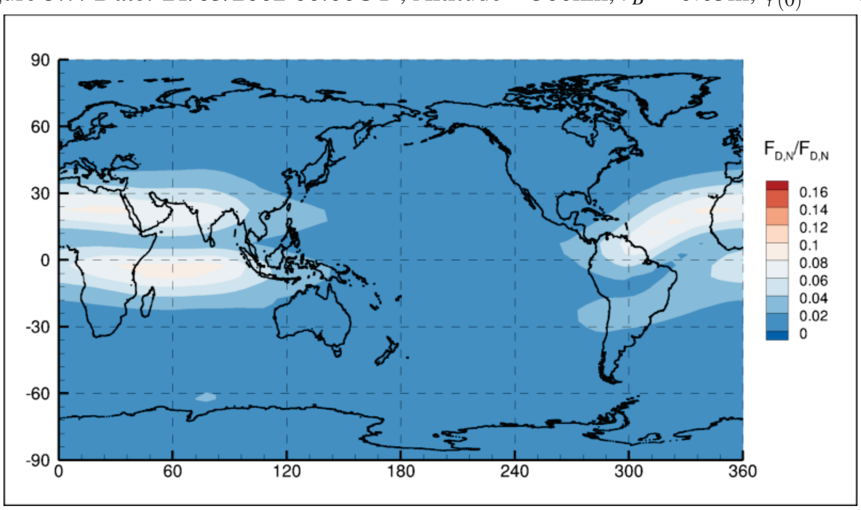

Figure 5.8: Date: 21/03/2002 00:00UT , Altitude = 600km, $r_B = 0.05$m, $\phi_{(0)} = -3$V.

The local ratio of charged to neutral force is not, however, the best measure for the impact that charged aerodynamic forces have on a RSO orbit. The local ratio is dependent upon the phasing of the local maxima and minima of the ion and neutral distributions with respect to one another. A better measure is the difference in work done by the charged and neutral drag, calculated by

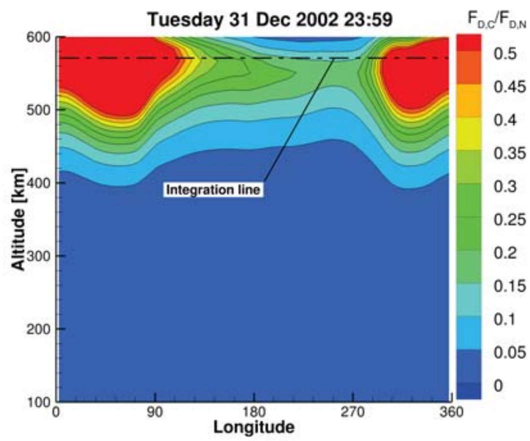

Figure 5.9: Date: 31/12/2002 23:59UT, Latitude=0^o with colour contours of $F_{D,C}/F_{D,N}$, $r_B = 0.05$m, $\phi_{(0)} = -3$V.

integrating the force about an orbit.

Figure 5.9 plots the force ratio distribution for midnight on the 1st January 2003 for a 0.05m radius cylinder at -3 V surface potential. At 570km there is an area that extends from approximately 300^o to 100^o longitude where charged drag exceeds neutral drag by 50% or more. The work done on the cylinder by the neutral and charged aerodynamic force was calculated by integrating the neutral and charged force across this line to understand how these regions of elevated charged drag could impact the RSO throughout its orbit. The work done by charged drag was found to be 31.9% of the neutral drag. This suggests that for these atmospheric conditions, the influence of charged drag would be a significant contribution to the total aerodynamic force.

The work done approach is extended in Figures 5.10 and 5.11 to cover all circular equatorial orbits where charged to neutral drag exceeds 5% and plotted for the entire 2002 and 2007 datasets. There is a marked difference in the overall level of charged to neutral drag ratio between 2002 and 2007, with 2007 exhibiting a substantially higher contribution throughout the entire year than 2002. The maximum occurs at approximately 550km for the 2002 dataset and 466km for 2007. In both figures the data shows that charged aerodynamic drag is considerable over an altitude range where many LEO satellites orbit, with approximately a 100km altitude band where the charged to neutral workdone ratio exceeds 5%. It should be noted that while the ratio of charged to neutral forces is smaller at lower altitudes, the magnitude of the forces are significantly larger at lower altitudes and hence the total orbital perturbation is greater.

The ratio of charged to neutral work done for 2002 is markedly reduced compared with 2007. The greater solar activity in 2002 would intuitively suggest that there should be a higher ratio of charged drag, however the GITM results demonstrate that the increase in neutral density due to increased solar activity is greater than the increase in ions. While the ratio levels are lower in 2002 than 2007 it is important to note that the neutral density at 400km altitude is approximately an order of magnitude greater in 2002 compared with 2007, leading to a far greater orbital perturbation for a given altitude than experienced during 2007.

An important outcome from this analysis is that there does not need to be significant solar activity for charged drag to contribute a significant proportion to the total aerodynamic drag. The results pose questions regarding the accuracy of neutral density estimates derived from accelerometer measurements taken from spacecraft, as the charged drag acceleration within those measurements has not been included in the analysis and data reconstruction process. Reducing uncertainty in

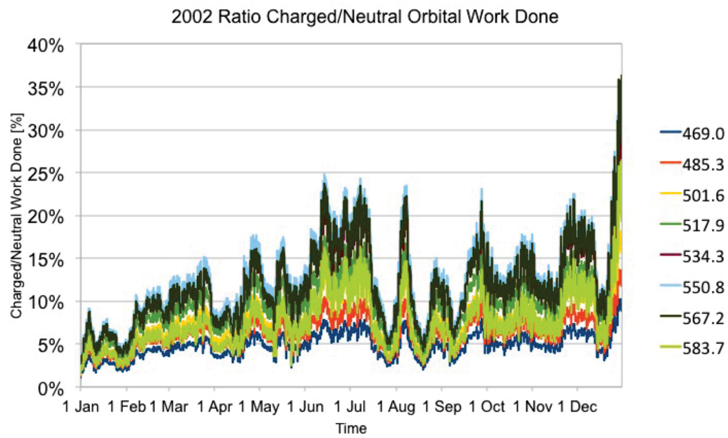

Figure 5.10: 2002: Work done for circular equatorial orbits with ratio of charged to neutral drag above 5%, coloured by altitude

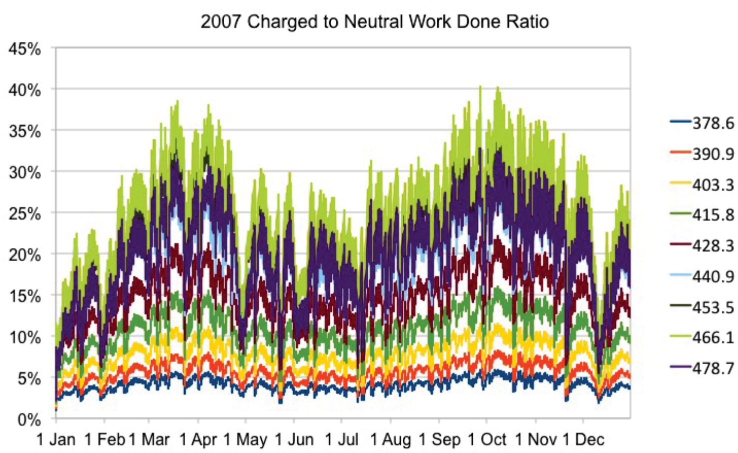

Figure 5.11: 2007: Work done for circular equatorial orbits with ratio of charged to neutral drag above 5%, coloured by altitude

neutral density models to under 10% has been cited as a key driver to improve Space Situational Awareness modelling activities. The results here suggest that inclusion of ionospheric aerodynamics is an essential aspect to consider to achieve this goal.

5.2.3 The Effect of a Physical Model

As a comparison for the ratio plots derived from GITM data, some equivalent plots using IRI for ionospheric data and NRLMSISE-00 for thermosphere data have been produced. Figures 5.13 and 5.14 are the empirically modelled equivalent of figures 5.7 and 5.8. The most obvious difference is that the drag ratio is higher in the GITM plots, this is due to $F_{D,N}$ being around 5 times lower in this data, with $F_{D,C}$ being similar. Another point of difference is the structure of the drag ratio enhancement - in the GITM data it is limited to the equatorial region, in IRI/NRLMSISE-00 data there is a weaker enhancement in the high latitude regions. This may be due to the lack of high-latitude dynamo simulations or coupled models for this region being included in the GITM runs that produced this data. In the GITM data (Figure 5.7 and 5.8) the drag ratio is higher in the

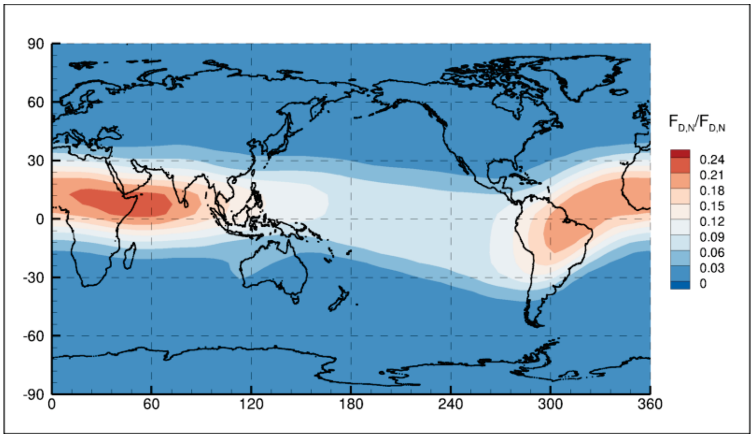

Figure 5.12: Date: 21/03/2002 00:00UT , Altitude = 500km, $r_B = 0.15$ m, $\phi_{(0)} = -30$ V.

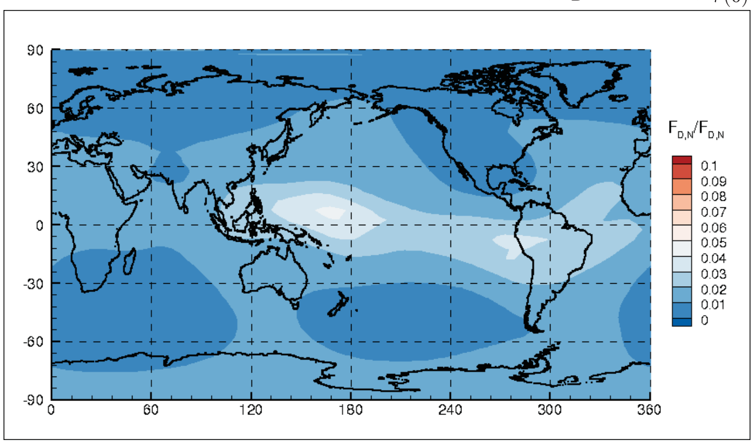

Figure 5.13: Date: 21/03/2002 00:00UT , Altitude = 500km, $r_B = 0.05$ m, $\phi_{(0)} = -3$ V. Data from IRI/NRLMSISE-00.

500km slice than the 600km data, and that the reverse is true of Figure 5.13 and 5.14. This may be due to the 600km altitude range being very close to GITM's top boundary.

Neutral density profiles were taken through the atmosphere from GITM and MSIS for comparison. The profiles were taken on the equator (latitude=0^o) and Longitude=180^o at midnight on the 3rd March 2002 and 31st December 2002. Figure 5.16 shows the neutral density profiles between GITM and NRLMSIS-00 have a similar shape. Applying a 15km offset correction to the 3rd March 2002 GITM data causes the curves to coincide. The neutral density profiles cannot be made to match through a simple altitude offset for the 31st December 2002, however. The GITM data is approximately 50% of the NRLMSIS-00 levels for the 31st December 2002.

Figure 5.17 presents the ratio of the NRLMSISE-00 neutral density to the GITM neutral density for the entire year. The results show that in 2002 there were regions where the NRLMSISE-00 neutral density was 250% of the GITM value. The 2007 data has a significantly greater difference, with 3000% increases in neutral density above 450km altitude in the month of April.

A similar approach has been applied for the electron density distribution through altitude (Figure 5.18). The 3rd March data shows a greater electron density within the IRI model above 350km from GITM. The GITM data shows a near constant electron density of 1.2x$10^{-12}m^{-3}$ from 350km to 520km. The IRI data peaks at 2x$10^{-12}m^{-3}$ at 475km. For the 31st December, the GITM

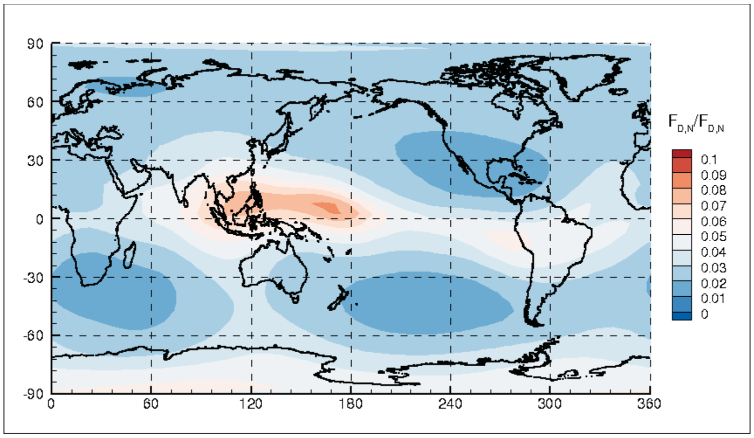

Figure 5.14: Date: 21/03/2002 00:00UT , Altitude = 600km, $r_B = 0.05$m, $\phi_{(0)} = -3$V. Data from IRI/NRLMSISE-00.

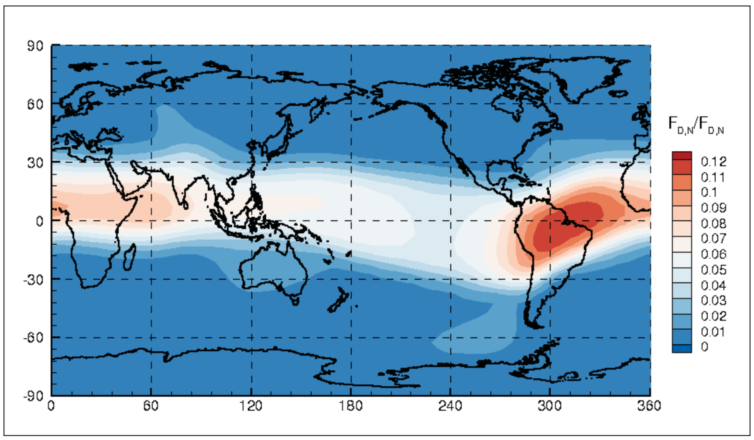

Figure 5.15: Date: 20/04/2002 00:00UT , Altitude = 500km, $r_B = 0.05$m, $\phi_{(0)} = -3$V. Data from GITM.

data displays a very similar profile and magnitude to 3rd March data. The IRI data is scaled down, however, with a peak of $1.5\text{x}10^{-12} m^{-3}$. The GITM result shows that the electron density reduces to zero at the upper boundary, which is non-physical and is assumed to be caused by the boundary condition prescribed.

5.2.4 The Effect of Solar Storms

Figure 5.15 shows the impact of a moderate-to-strong solar storm ($K_p = 7$, DST index = -150 nT) on the drag ratio at 500 km, with similar results for 600 km omitted. When compared to figure 5.7 we can see that the drag ratio is much lower the less disturbed period of time. This indicates that at these altitudes, any enhancement in the ionosphere that might lead to greater ion drag is offset and overwhelmed by the increase in thermospheric density during geomagnetically active times.

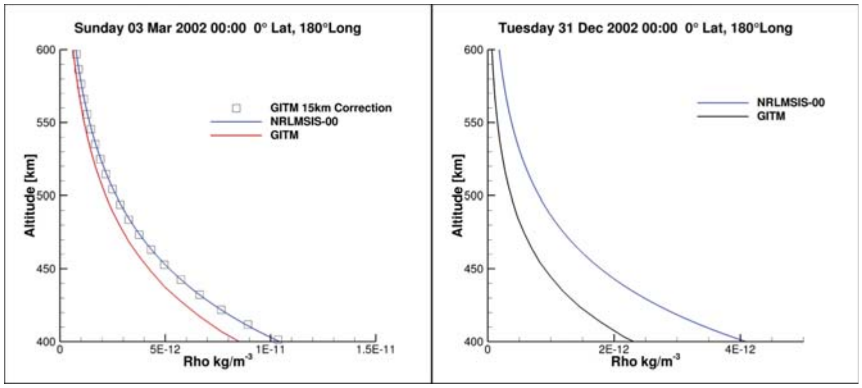

Figure 5.16: Left: 03/03/2002 00:00UT, Right: 31/12/2002 00:00UT Latitude=0^o, Longitude=180^o, neutral density comparison between GITM and NRLMSIS-00

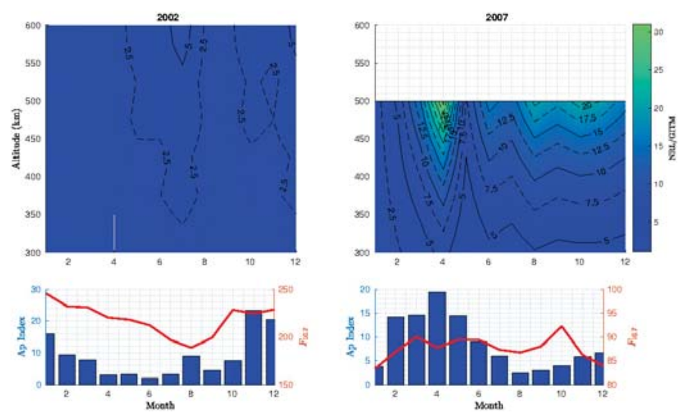

Figure 5.17: Ratio of NRLMSISE-00 to GITM neutral density for equatorial orbits. Left: 2002, Right: 2007

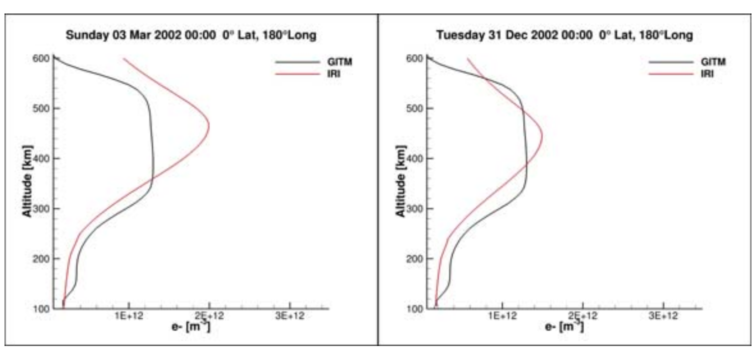

Figure 5.18: Left: 03/03/2002 00:00UT, Right: 31/12/2002 00:00UT, Latitude=0^o, Longitude=180^o, electron density comparison between GITM and IRI

6. Conclusions

Rapid and accurate prediction of Resident Space Objects (RSO) orbital elements is a capability vital for the sustainable development of the near-Earth environment as it becomes increasingly congested and contested. An understanding of all the forces influencing the dynamics of RSOs is fundamental to this capability. The influence of the charged aerodynamic interaction of RSOs with the ionosphere (i.e. ionospheric aerodynamics) on their motion is currently not considered in Precise orbit Prediction and Determination (PoPD) applications despite neutral aerodynamics being the largest non-conservative force on LEO objects with the largest associated uncertainties. The purpose of this report was to determine the significance of ionospheric aerodynamics to the motion of RSOs and, hence, whether it may account for some of the uncertainties currently associated with satellite aerodynamics.

Understanding and modelling the interaction between a charged body and a flowing, tenuous plasma is challenging; the underlying physics strongly non-linear and governed by many independent parameters. A review of previous ionospheric aerodynamic studies along with approaches taken in the study of dusty plasmas - a phenomenologically similar interaction - led to the development of a hybrid Particle-in-Cell (PIC) - Direct Simulation Monte Carlo (DSMC) code, pdFOAM, developed in collaboration with the University of Strathclyde in the OpenFOAM framework. pdFOAM represents a significant improvement over Orbital Motion Limited (OML) analytic techniques used in previous studies of charged aerodynamics, as it is able to capture the self-consistent deformation of the plasma sheath structure surrounding bodies immersed within a LEO-like ionospheric plasma.

pdFOAM was used to systematically study the interaction of charged bodies within ionospheric-like plasmas. Supporting this effort was a dimensional analysis of the unmagnetised Vlasov-Maxwell equations governing the interaction of a charged body immersed within a mesothermal plasma. This study produced a set of 6 non-dimensional scaling parameters that completely describe the non-linear interaction between the charged body and the surrounding plasma.

$$
\begin{aligned}
&\text{Ion Deflection Parameter} && \alpha_k && = -Z_k \left(\frac{q_e \phi_{(0)}}{m_k v_{k,B}^2} \right), \\
&\text{Electron Energy Coefficient} && \mu_e && = \left(\frac{q_e \phi_{(0)}}{k_B T_{e,\infty}} \right), \\
&\text{General Body Shielding Ratio} && \chi && = \frac{r_{(0)}}{\lambda_\phi}, \\
&\text{Ion Temporal Parameter} && \Omega_k && = \left(\frac{\omega_{(0)} r_{(0)}}{v_{k,B}} \right), \\
&\text{Ion Thermal Ratio} && S_k && = \frac{v_{k,B}}{\sqrt{2 k_B T_{k,\infty}/m_k}}, \\
&\text{Ion Coupling Parameter} && \beta_k && = \left(\frac{Z_k n_{k,\infty}}{\sum_k^K Z_k n_{k,\infty}} \right)
\end{aligned}
\tag{6.1}
$$

where the new shielding length scale λ_ϕ was introduced that accounts for the relationship between body surface potentials and sheath thickness and becomes the Debye length λ_D when limited by the assumptions used in its derivation.

$$
\text{General Shielding Length} \quad \lambda_\phi = \left(-\frac{\varepsilon_0 \phi_{(0)}}{q_e \sum_k^K Z_k n_{k,\infty}} \right)^{1/2} \quad [m] \tag{6.2}
$$

This non-dimensional description of the plasma-body system further provided the foundation to permit the scaling of simulation results between environmental, geometric, and body potential conditions. This foundation was augmented through a first principles control surface analysis, separating charged aerodynamic forces into direct forces resulting from gas-surface interactions, and indirect forces resulting from the scattering of non-colliding ions. Here, indirect charged drag forces were accounted for through their self-consistent deformation of the plasma sheath structure, the resulting energy stored in the field translated through to the body as an electrostatic force captured by the Maxwell stress tensor. The work here detailed the complex interplay between the relative contributions of direct and indirect charged drag forces to the to total charged drag exerted on the body by using the determined scaling parameters to isolate and study the influence of phenomena direct and indirect forces.

The ion deflection parameter, α_k was identified as a key driver for charged drag coefficient. The net charged drag in systems dominated by ion kinetic energy ($\alpha_k \ll 1$) were resistant to charged aerodynamic mechanisms, the net charged drag coefficient ($C_{D,C}$) approaching that predicted in a neutral interaction. As α_k increased, the charged drag coefficient increases significantly, with an $\alpha_k = 16.9$ producing a $C_{D,C} = 7.741$ (3.5 times the kinetic dominated case). The increase in α_k corresponds to an increasing contribution from indirect forces and a minor expansion of the sheath; ion deflections becoming more pronounced as the electric potential from the cylinder surface begins to drive the flow structures forming around the cylinder.

The general shield ratio χ, which dictates the relative size of the plasma sheath around the cylinder (or sheath thickness), was found to be another crucial non-dimensional parameter that drives the net drag coefficient. Given a constant α_k, two limiting behaviours were observed with changing χ; sheath-limited flows ($\chi \gg 1$) and Orbital Motion Limited ($\chi \ll 1$) ion collection. An example of a sheath-limited flow was the $\chi = 0.7$ case (with α_k= 1.072), where indirect drag effects were marginal (3% of total drag forces), and indirect forebody thrust became constant with

χ. For OML flows, direct forebody drag was seen to asymptote to approximately $C_{D,C} = 5.9$ for a constant α_k of 1.072. Indirect thrust and drag components, however, did not exhibit the same asymptotic behaviour for the OML cases. Indirect drag increased at a greater rate than indirect thrust - the net trend being an increase in $C_{D,C}$ as $\chi \rightarrow 0$. The results demonstrate the requirement for a high fidelity modelling capability, such as that provided by pdFOAM, to capture the important ionospheric aerodynamic effects that contribute to drag.

A response surface approach was developed from the results of the study to rapdily predict the charged drag force for a cylinder of any radius and negative potential immersed within plasmas that meet the assumptions for a rarefied mesothermal condition. The result that α_k and χ were the most influential non-dimensional parameters driving the charged drag force permitted the response surface to be simplified to a function of α_k and χ alone. This response surface model was applied to thermosphere (neutral) and ionosphere (charged) atmospheric data sets to investigate which orbital regimes are most likely to experience appreciable levels of charged drag. The work used 2 years' worth of data provided by the Los Alamos National Laboratories that utilised the University of Michigan's Global Ionosphere/Thermosphere Model (GITM) spanning a period of high solar activity in 2002 and a lower level of activity in 2007. These datasets provide a coupled, physics-based, description of the thermosphere/ionosphere system; directly resolving the transport of both the neutral and charged species. Further comparisons were made with NRLMSISE-00 thermosphere model and the IRI ionosphere model.

Analysis of the atmospheric data focussed on periods near the spring equinox (21st March) and winter solstice (22nd December). Electron density contours were used to illustrate the distribution of ions for the 2002 data. Near the spring equinox there was a significant increase in ion concentration. An iso-contour for $1.5 \times 10^{12} m^{-3}$ showed the ion distribution around the globe, detailing that a large band of high ion density spanning latitudes from 45^o north to 45^o south and covering altitude ranges from 250-580 km. Peak ion densities were found near the equator, with a small bias towards the northern hemisphere. The greatest ion densities were shown to be approximately within the 400-500 km altitude range. A strong temporal dependence was also observed. Ions were shown to be concentrated at approximately 300-350 degree longitude and convect westward to track the sun-line as the Earth rotates beneath. Further time series analysis is required to extract the short period modes above the strong day/night frequency and relate these to physical phenomena.

Similar ion density features found near the spring equinox are visible throughout the year, however the ion concentration levels are reduced. The concentrated electron density band covers a smaller range of latitudes around the equator and a diminished altitude range compared with the spring equinox. These results indicate that a significant seasonal variation is to be expected for the magnitude of charged aerodynamic forces.

The local ratio of charged to neutral drag is not an appropriate measure to analyse the effect of charged drag on an orbiting body. The local ratio is highly dependent on the location of ion and neutral density maxima and minima relative to one another. Comparing the integrated charged and neutral forces (work done) over a circular orbit at the equator and tracking this ratio through time provided clearer insight into the relative effect that charged drag plays in perturbing an RSO's orbit. For 2002, circular equatorial orbits with altitudes above 469km had >5% contribution to the total work done on the RSO from charged drag throughout the year. The maximum ratio throughout the year was found at 550km, reaching 25% for approximately a month from mid June and rapidly increasing at the end of December to in excess of 30%. The ratio of charged to neutral work done was consistently higher throughout 2007 than 2002, with altitudes above 378km exhibiting 5% or more contribution from charged work done. The 466km altitude orbit produced between 20% and 35% charged drag throughout the entire year.

The results show that charged drag can have a profound influence on the non-conservative force vector experienced by a CubeSat sized RSO in LEO when held at a constant surface potential of -3V. Comparing 2002 and 2007 demonstrated that the contribution of charged drag during low solar activity (2007) was greater than 2002. These results indicate that charged drag could present a significant augmentation to the total aerodynamic force vector throughout the 11-year solar cycle. Comparison against the empirical NRLMSISE-00 neutral density model demonstrated a large discrepancy with the GITM data in 2007, however. This highlights the necessity for ongoing research to improve the accuracy of thermospheric models. Caution is required, however, if atmosphere models are tuned using neutral density derived from satellite accelerometer data if ionospheric aerodynamic drag has not been taken into account.

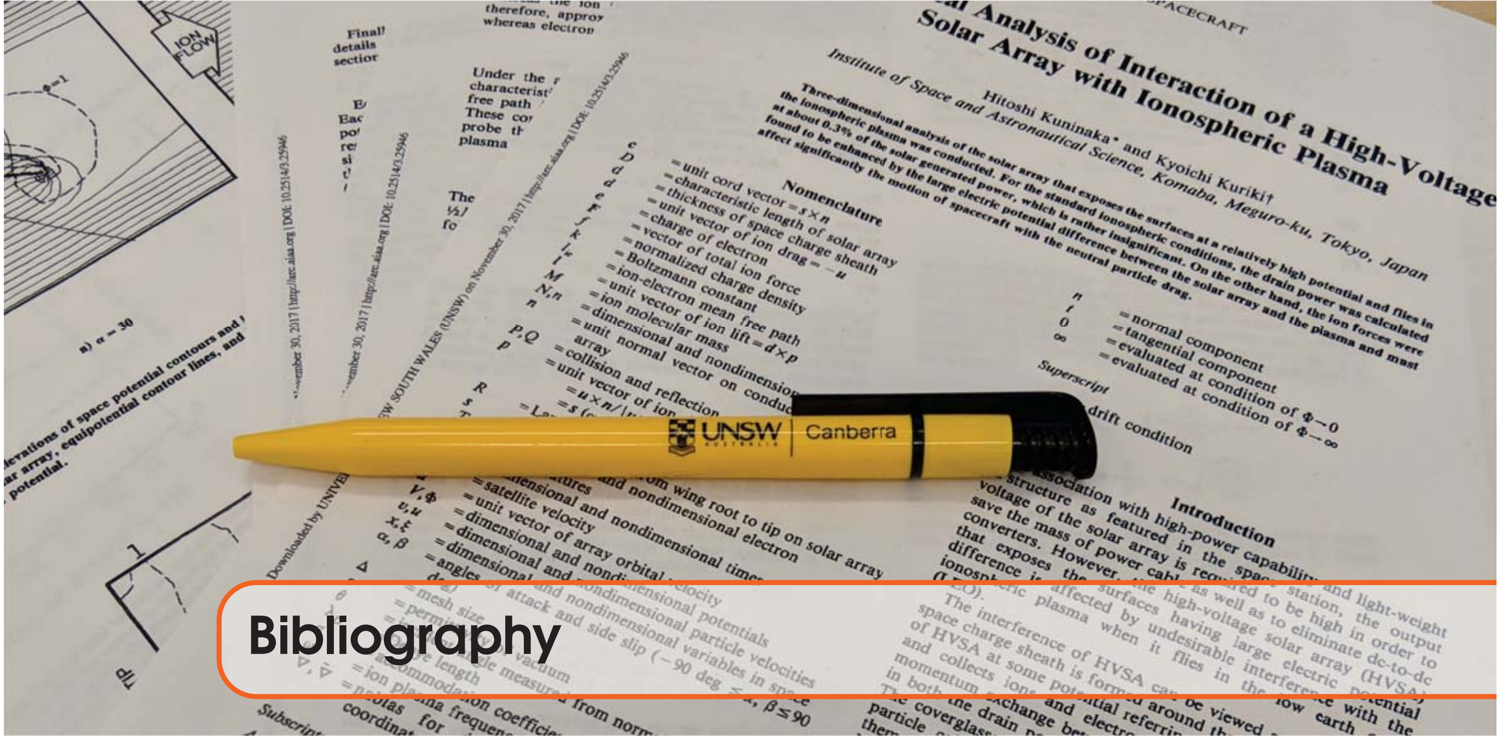

Bibliography

[1] C. J. Capon, R. R. Boyce, and Melrose Brown. "Charged Aerodynamics of a Low Earth Orbit Cylinder". In: *AIP Conference Proceedings* (2016).

[2] C. J. Capon. "Ionospheric Aerodynamics in Low Earth Orbit". PhD thesis. University of New South Wales Canberra, 2017.

[3] C. J. Capon, Melrose Brown, and R. R. Boyce. "Scaling Laws of Plasma-Body Interactions in Low Earth Orbit". In: *Physics of Plasmas* 24.4 (2017).

[4] C. J. Capon et al. "pdFOAM: A PIC-DSMC code for near-Earth plasma-body interactions". In: *Computers and Fluids* 149 (2017), pp. 160–171. ISSN: 00457930. DOI: `10.1016/j.compfluid.2017.03.020`.

[5] National Research Council. *Continuing Kepler's Question: Assessing Air Force Space Commands Astrodynamics Standards*. Tech. rep. Washington: TThe National Academies Press, 2012. DOI: `https://doi.org/10.17226/13456`.

[6] Joseph W Gangestad, Brian S Hardy, and David a Hinkley. "Operations, Orbit Determination, and Formation Control of the AeroCube-4 CubeSats". In: *27th Annual AIAA/USU Conference on Small Satellites* (2013).

[7] Kenneth Moe and Mildred M Moe. "Gas – surface interactions and satellite drag coefficients". In: *Planetary and Space Science* 53 (2005), pp. 793–801. DOI: `10.1016/j.pss.2005.03.005`.

[8] Alexei Klimenko et al. "Impact: Integrated Modeling of Perturbations in Atmospheres for Conjunction Tracking". In: *Advances in the Astronautical Sciences* 152.May 2014 (2014), pp. 3245–3257. ISSN: 00653438. DOI: `10.2514/6.2014-1771`.

[9] Sean Elvidge, Humberto C. Godinez, and Matthew J. Angling. "Improved forecasting of thermospheric densities using multi-model ensembles". In: *Geoscientific Model Development* 9.6 (2016), pp. 2279–2292. ISSN: 19919603. DOI: 10.5194/gmd-9-2279-2016.

[10] E. Doornbos and H. Klinkrad. "Modelling of space weather effects on satellite drag". In: *Advances in Space Research* 37.6 (2006), pp. 1229–1239. ISSN: 02731177. DOI: 10.1016/j.asr.2005.04.097.

[11] Craig A Mclaughlin, S. Mance, and T. Lechtenberg. "Drag Coefficient Estimation in Orbit Determination". In: *Journal of Astronautical Sciences* 58.3 (2011), pp. 513–530.

[12] D. A. Vallado and D. Finkleman. "A critical assessment of satellite drag and atmospheric density modeling". In: *Acta Astronautica* 95.1 (2014), pp. 141–165. ISSN: 00945765. DOI: 10.1016/j.actaastro.2013.10.005. URL: http://dx.doi.org/10.1016/j.actaastro.2013.10.005.

[13] S. Chandrasekhar. "Dynamical Friction". In: *Astrophysical Journal* 97 (1943), p. 255.

[14] C L Brundin. "Effects of Charged Particles on the Motion of an Earth Satellite". In: *AIAA Journal* 1.11 (1963), pp. 2529–2538. ISSN: 0001-1452. DOI: 10.2514/3.2105.

[15] Lee H. Sentman. *Free Molecule Flow Theory and its application to the determination of Aerodynamic Forces*. Tech. rep. California: Lockheed Aircraft Corporation, 1961.

[16] G.E. Cook. "Satellite drag coefficients". In: *Planetary and Space Science* 13.10 (1965), pp. 929–946. ISSN: 00320633. DOI: 10.1016/0032-0633(65)90150-9.

[17] D. E. Hastings. "A review of plasma interactions with spacecraft in low Earth orbit". In: *Journal of Geophysical Research* 100.A8 (1995), pp. 14457–14483. ISSN: 0148-0227. DOI: 10.1029/94JA03358.

[18] R C Olsen and C K Purvis. "Observations of Charging Dynamics". In: *Journal of Experimental and Theoretical Physics* 88 (1983), pp. 5657–5667.

[19] M. S. Gussenhoven et al. "High-Level spacecraft charging in the low-altitude polar auroral environment.pdf". In: *Journal of Geophysical Research* 90.A11 (1985), pp. 11009–11023. DOI: 10.1029/JA090iA11p11009.

[20] Robin Evans et al. "A Preliminary Spacecraft Charging Map for the Near Earth Environment". In: *Spacecraft Charging Technology Conference*. Jet Propulsion Laboratory. 1989. URL: http://holbert.faculty.asu.edu/eee460/spacecharge.html.

[21] Henry B. Garrett and Albert C. Whittlesey. "Spacecraft charging, an update". In: *IEEE Transactions on Plasma Science* 28.6 (2000), pp. 2017–2028. ISSN: 00933813. DOI: 10.1109/27.902229.

[22] Phillip C. Anderson. "Characteristics of spacecraft charging in low Earth orbit". In: *Journal of Geophysical Research* 117.A7 (2012), pp. 1–11. ISSN: 0148-0227. DOI: 10.1029/2011JA016875.

[23] Kyoichi Kuriki and Hitoshi Kuninaka. "Numerical analysis of interaction of a high-voltage solar array withionospheric plasma". In: *Journal of Spacecraft and Rockets* 24.6 (1987), pp. 512–517. ISSN: 0022-4650. DOI: 10.2514/3.25946. URL: http://arc.aiaa.org/doi/10.2514/3.25946.

[24] Jose Andrés de la Fuente. *Enhanced Modelling of LAGEOS Non-Gravitational Perturbations*. Turbineweg, Delft: Sieca Repro, 2007. ISBN: 9789056230814.

[25] I. H. Hutchinson. "Principles of plasma diagnostics". In: *Plasma Physics and Controlled Fusion* 44.12 (2002), p. 2603. DOI: https://doi.org/10.1017/CBO9780511613630.

[26] I. H. Hutchinson. "Ion collection by a sphere in a flowing plasma: 3. Floating potential and drag force". In: *Plasma Physics and Controlled Fusion* 47.1 (2004), pp. 71–87. ISSN: 0741-3335. DOI: 10.1088/0741-3335/47/1/005.

[27] I. H. Hutchinson. "Collisionless ion drag force on a spherical grain". In: *Plasma Physics and Controlled Fusion* 48.2 (2006), pp. 185–202. ISSN: 0741-3335. DOI: 10.1088/0741-3335/48/2/002.

[28] Iver Cairns. *Earth's Atmosphere*. 1999. URL: http://www.physics.usyd.edu.au/%7B~%7Dcairns/teaching/lecture16/node2.html (visited on 01/10/2017).

[29] J. M. Picone et al. "NRLMSISE-00 empirical model of the atmosphere: Statistical comparisons and scientific issues". In: *Journal of Geophysical Research: Space Physics* 107.A12 (2002), pp. 1–16. ISSN: 21699402. DOI: 10.1029/2002JA009430.

[30] Dieter Bilitza et al. "The International Reference Ionosphere 2012 – a model of international collaboration". In: *Journal of Space Weather and Space Climate* 4 (2014), A07. ISSN: 2115-7251. DOI: 10.1051/swsc/2014004.

[31] J. T. Emmert. "Thermospheric mass density: A review". In: *Advances in Space Research* 56.5 (2015), pp. 773–824. ISSN: 18791948. DOI: 10.1016/j.asr.2015.05.038. URL: http://dx.doi.org/10.1016/j.asr.2015.05.038.

[32] E. Doornbos, H. Klinkrad, and P. Visser. "Atmospheric density calibration using satellite drag observations". In: *Advances in Space Research* 36.3 (2005), pp. 515–521. ISSN: 02731177. DOI: 10.1016/j.asr.2005.02.009.

[33] A. D. Richmond. "Assimilative mapping of ionospheric electrodynamics". In: *Advances in Space Research* 12.6 (1992), pp. 59–68. ISSN: 02731177. DOI: 10.1016/0273-1177(92)90040-5.

[34] R. Godd and J. G. Laframboise. "Total current to cylindrical collectors in collisionless plasma flow". In: *Planetary and Space Science* 31.3 (1983), pp. 275–283. ISSN: 00320633. DOI: 10.1016/0032-0633(83)90077-6.

[35] J. G. Laframboise and J. Luo. "High-voltage polar-orbit and beam-induced charging of a dielectric spacecraft: A wake-induced barrier effect mechanism". In: *Journal of Geophysical Research* 94.A7 (1989), p. 9033. ISSN: 0148-0227. DOI: 10.1029/JA094iA07p09033. URL: http://doi.wiley.com/10.1029/JA094iA07p09033.

[36] J. E. Allen. "Probe theory - the orbital motion approach". In: *Physica Scripta* 45.5 (1992), p. 497. ISSN: 0031-8949. DOI: 10.1088/0031-8949/45/5/013.

[37] G. A. Bird. "Direct Molecular Simulation of a Dissociating Diatomic Gas". In: *Journal of Computational Physics* 25.4 (1977), pp. 353–365. ISSN: 00219991.

[38] Nobie H Stone. *The Aerodynamics of Bodies in a Rearefied Ionized Gas with Applications to Spacecraft Environmental Dynamics*. Tech. rep. Alabama: Marshall Space Flight Center, 1981, p. 319.

[39] J. C. McMahon, G. Z. Xu, and J. G. Laframboise. "The effect of ion drift on the sheath, presheath, and ion-current collection for cylinders in a collisionless plasma". In: *Physics of Plasmas* 12.6 (2005), pp. 1–11. ISSN: 1070664X. DOI: 10.1063/1.1924392.

[40] Elden Cole Whipple. "The Equilibrium Electric Potential of a Body in the Upper Atmosphere and in Interplanetary Space". PhD thesis. George Washington University, 1965.

[41] Lee W Parker. "Differential Charging and Sheath Asymmetry of Non-conduction Spacecraft Due to Plasma Flows". In: *Journal of Geophysical Research: Space Physics* 83.A10 (1978), pp. 4873–4876.

[42] Sherman E Deforest. "Spacecraft Charging at Synchronous Orbit". In: *Journal of Geophysical Research* 77.4 (1972), pp. 651–659.

[43] Graeme Shaw. "Analysis of the Ion Current Collection in the Plasma Wake During the Charging Hazards and Wake Studies (CHAWS) Experiment". PhD thesis. Massachusetts Institute of Technology, 1993.

[44] E. C. Whipple. "Potentials of surfaces in space". In: *Reports on Progress in Physics* 44.11 (1981), pp. 1197–1250. ISSN: 0034-4885. DOI: 10.1088/0034-4885/44/11/002. URL: http://iopscience.iop.org/0034-4885/44/11/002.

[45] Alexander Barrie. "Modeling Differential Charging of Composite Spacecraft Bodies Using the Coliseum Framework". PhD thesis. Virginia Polytechnic Institute, 2006.

[46] Joseph Wang, J W Qiu, and X G Qin. "PIC Simulation of Surface Charging in the Wake Zone". In: *PIERS Proceedings*. Hangzhou, China, 2008, pp. 518–521.

[47] Nobie H Stone. "The plasma wake of mesosonic conducting bodies . Part 1 . An experimental parametric study of ion focusing by the plasma sheath". In: *Journal of Plasma Physics* 25 (1981), pp. 351–371.

[48] U. Samir, K. H. Wright, and Nobie H Stone. "The expansion of a plasma into a vacuum - Basic phenomena and processes and applications to space plasma physics". In: *Reviews of Geophysics and Space Physics* 21.7 (1983), pp. 1631–1646. ISSN: 8755-1209. DOI: 10.1029/RG021i007p01631.

[49] Joseph Wang and D. E. Hastings. "Ionospheric plasma flow over large high-voltage space platforms. I : lon-plasma-time scale interactions of a plate at zero angle of attack". In: *Phys. Fluids B* 4.6 (1992), pp. 1597–1614. ISSN: 08998221. DOI: 10.1063/1.860069.

[50] Joseph Wang and D. E. Hastings. "Ionospheric plasma flow over large high-voltage space platforms. II: The formation and structure of plasma wake". In: *Phys. Fluids B* 4.6 (1992), pp. 1597–1614. ISSN: 08998221. DOI: 10.1063/1.860069.

[51] Joseph Wang et al. "Multibody-Plasma Interactions : Charging in the Wake". In: *Journal of Spacecraft and Rockets* 31.5 (1994), pp. 5–10.

[52] S. Meassick et al. "Temporal Study of Wake Formation Behind a Conducting Body". In: *Journal of Geophysical Research: Space Physics* 96.A8 (1991), pp. 13985–13995.

[53] E. Engwall, a. I. Eriksson, and J. Forest. “Wake formation behind positively charged spacecraft in flowing tenuous plasmas”. In: *Physics of Plasmas* 13.6 (2006), pp. 1–10. ISSN: 1070664X. DOI: 10.1063/1.2199207.

[54] Éric Choinière and Brian E. Gilchrist. “Self-consistent 2-D kinetic simulations of high-voltage plasma sheaths surrounding ion-attracting conductive cylinders in flowing plasmas”. In: *IEEE Transactions on Plasma Science* 35.1 (2007), pp. 7–22. ISSN: 00933813. DOI: 10.1109/TPS.2006.889300.

[55] David Burgess and Manfred Scholer. *Collisionless Shocks in Space Plasmas: Structure and Accelerated Particles*. Cambridge: Cambridge University Press, 2015. ISBN: 978-0-521-51459-0.

[56] Hrvoje Jasak, Aleksandar Jemcov, and Zeljko Tukovic. “OpenFOAM : A C ++ Library for Complex Physics Simulations”. In: *International Workshop on Coupled Methods in Numerical Dynamics* 1000 (2007), pp. 1–20.

[57] T. J. Scanlon et al. “An open source, parallel DSMC code for rarefied gas flows in arbitrary geometries”. In: *Computers and Fluids* 39.10 (2010), pp. 2078–2089. ISSN: 0045-7930. DOI: 10.1016/j.compfluid.2010.07.014. URL: http://dx.doi.org/10.1016/j.compfluid.2010.07.014.

[58] Andrew J. Lofthouse. “Nonequilibrium Hypersonic Aerothermodynamics Using the Direct Simulation Monte Carlo and Navier-Stokes Models”. PhD thesis. 2008, p. 231. URL: http://deepblue.lib.umich.edu/bitstream/handle/2027.42/58370/ajloft%7B%5C_%7D1.pdf?sequence=1.

[59] Monika Auweter-Kurtz et al. “Development of a hybrid PIC/DSMC Code”. In: *29 th International Electric Propulsion Conference,* 2005, pp. 1–15.

[60] Willy Feller. “On the Integro-Differential Equations of Purely Discontinuous Markoff Processes”. In: *Transactions of the American Mathematical Society* 48.3 (1940), pp. 488–515.

[61] L. Boltzmann. “Weitere StudiEn fiber das WSxmegleichgewicht unter Gasmolekfilen”. In: *Wien. Ber* (1872).

[62] H. Fehske, Rudolf Schneider, and A. Weibe. *Computaional Many-particle Physics*. New York: Springer, 2008. ISBN: 9783540746850.

[63] Giovanni Lapenta. “DEMOCRITUS: An adaptive particle in cell (PIC) code for object-plasma interactions”. In: *Journal of Computational Physics* 230.12 (2011), pp. 4679–4695. ISSN: 00219991. DOI: 10.1016/j.jcp.2011.02.041. URL: http://dx.doi.org/10.1016/j.jcp.2011.02.041.

[64] Charles K. Birdsall and A. B. Langdon. *Plasma physics via computer simulation*. Vol. 42. New York: Adam Hilger Press, 1991. ISBN: 0750301171. DOI: 10.1016/0010-4655(86)90240-7.

[65] G. A. Bird. *Molecular Gas Dynamics and Direction Simulation of Gas Flows*. Clarendon Press, 1994.

[66] J Clerk Maxwell. “On the Dynamical Theory of Gases”. In: *Philosophical Transactions* January (1867), pp. 49–88.

[67] Wolfgang Wagner. “A convergence proof for Bird’s direct simulation Monte Carlo method for the Boltzmann equation”. In: *Journal of Statistical Physics* 66.3-4 (1992), pp. 1011–1044. ISSN: 00224715. DOI: 10.1007/BF01055714.

[68] G. A. Bird. *The DSMC Method*. 1.1. Sydney: CreateSpace, 2013. ISBN: 1492112909.

[69] Spencer E Olson and Andrew J Christlieb. “Gridless DSMC”. In: *Journal of Computational Physics* 227.17 (2008), pp. 8035–8064. DOI: 10.1016/j.jcp.2008.04.038.

[70] M Pfeiffer, A Mirza, and S Fasoulas. “A grid-independent particle pairing strategy for DSMC”. In: *Journal of Computational Physics* 246 (2013), pp. 28–36. ISSN: 0021-9991. DOI: 10.1016/j.jcp.2013.03.018. URL: http://dx.doi.org/10.1016/j.jcp.2013.03.018.

[71] R W Hockney and J W Eastwood. *Computer Simulation Using Particles*. Abingdon: Taylor & Francis Group, 1988. ISBN: 0852743920. DOI: 10.1137/1025102. URL: http://link.aip.org/link/SIREAD/v25/i3/p425/s1%7B%5C&%7DAgg=doi.

[72] Y. Sentoku and A. J. Kemp. “Numerical methods for particle simulations at extreme densities and temperatures: Weighted particles, relativistic collisions and reduced currents”. In: *Journal of Computational Physics* 227.14 (2008), pp. 6846–6861. ISSN: 00219991. DOI: 10.1016/j.jcp.2008.03.043.

[73] Jean Luc Vay and Brendan B. Godfrey. *Modeling of relativistic plasmas with the Particle-In-Cell method*. 2014. DOI: 10.1016/j.crme.2014.07.006.

[74] Mikhail A. Belyaev. “PICsar: A 2.5D axisymmetric, relativistic, electromagnetic, Particle in Cell code with a radiation absorbing boundary”. In: *New Astronomy* 36 (2015), pp. 37–49. ISSN: 13841076. DOI: 10.1016/j.newast.2014.09.006. arXiv: 1407.1810.

[75] Graham B. Macpherson, Nordin Niklas, and Henry G. Weller. “Particle tracking in unstructured, arbitrary polyhedral meshes for use”. In: *International Journal for Numerical Methods in Biomedical Engineering* 25 (2009), pp. 263–273. ISSN: 20407939. DOI: 10.1002/cnm. URL: http://onlinelibrary.wiley.com/doi/10.1002/cnm.1494/full.

[76] T. J. Scanlon et al. “Simulation of Rarefied and Continuum Hypersonic Flow over Re-Entry Objects”. In: *8th European Symposium on Aerothermodynamics for Space Vehicles*. 2015. ISBN: 8789809289. DOI: 10.1016/j.buildenv.2006.10.027. arXiv: 0812.0143v2.

[77] I Ari Sadarjoen et al. *Particle Tracing Algorithms for 3D Curvilinear Grids*. Tech. rep. Delft, 1994.

[78] Gian Luca Delzanno et al. “CPIC: A curvilinear particle-in-cell code for plasma-material interaction studies”. In: *IEEE Transactions on Plasma Science* 41.12 (2013), pp. 3577–3587. ISSN: 00933813. DOI: 10.1109/TPS.2013.2290060. arXiv: 1311.2286.

[79] Jeremiah Boerner and Iain D. Boyd. “Numerical Simulation of Probe Measurements in a Non-equilibrium Plasma , Using a Detailed Model Electron Fluid”. In: *AIAA Aerospace Science Meeting and Exhibit* 2007-995.January (2007), pp. 1–12.

[80] V. I. Kolobov and R. R. Arslanbekov. "Towards adaptive kinetic-fluid simulations of weakly ionized plasmas". In: *Journal of Computational Physics* 231.3 (2012), pp. 839–869. ISSN: 00219991. DOI: 10.1016/j.jcp.2011.05.036. URL: http://dx.doi.org/10.1016/j.jcp.2011.05.036.

[81] Mickaël Melzani et al. "Apar-T: code, validation, and physical interpretation of particle-in-cell results". In: *Astronomy & Astrophysics* 558 (2013), A133. ISSN: 0004-6361. DOI: 10.1051/0004-6361/201321557. arXiv: 1308.5892. URL: http://www.aanda.org/10.1051/0004-6361/201321557%7B%5C%%7D5Cnhttp://arxiv.org/abs/1308.5892%7B%5C%%7D5Cnhttp://www.aanda.org/10.1051/0004-6361/201321557.

[82] Andrew J. Lofthouse, Iain D. Boyd, and Michael J. Wright. "Effects of continuum breakdown on hypersonic aerothermodynamics". In: *Physics of Fluids* 19 (2007). DOI: 10.1063/1.2710289.

[83] Stefan Dietrich and Iain D. Boyd. "Scalar and Parallel Optimized Implementation of the Direct Simulation Monte Carlo Method". In: *Journal of Computational Physics* 126.2 (1996), pp. 328–342. ISSN: 00219991. DOI: 10.1006/jcph.1996.0141. URL: http://www.sciencedirect.com/science/article/pii/S0021999196901412.

[84] G. A. Bird. "Sophisticated DSMC". In: *Notes prepared for a short course at the DSMC07 meeting*. Santa Fe, 2007, pp. 1–49.

[85] Henry B. Garrett. "The charging of spacecraft surfaces". In: *Review of Geophysics and Space Physics,* 19.4 (1981), pp. 577–616. ISSN: 8755-1209. DOI: 10.1029/RG019i004p00577.

[86] G. A. Bird. *Molecular Gas Dynamics*. Oxford: Clarendon Press, 1976.

[87] W. R. Hoegy and L. E. Wharton. "Current to a moving cylindrical electrostatic probe". In: *Journal of Applied Physics* 44.12 (1973), pp. 5365–5371. ISSN: 00218979. DOI: 10.1063/1.1662157.

[88] Ya. L. Al'Pert, A. V. Gurevich, and L. P. Pitaevskii. *Space Physics with Artificial Satellites*. New York: Consultants Bureau, 1965. DOI: 10.1119/1.1973101.

[89] V. E. Fortov et al. "Complex (dusty) plasmas: Current status, open issues, perspectives". In: *Physics Reports* 421.1-2 (2005), pp. 1–103. ISSN: 03701573. DOI: 10.1016/j.physrep.2005.08.007.

[90] A. Beiser and B. Raab. "Hydromagnetic and Plasma Scaling Laws". In: *Physics of Fluids* 4.2 (1961), p. 177. ISSN: 00319171. DOI: 10.1063/1.1724425. URL: http://scitation.aip.org/content/aip/journal/pof1/4/2/10.1063/1.1724425.

[91] D Knechtel and William C Pitts. "Experimental Investigation of Electric Drag on Spherical Satellite Models". In: *AIAA Aerospace Sciences Meeting* 2.February (1965), pp. 1148–1151.

[92] D. F. Hall et al. "Plasma-Vehicle Interaction in a Plasma Stream". In: *AIAA Electric Propulsion Conference,* 2.6 (1963), pp. 1032–1039. ISSN: 0001-1452. DOI: 10.2514/3.2495.

[93] U Fahleson. "Laboratory Experiments with Plasma Flow Past Unmagnetised Obstacles". In: *Planetary and Space Science* 15.10 (1967), pp. 1489–1497.

[94] J Lacina. “Similarity rules in plasma physics”. In: *Plasma Physics* 13 (1971), pp. 303–312.

[95] S. H. Lam. “Collisionless flow of a plasma mixture”. In: *7th Aerospace Sciences Meeting* 7.11 (1969), pp. 2094–2098. ISSN: 00011452. DOI: doi:10.2514/6.1969-78. URL: http://dx.doi.org/10.2514/6.1969-78.

[96] A. V. Gurevich, L. V. Pariiskaya, and L. P. Pitaevskii. “Self-similar motion of rarefied plasma”. In: *Journal of Experimental and Theoretical Physics* 22.2 (1966), pp. 449–454.

[97] G. I. Barenblatt. *Self-similarity: Dimensional Analysis, and Intermediate Asymptotics*. Ed. by D. G. Crighton. Cambridge University Press, 1996. ISBN: 0521435226.

[98] A. H. Davis and I Harris. *Interaction of a charged satellite with the ionosphere*. Washington, D.C.: National Aeronautics and Space Administration, 1961.

[99] Anthony R Martin. “Numerical Solutions to the problem of charged particle flow around an Ionospheric Spacecraft”. In: *Planetary and Space Science* 22 (1974), pp. 121–141.

[100] M S Benilov. “The Child–Langmuir law and analytical theory of collisionless to collision-dominated sheaths”. In: *Plasma Sources Science and Technology* 18.1 (2008), p. 014005. ISSN: 0963-0252. DOI: 10.1088/0963-0252/18/1/014005.

[101] K -U Riemann. “The Bohm criterion and sheath formation”. In: *Journal of Physics D: Applied Physics* 24.4 (1991), pp. 493–518. ISSN: 0022-3727. DOI: 10.1088/0022-3727/24/4/001. URL: http://stacks.iop.org/0022-3727/24/i=4/a=001?key=crossref.8ef018f33cb54573928abc7217c3932b.

[102] J. E. Allen. “On the drag on an object immersed in a flowing plasma: The control surface approach”. In: *Journal of Plasma Physics* 73 (2007), pp. 773–783. ISSN: 0022-3778. DOI: Doi10.1017/S0022377806006246.

[103] Frederic P. Miller, Agnes F. Vandome, and McBrewster John. *Maxwell Stress Tensor*. VDM Publishing, 2010. ISBN: 9786132848321.

[104] S. A. Khrapak et al. “Hybrid approach to the ion drag force”. In: *Physics of Plasmas* 12.4 (2005), pp. 1–8. ISSN: 1070664X. DOI: 10.1063/1.1867995.

[105] A J Ridley, Y Deng, and G To. “The global ionosphere – thermosphere model”. In: 68 (2006), pp. 839–864. DOI: 10.1016/j.jastp.2006.01.008.

[106] Stanley C. Solomon, Paul B. Hays, and Vincent Abreu. “The Auroral 6300 Å Emission: Observations and Modeling”. In: *Journal of Geophysical Research* 93.A9 (1988), pp. 9867–9882. ISSN: 1098-6596. DOI: 10.1017/CBO9781107415324.004. arXiv: arXiv:1011.1669v3.